IN-32
194219

Interim Progress Report on NAG-5-356 "Optical Communication with Semiconductor Laser Diode"†

F. Davidson and X. Sun

† This report consists of the Doctoral Dissertation submitted to the Johns Hopkins University by Mr. Xiaoli Sun. It summarizes work done on the grant since its inception.

March 1989

ABSTRACT

This dissertation consists of a theoretical and experimental study of the performance limits of a free-space direct detection optical communication system using a semiconductor laser diode as the optical transmitter and a silicon avalanche photodiode (APD) as the receiver photodetector. Optical systems using these components are under extensive consideration as replacements for microwave satellite communication links. Due to the peak and average optical power output constraints inherent in semiconductor laser diodes, optical pulse position modulation (PPM) was chosen as the most appropriate signal format.

An experimental system was constructed that used an AlGaAs (Hitachi-HL8314E, λ=833nm) semiconductor laser diode as the transmitter and a silicon avalanche photodiode (RCA-C30902S) photodetector. The system used Q=4 PPM signaling at a source data rate of 25 megabits per second. The PPM signal format requires regeneration of PPM slot clock and word clock waveforms in the receiver. A nearly exact computational procedure was developed to compute receiver bit error rate without using the Gaussian approximation. A transition detector slot clock recovery system using a phase lock loop was developed and implemented. A novel word clock recovery system was also developed in which a phase lock loop was used to track the random occurrence of back-to-back PPM pulse pairs on the received data stream. This enabled the receiver to establish PPM word boundary synchronization without the presence of specially inserted synchronization patterns in the transmitted data.

It was found that the results of the nearly exact computational procedure agreed well with actual measurements of receiver performance. Use of the widely accepted Gaussian model for the APD output photocurrent was shown to underestimate the value of APD average gain that minimized the bit error rate of a maximum likelihood receiver structure and to substantially overestimate the actual bit error rate of the receiver when the average number of detected background noise photons was less than one per PPM slot time. The maximum likelihood receiver achieved a bit error rate of 10^{-6} at received optical signal levels which corresponded to 55 average detected signal photons per bit. This is best receiver sensitivity yet reported for a direct detection system of this type. The transition detector slot clock recovery system was simple to implement and yet caused no measurable penalty in receiver sensitivity when the phase error was less than one percent of a slot clock cycle. This occurred when the noise bandwidth of the phase lock loop was less than 2×10^{-4} of the slot clock frequency. The new word clock recovery scheme was shown to perform well in initial synchronization. The entire PPM slot and word timing recovery subsystem could acquire and maintain receiver synchronization at received optical signal levels corresponding to more than 15 detected signal photons per transmitted information bit.

To my parents

ACKNOWLEDGEMENTS

I wish to express my gratitude to many people who have helped me to accomplish this work. First, I feel deeply indebted to my research advisor, Professor Frederic Davidson, for his never ending assistance ever since I came to The Johns Hopkins University. It was he who led me to the field of optical communication, improved my English, and guided me to accomplish this work. I would like to thank Dr. James B. Abshire in NASA Goddard Space Flight Center for his support for this project. I would also like to thank Professor Brian Hughes for his careful reading of the manuscript and his many valuable suggestions.

I wish to thank Professor Robert Jenkins for his encouragement in my study at Hopkins. I would like to acknowledge Dr. Andreas Andreou, Dr. Yulin Wang and Dr. Yutai Tom Koh for their counsel and loan of lab equipment. I deeply appreciate Christopher Field's interest in the experimental system and his many valuable suggestions during our discussions. I also thank him for proof reading this manuscript.

I am very grateful to all the friends I met since I came to Hopkins. They have made my life here very interesting and enjoyable.

I am specially indebted to my wife, Xufeng Wu, for her love, encouragement, and support. Finally, I wish to express my deep gratitude to my family, especially my parents, for their love, support, sacrifice, and patience over the years. I dedicate this dissertation to them.

TABLE OF CONTENTS

LIST OF FIGURES

Chapter 1. Introduction

Fiber optic guide laser communication systems have revolutionized terrestrial long distance data transmission. Advances in the technologies of semiconductor laser diodes and silicon avalanche photodiode (APD) photodetectors have now made it possible to realistically consider replacing existing microwave satellite communication systems with optical communication systems. Semiconductor laser diodes are small and highly efficient devices which require only low voltage and low power (few watts) electrical power sources to generate tens to hundreds of milliwatts of optical output power. Because of the much shorter wavelength of the optical frequency radiation (1 micron versus 1 millimeter), very large antenna gains ($\sim$100dB) can be obtained with relatively small sized (10 cm diameter) optical components. As a result, high data rate (100-500 megabits/second) free space optical communication system have become highly competitive with comparable microwave systems [1, 2, 3, 4].

The main objectives of this dissertation were to conduct a theoretical as well as experimental investigation of the performance limits and receiver timing recovery of a direct detection optical communication system which used currently available semiconductor laser transmitter and silicon APD photodetectors. The net results of this work was a state-of-the-art system that used Q=4 pulse position modulation (PPM) signaling at a source data rate of 25 megabits per second. The system achieved a receiver bit error rate (BER) of 10^{-6} at received optical signal levels which corresponded to an average of 55 detected signal photons per source date bit. This is within 10 dB of the absolute (quantum) limit to system performance and is the best performance yet reported for this type of system.

A theoretical analysis of the system performance revealed that standard Gaussian models for the APD output photoelectrons were insufficient for proper system design. A more accurate model was used which required the development of new numerical computational procedures efficient enough to allow receiver BER to be computed without the use of excessive amounts of computer time. Novel PPM slot and word boundary timing recovery subsystems were also developed. Their performance were mathematically characterized and shown to agree well with experimental measurements. Use of the recovered clocks caused no measurable penalty in receiver sensitivity when compared to a receiver with common transmitter/receiver clocks. The net result was the development and laboratory demonstration of a completely self synchronized PPM receiver that could acquire and maintain timing synchronization with the received PPM data stream at received optical pulse energies as low as 15 average detected signal photons per source date bit (30 photons per light pulse). The remander of this introductory chapter further describes the receiver design and analysis and gives explanations for the various design choices made.

A direct detection optical communication system consists of a photodetector which directly converts the received optical signal intensity into a photocurrent. The output of the photodetector can be modeled as a Poisson counting process in which the average counting rate is proportional to the received optical field intensity [5]. The optical signal can only be intensity modulated in a direct detection system.

Another type of optical communication system is called a coherent detection system. The receiver in a coherent detection system must contain

a local oscillator which is phase coherent with the received signal optical field. The local oscillator laser is superposed with the signal optical field and a photodetector is used as the nonlinear device (square law) to generate an intermediate frequency (IF) component. The IF component is proportional to the input signal field strength rather than intensity, and therefore, the optical signal can be either amplitude, frequency, or phase modulated. The performance comparisons between coherent detection and direct detection systems are given in [6, 7]. In general, direct detection systems are far simpler to implement.

Direct detection optical communication systems are sensitive to background radiation because the receiver noise bandwidth is determined by the optical filter preceding the photodetector which is typically on the order of a few angstroms, or hundreds of gigahertz. Coherent detection systems, on the other hand, are relatively immune to background radiation because the receiver noise bandwidth is determined by the IF filter bandwidth which is usually close to the source data rate. The performance of direct detection systems is also limited by amplifier thermal noise. A coherent detection system, on the other hand, can override amplifier thermal noise by increasing the local oscillator laser power, since the IF signal component is proportional to the amplitude of the local oscillator. The performance of coherent detection systems are limited by the amplitude and phase noise of the local oscillator laser. A coherent detection system requires a very complicated optical phase tracking loop in order to generate a coherent local oscillator. The local oscillator laser field and the signal optical field have to be aligned perfectly in spatial mode and polarization in order to generate the IF component properly. Although the technologies of coherent optical communica-

tion are advancing rapidly, semiconductor lasers available today still have excessively high levels of phase and frequency noise. The stability of laser devices, the complexity of the receiver, and the reliability of the entire system are still problems to be overcome in order to fully exploit the potential of coherent communication systems [8]. Direct detection optical communication systems, on the other hand, are much simpler, less expensive and more mature. They have been widely used in terrestrial fiber optic communication systems and will surely play an important role in free space optical communications.

A PPM signal format can be used to improve performance of a direct detection optical communication system when the optical transmitter is average power limited, rather than peak power limited [9]. In PPM signaling, a group of L binary source bits are transmitted as a PPM word which consists of a single light pulse positioned in one of the $Q=2^L$ time slots, as shown in Figure 1.1. If the binary source data rate is $1/T_B$, with T_B the pulse width of the corresponding input binary on-off-keyed (OOK) signal, the PPM pulse width, T_s, is given by $QT_s = LT_B$, or $T_s = (\log_2 Q/Q)T_B$. The major advantage of PPM signaling format is that it concentrates the limited average transmitter laser power into fewer narrower, but higher peak power, PPM pulses. The system performance, as measured by the probability of correct detection, improves because the signal becomes more distinguishable from the background and circuit noise. Since the signal bandwidth of the system is proportional to the reciprocal of the pulse width, PPM signaling requires $Q/\log_2 Q$ times larger bandwidth as that of OOK signaling. However, unlike optic fiber systems, the bandwidth of a free space optical communication system is limited only by the electronics

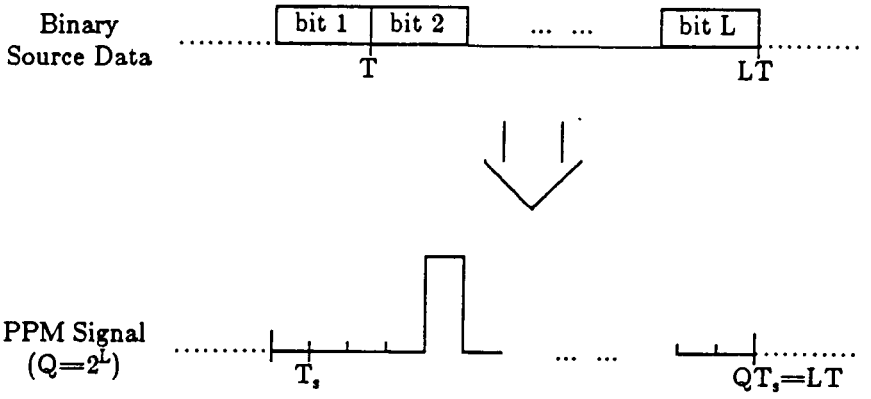

Figure 1.1. PPM signal format

rather than by the light dispersion properties of the transmission media. AlGaAs laser diodes as optical transmitters are average power limited for $Q \leq 8$ PPM signaling [10, 11]. Therefore, low order PPM signaling is suitable for free space direct detection optical communication systems when AlGaAs laser diode transmitters are used.

The ultimate performance of an optical communication system is called the quantum limit, which is the performance achieved in the absence of any noise except for the quantum noise inherent to the photodetection process. The optimal detection scheme for PPM signals consists of the maximum likelihood (ML) detection method. Under the quantum limit, the photodetector output is a Poisson random point process. The probability density for the number of detected photons, N_{t_1,t_2}, within an interval $[t_1,t_2]$ is given by [5]

$$\Pr[\, N_{t_1,t_2}=n] = \frac{1}{n!}\Big(\int_{t_1}^{t_2}\lambda(t)dt\Big)^n \exp\Big[-\int_{t_1}^{t_2}\lambda(t)dt\Big]. \tag{1.1}$$

The average photon count rate, $\lambda(t)$, is given by

$$\lambda(t) \equiv \lim_{\Delta t \downarrow 0}\frac{1}{\Delta t}\Pr[\, N_{t,t+\Delta t}= 1\,] = \frac{\eta P_o(t)}{hf} \tag{1.2}$$

where $P_o(t)$ is the power of the received optical signal, η is the quantum efficiency with which the received photons are converted into photoelectrons, and hf is the photon energy. The sample function density for photon absorption times of the Poisson photon counting process over a PPM word time is [5]

$$p[\omega_1,\omega_2,\cdots,\omega_n, N_{0,QT_s}=n\,] = \Big[\prod_{i=1}^{n}\lambda(\omega_i)\Big]e^{-\int_0^{QT_s}\lambda(t)dt} \tag{1.3}$$

where ω_i represents the time at which the i th detected photon is registered. The likelihood function is defined as the logarithm of (1.3) and can be written as

$$l = -\int_0^{QT_s} \lambda(\sigma)d\sigma + \sum_{i=1}^{N_{QT_s}=n} \ln\lambda(\omega_i)\,. \tag{1.4}$$

The average photon count rate for PPM signaling is piecewise constant, i.e.

$$\lambda(t) = \begin{cases} \lambda_s + \lambda_0 & \text{in the slot containing the PPM pulse} \\ \lambda_0 & \text{in all other slots} \end{cases} \tag{1.5}$$

where λ_s, λ_0 are the photon count rates due to signal and background radiation, respectively. The maximization of (1.4) reduces to

$$\max \{\ln(\lambda_0 + \lambda_s)N_{(j-1)T_s,jT_s} + \sum_{i=1,i\neq j}^{Q} \ln(\lambda_0)N_{(i-1)T_s,iT_s}\,;\ 1\leq j\leq Q\ \}. \tag{1.6}$$

In other words, ML detection of the PPM signal is equivalent to finding the time slot which contains the largest number of detected photons. If the number of detected signal photons per bit is denoted as $\bar{n}_{bit}$, the number of detected signal photons per PPM pulse is $\bar{n}_{bit}\times\log_2 Q$. The PPM word error probability (WEP) under the quantum limit can be written as

$$\text{WEP} = \exp\left[-\bar{n}_{bit}\times\log_2 Q\right]. \tag{1.7}$$

The receiver bit error rate (BER) is related to the PPM word error probability by [12]

$$\text{BER} = \frac{Q}{2(Q-1)}\text{WEP}. \tag{1.8}$$

Equation (1.7) and (1.8) also show that the number of detected signal photons per bit required to achieve a receiver BER decreases monotonically as the alphabet size of the PPM signal, Q, increases.

In a practical optical receiver, the thermal noise and the limited bandwidth of the preamplifier have to be considered. The actual output from the photodetector can be modeled as the sum of a filtered Poisson random point process and a continuous thermal noise process. The exact maximum likelihood function becomes very complicated. The ML detection procedure derived for the quantum limited case may be applied as an approximation. The approximate ML PPM signal detection procedure which can be implemented consists of integrating the photodetector output current over each time slot and then determining which time slot contained the largest integrated electron charge.

There are two types of photodetectors which are suitable for wavelengths emitted by AlGaAs lasers (λ=780$\sim$840nm), silicon photodiodes and silicon avalanche photodiodes (APD). Both of them have quantum efficiencies of about 80% near a wavelength of 800nm. The former is stable and simple to use, but, when the received optical signal power is low, the output photocurrent may be buried completely in the thermal noise of the photodetector load resistor at the input of the preamplifier. An APD photodetector has internal multiplication gain for the primary photocurrent as in a photomultiplier tube, and its output photocurrent is much larger than that of a ordinary silicon photodiode. Personick [13] has shown that use of an APD photodetector can improve the performance of a direct detection optical communication system by 10-15 dB in minimum optical power required to achieve a BER of 10^{-2}–10^{-12}. However, the gain of an APD is random, which introduces so called excess noise in the output photocurrent. A stable and high voltage bias supply is required and some kind of temperature compensation may be necessary in order to keep the average

APD gain constant.

The statistics of the APD output photocurrent is rather complicated as shown in [14, 15]. In many applications, the APD output is approximated as a continuous Gaussian random variable when computing receiver performance. Although the true distribution differs significantly from the Gaussian distribution at the tails of the distribution functions, it is shown [16] that the use of the Gaussian approximation results in only insignificant errors when both the background radiation and received signal levels are high. It was not known, however, if the Gaussian approximation could still be used when the background radiation level is very low. Low background radiation may be encountered in a free space optical communication link between two satellites when neither the Sun, the Earth, or the Moon is in the field of view of the receiver optics [17]. Furthermore, the average number of detected background noise photons per PPM slot time decreases as the data rate increases, because the intensity of the background radiation is constant. Therefore, an accurate and efficient model was needed to characterize the APD output photocurrent under conditions of a very small number of detected background noise photons per PPM time slot.

One of the basic problems inherent in using PPM signal formats is receiver timing recovery and synchronization. The receiver has to reestablish not only PPM slot synchronization but also the PPM word synchronization. Offset or jitters in PPM time slot boundaries will cause the ML detector to integrate over a time interval which overlaps two PPM time slots. As a result, part of the received signal energies is spread into the adjacent time slot and hence acts as background noise. Errors in PPM word boundaries will cause the ML detector to compare the integrated APD outputs

from time slots that do not belong to the same PPM word. This will result in catastrophic detection errors in the regenerated PPM sequence and the demodulated binary data sequence. Timing recovery for PPM signaling can be established using similar methods for bit and word/frame timing recoveries found in conventional digital communication systems that use OOK signal formats. Some studies of timing recovery in optical PPM communication systems have already been done previously [18, 19, 20, 21, 22, 23]. However, it is still of interest to search for new schemes which are more suitable for PPM signal formats, and simpler to implement. The performance of the timing recovery schemes should also be well characterized.

An efficient algorithm was developed that used the nearly exact Webb's approximation [24] for the number of photoelectrons output by an APD. A set of upper bounds were found for the resultant computation errors of the numerical procedure. It was shown that the results of the Gaussian approximation diverged significantly from the results obtained using Webb's approximation when the average numbers of detected background noise photons per PPM slot were less than one.

A laboratory optical communication system was constructed and its performance carefully measured. The system used Q=4 PPM signaling at a source date rate of 25 megabits per second. An AlGaAs laser diode (Hitachi HL8314E, λ=833nm) was used as the optical transmitter and a silicon APD (RCA 30902S) was used as the photodetector. The receiver BER was measured as a function of the average number of detected photons per information bit. It was found that use of the Gaussian approximation for the APD output photocurrent was inappropriate when the background radiation level

was less than one detected noise photon per PPM slot time. For example, when the background radiation level was 0.0122/slot, use of the Gaussian approximation gave an optimal average APD gain that was smaller than the measured value by a factor of two and a BER that was larger than the measured value by 1 to 3 orders of magnitude. The measured values of the optimal average APD gain and the receiver BER agreed well with those predicted when using Webb's approximation.

PPM slot timing recovery in optical communication systems was reviewed and a new scheme was introduced. This scheme, though popular in conventional digital communications, had not been studied for optical PPM communications. It consisted of a transition detector and a phase lock loop (PLL). The transition detector was made of a high speed comparator and a pulse shaper. The output of the pulse shaper consisted of a series of short pulses each of which corresponded to the detection of a positive transition in the received PPM light pulse train. The power spectrum of the transition detector output contained a strong discrete component at the PPM slot clock frequency which was tracked by a PLL. The output of the voltage controlled oscillator of the PLL then formed a continuous and synchronous PPM slot clock. A complete analysis of the phase error in the recovered PPM slot clock was presented and it agreed well with the experimentally measured values. It was shown that use of the recovered slot clock at the receiver caused no measurable degradation in receiver sensitivity if the rms phase error in the recovered PPM slot clock was 1% of a slot clock cycle, or the loop noise bandwidth of the PLL was below 10^{-4} of the slot clock frequency.

A novel PPM word timing recovery scheme was invented that used a PLL to track the occurrence of back-to-back PPM pulses (PPM word "Q" followed by an "1") in the received random data sequences. This PPM word synchronization scheme was efficient because there was no prescribed synchronization pattern inserted into random data and hence no channel use overhead associated with insertion of synchronization patterns. The measured rms phase error of the recovered word clock was close to the values predicted by the theoretical analysis. A special PLL was devised which phase locked the recovered PPM word clock to the slot clock, and consequently, corrected phase errors of the word clock in reference to the slot clock. Use of the recovered slot clock and word clock caused no measurable penalty in receiver sensitivity when compared with a receiver that used common clocks at the transmitter and the receiver. This synchronization system could acquire and maintain the slot and word synchronization for an received optical signal level as low as 15 average detected photons per bit, or 30 photons per PPM pulse.

The completely self synchronized receiver achieved a BER of 10^{-6} at an average received optical signal power of less than -63.5 dBm, which corresponds to 55 detected photons per information bit. This is believed to be the most sensitive receiver yet reported for this type of direct detection optical communication system [25]. The receiver sensitivity achieved was only 9.1 dB from the quantum limited performance (6.7 photons per bit at BER=10^{-6}). The best performance reported so far for coherent detection systems that used semiconductor laser was 34 photons per bit using a far more complicated phase shift keying (PSK) homodyne detection scheme [26].

The system described in this dissertation has the potential to provide a communication link between two geostationary satellites. The laser diode used had an average power limit of 30 mW (14.8 dBm). The total allowable losses between the transmitter and the receiver was therefore 78.3 dB. When 20 cm diameters transmitter and receiver telescopes are used, the diffraction limited propagation losses between two geostationary satellites 120° or 72,000 km apart is 66.5 dB. Therefore, a total of 11.8 dB is left to account for the optic component losses and the system design margin. An even larger margin may be obtained by incoherently combining the laser beams from a number of laser diodes to increase the transmitter power, as shown in [27, 28].

The rest of this dissertation is organized as follows. Chapter II gives a detailed analysis of the system performance using the widely used Gaussian approximation and the nearly exact Webb's approximation for the APD output photoelectrons. Chapter III describes the experimental setup including optics configuration, major components, and electronic circuits. The procedure and the results of the measurements are also presented. PPM slot timing recovery is covered in Chapter IV. Chapter V describes PPM word timing recovery. Chapter VI consists of the conclusions and the final remarks.

Chapter 2. Performance of Optical PPM Receiver with APD Photodetectors

In this chapter, the structure and the statistics of the output photocurrent of an APD photodetector are described. An efficient algorithm is developed to numerically evaluate the receiver performance using the nearly exact Webb's approximation for the true distribution function of the APD output. Comparisons are made between the use of Webb's approximation and the commonly used Gaussian approximation. It is shown that use of the Gaussian approximation seriously underestimates the optimal average APD gain and overestimates the bit error probability when the background radiation level and the APD leakage current are very low. Perfect timing recovery at the receiver is assumed in the analysis. The issue of timing recovery and the effects of jitter in the recovered timing signal will be addressed in detail in Chapter 4. Chapter 5.

2.1. APD Photodetectors

The structure of a silicon APD is shown in Figure 2.1 [29]. A thin layer of heavily doped n type (n^+) material is on the top. Next to it is a thin layer of less heavily doped p material and a thick layer of very lightly doped p material. This second p layer is labeled i for intrinsic because the material is so lightly doped that it can be considered to be intrinsic. A heavily doped p layer (p^+) is added at the bottom to reduce the contact resistance between the device and the outside circuit.

When a large reverse bias voltage is applied as shown in the diagram, depletion occurs at the p-n junction. Because the p layer adjacent to the n^+ layer is thin and less heavily doped, the depletion region can extend

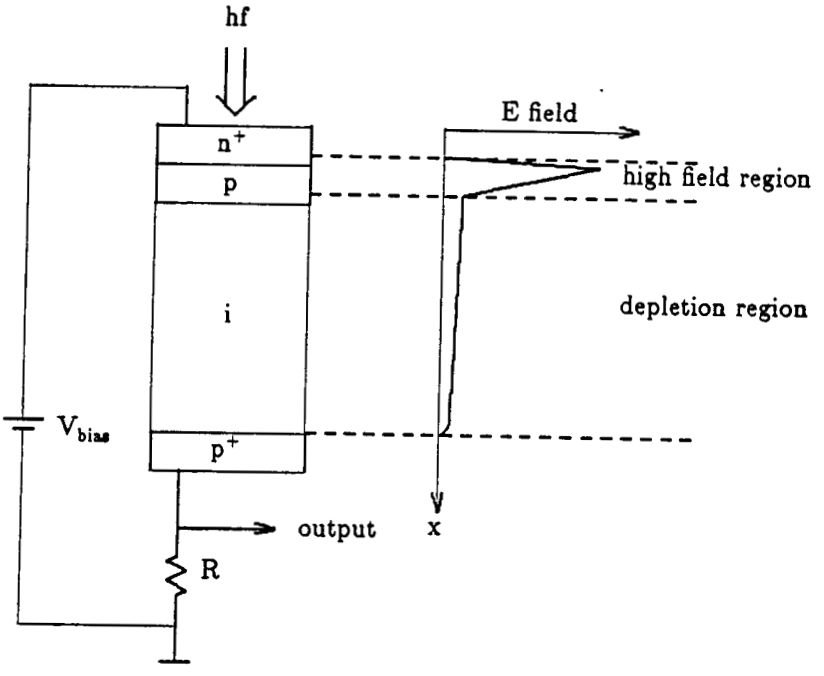

Figure 2.1. Structure of an APD and distribution of the electrical field

through the entire intrinsic layer if the bias voltage is high enough. Due to the differences in the doping levels, a large electric field appears across the thin junction between the n^+ and the p layers and a much smaller electric field appears across the thick intrinsic layer. Figure 2.1 also shows the distribution of the electrical field versus distance inside the APD.

Incident photons are mainly absorbed in the depleted intrinsic layer. Each absorbed photon generates an electron-hole pair. Under the influence of the electric field, electrons travel into the high field region where they can acquire sufficient energies to excite new electron-hole pairs through impact ionization. These secondary electrons and holes may collide with other molecules and excite even more secondary electron-hole pairs. The process goes on until the electrons and holes leave the high field region. As a result, the input primary photoelectron current is multiplied at the output of the APD. The multiplication gain is a random number because the impact ionizations occur at random. The thickness and the cross section area of the intrinsic layer is determined by a tradeoff between the quantum efficiency and the response speed of the device. Silicon APD's can have internal quantum efficiencies of nearly 100% at the wavelengths emitted by AlGaAs laser diodes (780-840nm) [29].

The number of photons which are absorbed in the APD is random and the probability that n photons are absorbed from an incident optical field of known intensity, $P_o(t)$ watts, over an interval of [t,t+T] is given by a Poisson distribution. The mean number of absorbed photons is given as $\bar{n}=(\eta/hf)\int_t^{t+T} P_o(t')dt'$, where η is the quantum efficiency, and hf is the incident photon energy. The probability that n absorbed primary photons

give rise to m photoelectrons at the output of the APD was given by McIntyre [14] and Conradi [15] as,

$$P(m \mid n) = \frac{n\Gamma(\frac{m}{1-k_{eff}}+1)}{m(m-n)!\,\Gamma(\frac{k_{eff}m}{1-k_{eff}}+1+n)}$$

$$[\frac{1+k_{eff}(G-1)}{G}]^{\frac{n+k_{eff}m}{1-k_{eff}}} \cdot [\frac{(1-k_{eff})(G-1)}{G}]^{m-n} \qquad (2.1.1)$$

where G is the average APD gain, $k_{eff}=\alpha/\beta$ with α and β the ionization coefficients of holes and electrons (i.e. $\alpha\equiv$probability of ionization per unit distance caused by a hole). The probability that m photoelectrons are output by the APD in response to $\bar{n}$ average absorbed primary photons can be written as

$$P(m=0 \mid \bar{n}) = e^{-\bar{n}} \ , \qquad (2.1.2)$$

$$P(m \mid \bar{n}) = \sum_{n=1}^{\infty} P(m \mid n)\frac{(\bar{n})^n}{n!}e^{-\bar{n}} \ , \qquad m \geq 1. \qquad (2.1.3)$$

The noise due to the randomness of the APD gain is called excess noise and is characterized by an excess noise factor defined as $F=E\{m^2\}/E^2\{m\}$. It can be shown that [15]

$$F = k_{eff}G+(2-1/G)(1-k_{eff}) \ . \qquad (2.1.4)$$

The excess noise factor increases as the ionization coefficient ratio and/or the average APD gain increase and $F\rightarrow 2$ as $G\rightarrow\infty$ and $k_{eff}\rightarrow 0$. Silicon APD's can have values of k_{eff} as low as 0.006 [30]. The average and mean square value of the number of photoelectrons output by an APD are given by

$$E\{m\} = G\bar{n} = \frac{\eta G}{hf}\int_{t}^{t+T} P_o(t')\,dt' \ , \qquad (2.1.5)$$

$$E\{m^2\} = G^2F\bar{n} = \frac{\eta G^2 F}{hf} \int_t^{t+T} P_o(t')\,dt' \quad . \tag{2.1.6}$$

2.2. Effect of Thermal Noise

The photocurrent output by the APD need to be amplified for further processing. A transimpedance amplifier is usually used to convert the high impedance current signal to a low impedance voltage signal. In a practical system, there always exist thermal noises from the load resistance seen by the APD (input impedance of the amplifier) and the thermal noise of the amplifier. These noises can be approximated to appear additive and have a Gaussian distribution with zero mean and a constant (white) power spectral density within a certain bandwidth. One can model the amplifier thermal noise as an equivalent current noise source at the input of a noiseless amplifier and use the total input current of the amplifier to analysis the receiver performance. The one sided spectral density of the load resistor thermal noise current is given by [31]

$$\frac{d<i_R^2>}{df} = \frac{4KT_R}{R}\ ,\ A^2/Hz \tag{2.2.1}$$

where the bracket means average value, K is Boltzmann's constant, and T_R is the absolute temperature. The amplifier thermal noise may be characterized approximately by an equivalent noise temperature defined as $T_e/T_R = <i_{total}^2>/<i_R^2>$, where i_{total} represents the total noise current from the APD load resistor and the subsequent amplifier. The spectral density of this total noise current may still be described by (2.2.1) with the absolute temperature T_R being replaced by T_e. When the data rates are high, for example, greater than 100 Mbits/sec, the bandwidth of the amplifiers has to be large and the noise spectrum within the bandwidth can not be assumed

to be white. Smith and Personick have given a more accurate model under these circumstances [32].

As mentioned in Chapter 1, the detection of PPM signals consists of a device which integrates the APD output current over each time slot and then determines the largest one through comparisons. The output of the integrator contains both APD photoelectrons and thermal noise electrons accumulated over the time slot. The electron charge due to the total thermal noise, x_t, is a Gaussian random variable with zero mean and variance given by

$$\text{var}\{x_t\} = \frac{4KT_e}{R}BT_s^2 = \frac{2KT_e}{R}T_s\,, \quad \text{Coulomb}^2 \tag{2.2.2}$$

where $B=1/2T_s$ is the noise bandwidth of an ideal integrator, and T_s is the PPM slot time.

The advantage of using an APD is that it provides internal gain for the primary signal photocurrent which would otherwise be obscured by the thermal noise of the load resistor and amplifier. Since the excess noise also increases with the APD gain, according to (2.1.4), there exists an optimal value for the average APD gain under which the system performance is optimal. In the absence of any thermal noise, the optimal APD gain is unity and the receiver reaches its ultimate performance which is the quantum limit.

2.3. Gaussian Approximation for the APD Output Photoelectrons

Since the total APD output consists of the discrete number of photoelectrons described by (2.1.1) and the additive continuous Gaussian thermal noise, the explicit expression of the probability density function is generally too complicated to use in practice. A widely used approximation is to

assume the discrete number of photoelectrons output by the APD as a continuous Gaussian random variable with the same mean and variance as given by (2.1.5) and (2.1.6). Since the amplifier thermal noise is Gaussian and independent of the APD output photoelectrons, the total electron charge integrated over a PPM time slot, x, is also a Gaussian random variable with mean and variance given as

$$p(x \mid \overline{n}) = \frac{1}{\sqrt{2\pi}\sigma} e^{-\frac{(x-\overline{x})^2}{2\sigma^2}} \tag{2.3.1}$$

$$\overline{x} = eG\overline{n} \text{ Coulomb} \tag{2.3.2}$$

$$\sigma^2 = e^2G^2F\overline{n} + eI_sT_s + \frac{2KT_eT_s}{R} \text{ Coulomb}^2 \tag{2.3.3}$$

where $\overline{n}$ is the average number of absorbed photons in a time slot of duration T_s, and I_s is the APD surface leakage current. The APD surface leakage current can be treated as a constant dc current because it is the part of the APD dark current which dose not get multiplied by the APD gain. There is also bulk leakage current in an APD which does get multiplied and it can be treated equivalently as a source of background radiation. If one defines the signal to noise ratio (SNR) as

$$SNR = \frac{\overline{x}^2}{\sigma^2} = \frac{(eG\overline{n})^2}{e^2G^2F\overline{n} + eI_sT_s + \frac{2KT_eT_s}{R}} . \tag{2.3.4}$$

The SNR increases as G increases from unity because the numerator of (2.3.4) increases while the main contribution to the denominator is still the thermal noise, $2KT_eT_s/R$, which is independent of the APD gain. However, the excess noise term, $e^2G^2F\overline{n}$, increases faster than the the numerator of (2.3.4) because F increases with G as shown in (2.1.4). As a result, the SNR starts to decreases as G becomes greater than a certain value when the excess noise becomes much larger than the thermal noise. In other words,

there exists an optimal average APD gain that maximum the SNR. The receiver performance does not solely depend on the SNR of the input signal and hence the optimal value of G that optimize the receiver performance may be slightly different.

The PPM word error probability (WEP) can be written as

$$\text{WEP} = 1 - \int_{-\infty}^{\infty} p(x \mid \bar{n}_1) \left[\int_{-\infty}^{x} p(x' \mid \bar{n}_0) dx' \right]^{Q-1} dx \qquad (2.3.5)$$

where $\bar{n}_1$ and $\bar{n}_0$ represent the average number of detected (absorbed) photons in the time slot where a transmitted PPM pulse is present and absent, respectively. In a real optical communication system,

$$\bar{n}_0 = \alpha_e \bar{n}_s + \bar{n}_{bl} + \bar{n}_{bg} \qquad (2.3.6)$$

and

$$\bar{n}_1 = \bar{n}_s + \bar{n}_{bl} + \bar{n}_{bg} \qquad (2.3.7)$$

where α_e is the extinction ratio of the laser diode emitting power between ON and OFF states, $\bar{n}_s$ is the average number of detected signal photons in a PPM pulse, $\bar{n}_{bl}$ is the equivalent average number of detected noise photons resulting from the APD bulk leakage current within T_s seconds, and $\bar{n}_{bg}$ is the average number of detected noise photons within T_s due to background radiation. The corresponding bit error rate is given by [12]

$$\text{BER} = \frac{Q}{2(Q-1)} \text{WEP} \quad . \qquad (2.3.8)$$

The above Gaussian approximation method has been used by Abshire [33 and Sorensen 34] to compute the receiver performance of optical PPM communication systems that used APD receivers.

2.4. Webb's Approximation for the APD Output Photoelectrons

A much more accurate approximation for the probability of the

number of photoelectrons output by an APD, (2.1.1), was given by Webb [24], as

$$P(m \mid \bar{n}) = \frac{1}{(2\pi\bar{n}G^2F)^{1/2}} \cdot \frac{1}{[1+\frac{m-G\bar{n}}{\bar{n}GF/(F-1)}]^{3/2}} \cdot \exp\left[-\frac{(m-G\bar{n})^2}{2\bar{n}G^2F(1+\frac{m-G\bar{n}}{G\bar{n}F/(F-1)})}\right] \quad (2.4.1)$$

for m values greater than $\bar{n}$. Equation (2.4.1) approaches a Gaussian density with mean $G\bar{n}$ and variance $FG^2\bar{n}$ when $|(m-G\bar{n})| << G\bar{n}$. Conditioned on the number of secondary photoelectrons, the probability density function of the total APD output can be written as

$$p(x \mid \bar{n}) = \sum_{m=0}^{\infty} p(x \mid m)P(m \mid \bar{n}) \ , \quad (2.4.2)$$

where $P(m \mid \bar{n})$ is given by (2.4.1), and $p(x \mid m)$ is the conditional probability density function of the APD output including thermal noise. Because the thermal noise is well characterized by the Gaussian distribution, $p(x \mid m)$ can be written as

$$p(x \mid m) = \frac{1}{\sqrt{2\pi\sigma}} e^{-\frac{(x-\bar{x}_m)^2}{2\sigma^2}} \quad (2.4.3)$$

$$\bar{x}_m = me + I_sT_s \quad (2.4.4)$$

$$\sigma^2 = (eI_s + \frac{2KT_e}{R})T_s \ . \quad (2.4.5)$$

The final BER can be obtained by substituting (2.4.1) through (2.4.5) into (2.3.5) and (2.3.8).

2.5. Comparison between the Gaussian Approximation and Webb's Approximation

Use of Gaussian approximation has the advantage of analytical simplicity. It has been shown that the calculated results of receiver performance

obtained with the Gaussian approximation were quite accurate in situations where the bulk leakage current of the APD is of order of nanoamperes and the background radiation levels are relatively high, i.e. when they produce more than 10 detected noise photons per time slot [16, 35, 36]. However, it was found in our experiments that use of the Gaussian approximation resulted substantial underestimation of the optimal average APD gain and overestimation of the receiver bit error rate when the number of detected noise photons was very small, e.g. $\bar{n}_0 < 1$.

Figure 2.2 shows the probabilities of number of photoelectrons output by an APD using the nearly exact Webb's approximation, (2.4.1), and a Gaussian probability density function with mean $G\bar{n}$ and variance $G_2F\bar{n}$, when $\bar{n}=1$ and $\bar{n}=120$, respectively. The two curves are close to each other only when $m \approx G\bar{n}$ and they differ substantially at the tails of the distribution which form the main contributions to the WEP given by (2.3.4). The smaller $\bar{n}$ is, the poorer the Gaussian approximation becomes. As shown in Figure 2.2, when $\bar{n}=1$, the Gaussian approximation is far off from that of Webb's approximation and almost half the Gaussian probability density function extends to the unphysical region of $m<0$.

The poor estimates of the optimal APD gain and receiver BER that result from use of the Gaussian approximation may be understood heuristically as follows. Under the extreme case when $\bar{n}_0=0$, the APD output from time slots where no light pulse was transmitted consists of only the thermal noise. The receiver BER may be reduced to the quantum limit by increasing the average APD gain because thermal noise is independent of the APD gain and the probability that the primary photoelectrons are obscured by the thermal noise approaches zero as the average APD gain increases. That

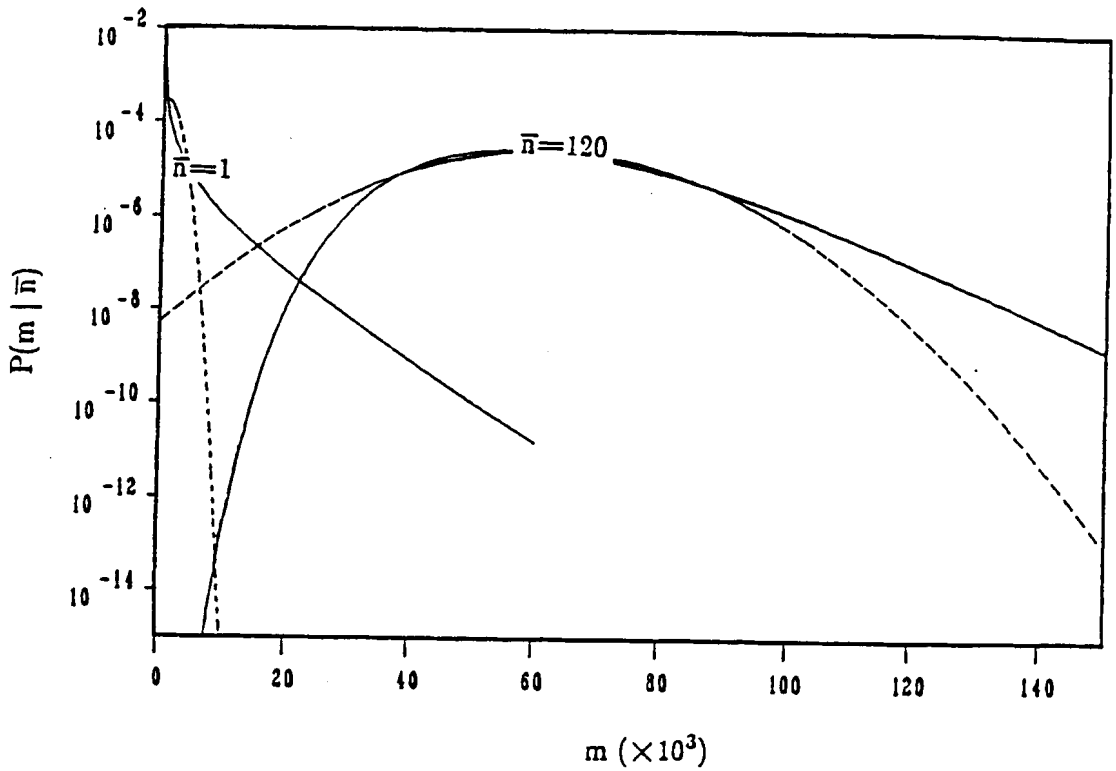

Figure 2.2. Probabilities of the number of photoelectrons output by an APD. The solid curves correspond to the Webb's approximation given by (2.4.1) and the dashed curves correspond to the Gaussian distributions with the same mean and variance as those given by (2.4.1). The APD parameters used were G=500 and k_{eff}=0.010. The average number of absorbed photons are $\bar{n}$=120 and $\bar{n}$=1, as indicated in the graph.

implies an optimal APD gain of infinity and an error probability approaching the quantum limit. On the other hand, when the Gaussian approximation is used, the probability that the APD output from the time slots which do contain a light pulse falls below a noise discrimination level, x_0, is given by

$$P(x \leq x_0) = \int_{-\infty}^{x_0} \frac{1}{(2\pi e^2 G^2 F \bar{n}_1)^{1/2}} \exp\left[\frac{-(x-eG\bar{n}_1)^2}{2e^2G^2F\bar{n}_1}\right]dx \qquad (2.5.1)$$
$$= \int_{-\infty}^{Th} \frac{1}{\sqrt{2\pi}} e^{-\frac{t^2}{2}} dt$$

where

$$Th = \frac{x_0 - eG\bar{n}_1}{(e^2G^2F\bar{n}_1)^{1/2}}. \qquad (2.5.2)$$

It can be seen that $Th \to 0$ as $G \to \infty$ for any value of x_0 because F is proportional to G. Consequently $P(x \leq x_0) \to 1/2$ as $G \to \infty$. That is to say that the optimal APD gain cannot be infinite and the minimal error probability never reduces to the quantum limit. In reality, $\bar{n}_0 > 0$ but as long as $\bar{n}_0$ is small, the Gaussian approximation still underestimates the optimal gain and overestimates the error probabilities. The smaller $\bar{n}_0$ gets, the bigger the discrepancies become.

Very low noise APD's can have bulk leakage currents of less than 10^{-12} amperes [37], which is equivalent to a background radiation noise photon absorption rate of the order 10^6/second. In some free space optical communication systems, background light levels are negligible when neither the Sun, the Earth or the Moon is not in the field of view of the receiver optics [17]. The extinction ratio of the laser between ON and OFF states can be kept small by biasing the laser diode below its threshold level. Therefore, the mean number of detected noise photons per PPM time slot, $\bar{n}_0$, can be well

below unity, at useful data transmission rates of 100 megabits/second and higher. The Gaussian approximation does not accurately model the APD output under these conditions and the more exact Webb's approximation for the APD output, (2.4.1) has to be used.

2.6. Numerical Computations Using Webb's Approximation

In this section, an efficient algorithm is described which uses Webb's approximation for the APD output photoelectrons.

2.6.1. Computing BER with Webb's Approximation

Substituting (2.4.1) through (2.4.5) into (2.3.5), the PPM word error probability can be written as

$$\mathrm{WEP} = \sum_{m=0}^{\infty} P(m \mid \bar{n}_1) \int_{-\infty}^{\infty} \phi(x,\bar{x}_m,\sigma^2) \cdot\{ 1-[\sum_{m'=0}^{\infty} P(m' \mid \bar{n}_0)\mathrm{Erf}(\frac{x-\bar{x}_{m'}}{\sigma})]^{Q-1}\} \, dx \tag{2.6.1}$$

where

$$\phi(x,\bar{x}_m,\sigma^2) \equiv \frac{1}{\sqrt{2\pi}\sigma} \exp\left[- \frac{(x-\bar{x}_m)^2}{2\sigma^2} \right] \tag{2.6.2}$$

is the Gaussian probability density function, $\bar{x}_m$ and $\bar{x}_{m'}$ are the mean values of the electron charge for given number of secondary electrons m and m' , respectively, and

$$\mathrm{Erf}(u) \equiv = \int_{-\infty}^{u} \frac{1}{\sqrt{2\pi}} e^{-\frac{t^2}{2}} dt \ . \tag{2.6.3}$$

Since $\mathrm{Erf}(\frac{x-\bar{x}_{m'}}{\sigma}) = 1-\mathrm{Erf}(-\frac{x-\bar{x}_{m'}}{\sigma})$, $\bar{x}_{m'} << \bar{x}_m$, and x varies about its mean during the course of the outer integration in (2.6.1), $\mathrm{Erf}(-\frac{x-\bar{x}_{m'}}{\sigma}) << 1$. We can then use a Taylor expansion for the Q-1 power

and approximate the expression inside the braces of (2.6.1) and rewrite WEP as

$$\mathrm{WEP} = (Q-1)\sum_{m=0}^{\infty} P(m \mid \bar{n}_1)\int_{-\infty}^{\infty} \phi(x,\bar{x}_{m,}\sigma^2) \cdot \sum_{m'=0}^{\infty} P(m' \mid \bar{n}_0)\mathrm{Erf}(-\frac{x-\bar{x}_{m'}}{\sigma})dx \qquad (2.6.4)$$

This is equivalent to the union bound for the word error probability.

In a numerical evaluation of (2.6.4), the two infinite sums and the infinite integral have to be truncated to finite terms and limits. Equation (2.6.4) can be rewritten as

$$\mathrm{WEP} = (Q-1)\sum_{m=0}^{M} P(m \mid \bar{n}_1)\int_{A_m}^{B_m} \phi(x,\bar{x}_{m,}\sigma^2) \cdot \sum_{m'=0}^{M'} P(m' \mid \bar{n}_0)\mathrm{Erf}(-\frac{x-\bar{x}_{m'}}{\sigma})dx + \epsilon \qquad (2.6.5)$$

where M, M′ , A_m, and B_m are the new limits of the sums and the integral. The resultant truncation error, ϵ, consists of three parts corresponding to each truncation. A set of bounds for those errors will be given in the next subsection, along with a procedure for choosing the appropriate limits of the sums and the integral.

It should be noted that Webb's approximation is only valid for $m > \bar{n} > 0$ and terms corresponding to $m \leq \bar{n}_1$ and $m' \leq \bar{n}_0$ have to be treated separately. The contributions from the terms for $m \leq \bar{n}_1$ in the outer sum of (2.6.5) are negligible since $P(m \mid \bar{n}_1) \rightarrow 0$ for values of m which are much less than the mean, $G\bar{n}_1$. On the other hand, the contributions from the terms for $m' \leq \bar{n}_0$ in the inner sum of (2.6.5) cannot be neglected when $\bar{n}_0 \ll 1$. The probability that no secondary electrons are output by the APD, $P(m' = 0 \mid \bar{n}_0)$, is given by $e^{-\bar{n}_0}$, the same as the probability that no primary

electron is generated based on the Poisson distribution. If $\bar{n}_0$ approach zero, which occurs at high data rates , low background radiation levels, and low APD bulk leakage currents, the probability that no secondary electron is output by the APD approaches unity. In other words, when $\bar{n}_0 \ll 1$, the contributions from the terms for $m' = 0$ in (2.6.5) dominate. Consequently, if the truncation error is negligible and $\bar{n}_0 < 1$, equation (2.6.5) should be modified as

$$\begin{aligned} WEP \approx (Q-1) \sum_{m=\bar{n}_1+1}^{M} P(m \mid \bar{n}_1) \int_{A_m}^{B_m} \phi(x, \bar{x}_m, \sigma^2) \\ \cdot \sum_{m'=1}^{M'} P(m' \mid \bar{n}_0) Erf\left(-\frac{x-\bar{x}_{m'}}{\sigma}\right) dx \\ + (Q-1) \sum_{m=\bar{n}_1+1}^{M} P(m \mid \bar{n}_1) \cdot e^{-\bar{n}_0} \cdot \int_{A_m}^{B_m} \phi(x, \bar{x}_m, \sigma^2) Erf\left(-\frac{x-I_s T_s}{\sigma}\right) dx \end{aligned} \quad (2.6.6)$$

where $I_s T_s$ is the value of $\bar{x}_{m'}$ at $m' = 0$, and $P(m \mid \bar{n}_1)$, $P(m' \mid \bar{n}_0)$ are given by Webb's approximation, (2.4.1). The contribution from the second term in (2.6.6) increases as $\bar{n}_0$ decreases. In the extreme case when $\bar{n}_0 = 0$, the second term in (2.6.6) becomes the only contribution to WEP and the first term vanishes because

$$\begin{aligned} &\sum_{m=\bar{n}_1}^{M} P(m \mid \bar{n}_1) \int_{A_m}^{B_m} \phi(x, \bar{x}_m, \sigma^2) \sum_{m'=1}^{M'} P(m' \mid \bar{n}_0) Erf\left(-\frac{x-\bar{x}_{m'}}{\sigma}\right) dx \\ &\leq \sum_{m'=1}^{\infty} P(m' \mid \bar{n}_0 T_s) \\ &= 1 - e^{-\bar{n}_0} \rightarrow 0, \quad \text{as } \bar{n}_0 \rightarrow 0 \end{aligned} \quad (2.6.7)$$

2.6.2. The Truncation Errors

From Eq.(2.6.5), the truncation error is

$$\epsilon = \epsilon_1 + \epsilon_2 + \epsilon_3 \quad (2.6.8)$$

$$\epsilon_1 = (Q-1) \sum_{m=M+1}^{\infty} P(m \mid \bar{n}_1) \cdot \int_{-\infty}^{\infty} \phi(x,\bar{x}_m,\sigma^2) \sum_{m'=0}^{\infty} P(m' \mid \bar{n}_0) \mathrm{Erf}(-\frac{x-\bar{x}_{m'}}{\sigma})dx \tag{2.6.9}$$

$$\epsilon_2 = (Q-1) \sum_{m=0}^{M} P(m \mid \bar{n}_1) \cdot \int_{x>B_m,\ x<A_m} \phi(x,\bar{x}_m,\sigma^2) \sum_{m'=0}^{\infty} P(m' \mid \bar{n}_0) \mathrm{Erf}(-\frac{x-\bar{x}_{m'}}{\sigma})dx \tag{2.6.10}$$

$$\epsilon_3 = (Q-1) \sum_{m=0}^{M} P(m \mid \bar{n}_1) \int_{A_m}^{B_m} \phi(x,\bar{x}_m,\sigma^2) \cdot \sum_{m'=M'+1}^{\infty} P(m' \mid \bar{n}_0) \mathrm{Erf}(-\frac{x-\bar{x}_{m'}}{\sigma})dx \ . \tag{2.6.11}$$

A set of bounds for ϵ_1, ϵ_2, and ϵ_3 will be given next.

Since probabilities do not exceed unity and $\mathrm{Erf}(-\frac{x-\bar{x}_{m'}}{\sigma}) \leq 1$ for any value of x,

$$\epsilon_2 < (Q-1) \sum_{m=0}^{M} P(m \mid \bar{n}_1) \cdot \int_{x>B_m,\ x<A_m} \phi(x,\bar{x}_m,\sigma^2)dx \tag{2.6.12}$$

The integrand in (2.6.12) is now a Gaussian density function and A_m and B_m can be chosen such that the integration is a constant for any value of m. Then,

$$\epsilon_2 < (Q-1) \int_{x>B_m,\ x<A_m} \phi(x,\bar{x}_m,\sigma^2)dx \tag{2.6.13}$$

A_m and B_m can be set to be symmetric about $\bar{x}_m$ and deviate by an amount which is determined by the specified maximum value for ϵ_2. For example, $A_m = \bar{x}_m - 6\sigma$ and $B_m = \bar{x}_m + 6\sigma$ for $\epsilon_2 < (Q-1) \times 10^{-9}$.

Next, since $\bar{x}_m$ and $\bar{x}_{m'}$ become further apart as m increases, the value of the integration in (2.6.9) decreases monotonically as m increases. Therefore,

$$\epsilon_1 < (Q-1)\sum_{m=M+1}^{\infty} P(m \mid \bar{n}_1)$$
$$\cdot\int_{-\infty}^{\infty}\phi(x,\bar{x}_{M+1},\sigma^2)\sum_{m'=0}^{\infty}P(m' \mid \bar{n}_0)\cdot Erf(-\frac{x-\bar{x}_{m'}}{\sigma})dx$$
$$<(Q-1)\int_{-\infty}^{B_{M+1}}\phi(x,\bar{x}_{M+1},\sigma^2)\sum_{m'=0}^{\infty}P(m' \mid \bar{n}_0)\cdot Erf(-\frac{x-\bar{x}_{m'}}{\sigma})dx$$
$$\approx(Q-1)\int_{A_{M+1}}\phi(x,\bar{x}_{M+1},\sigma^2)\sum_{m'=0}^{M'}P(m' \mid \bar{n}_0)\cdot Erf(-\frac{x-\bar{x}_{m'}}{\sigma})dx \qquad (2.6.14)$$

Hence it is safe to choose M such that the integral given in (2.6.14) is less than a specified value. The integral in (2.6.14) is identical to that in (2.6.5) when taking m=M+1, so proper values of M can be determined during the course of the numerical evaluation of (2.6.5), rather than through trials of separate computations of (2.6.14). Every time the index of the outer sum is increased, i.e. a new term is computed and accumulated for the outer sum of (2.6.5), the values of the integral within this new term is compared with a preset limit, for example, $10^{-9}/(Q-1)$ for $\epsilon_1<10^{-9}$. The process terminates when the value of the integral in the next new term becomes less than the preset limit.

Finding the proper value of M' is lengthy. First, since $Erf(-\frac{x-\bar{x}_{m'}}{\sigma})\leq 1$ for any value of x,

$$\epsilon_3 \leq (Q-1)\sum_{m=0}^{M}P(m \mid \bar{n}_1)\int_{A_m}^{B_m}\phi(x,\bar{x}_m,\sigma^2)dx\cdot\sum_{m'=M'+1}^{\infty}P(m' \mid \bar{n}_0)$$
$$< (Q-1)\sum_{m'=M'+1}^{\infty}P(m' \mid \bar{n}_0). \qquad (2.6.15)$$

Substituting (2.4.1) for $P(m' \mid \bar{n}_0)$ in (2.6.15) and bounding the sum by the associated integral gives,

$$\epsilon_3 < (Q-1)\int_{M'}^{\infty}\frac{1}{(2\pi\bar{n}_0G^2F)^{1/2}}\cdot\frac{1}{[1+\frac{m'-G\bar{n}_0}{\bar{n}_0GF/(F-1)}]^{3/2}}$$

$$\cdot\exp\left[-\frac{(m'-G\bar{n}_0)^2}{2\bar{n}_0G^2F(1+\frac{m'-G\bar{n}_0}{G\bar{n}_0F/(F-1)})}\right]dm' \qquad (2.6.16)$$

Since, for $m' > G\bar{n}_0$,

$$(1+\frac{m'-G\bar{n}_0}{G\bar{n}_0F/(F-1)})<(1+\frac{m'-G\bar{n}_0}{G\bar{n}_0}) = \frac{m'}{G\bar{n}_0}$$

then,

$$2\bar{n}_0G^2F(1+\frac{m'-G\bar{n}_0}{G\bar{n}_0F/(F-1)})<2GFm' \ .$$

The exponent in (2.6.16) satisfies

$$\frac{(m'-G\bar{n}_0)^2}{2\bar{n}_0G^2F(1+\frac{m'-G\lambda_0T_s}{G\bar{n}_0F/(F-1)})} > \frac{(m'-G\bar{n}_0)^2}{2GFm'}$$

$$> \frac{m'^2-2m'\,G\bar{n}_0}{2GFm'}$$

$$= \frac{m'-2G\bar{n}_0}{2GF}.$$

Furthermore,

$$[1+\frac{m'-G\bar{n}_0}{\bar{n}_0GF/(F-1)}]^{3/2} > [\frac{m'-G\bar{n}_0}{\bar{n}_0GF/(F-1)}]^{3/2},$$

then,

$$\epsilon_3 < \frac{Q-1}{(2\pi\bar{n}_0G^2F)^{1/2}}\int_{M'}^{\infty}\frac{1}{[\frac{m'-G\bar{n}_0}{\bar{n}_0GF/(F-1)}]^{3/2}}$$

$$\cdot\exp\left[-\frac{m'-2\bar{n}_0G}{2GF}\right]dm' \qquad (2.6.17)$$

Let $u \equiv \frac{2GF}{m'-\bar{n}_0G}$, so that

$$\epsilon_3 < \frac{1}{2}(Q-1)\bar{n}_0 e^{\bar{n}_0/2F} \cdot \sqrt{\frac{F}{\pi(F-1)^3}} \cdot \int_0^{\frac{2GF}{M' - \bar{n}_0 G}} \frac{1}{\sqrt{u}} e^{-\frac{1}{u}} du \qquad (2.6.18)$$

The proper value of M' is found by setting the upper limit of the integral in (2.6.18) such that ϵ_3 is smaller than a desired value. Following are two examples with two sets of the parameters used in the experiments described in Chapter 3.

Example 1:

$\bar{n}_0=1$, $k_{eff}=0.01$, $G=500$, $Q=4$. For $\epsilon_3<10^{-9}$,

$$\frac{2GF}{M' - \bar{n}_0 G} < 0.067, \quad \text{or } M' > 105{,}000$$

Example 2:

$\bar{n}_0=0.01$, $k_{eff}=0.01$, $G=700$, $Q=4$. For $\epsilon_3<10^{-9}$,

$$\frac{2GF}{M' - \bar{n}_0 G} < 0.095, \quad \text{or } M' > 133{,}000$$

2.6.3. Numerical Computation Procedure

The procedure to evaluate the receiver performance, (2.6.6), is as follows. First, the limits of the integral, A_m and B_m, for a fixed value of the index of the outer sum, m, are computed. Corresponding to each value of the integration variable, x, the inner sum and then the integrand are evaluated. The result of the integration is multiplied by $P(m \mid \bar{n}_1)$ and the product is then accumulated. The process repeats for all values of m from zero to M. The computer program used was written in FORTRAN as listed in Appendix A. The subroutines for the integration and error function, Erf(x), in (2.6.6) were called from the IMSL library.

Even more computation time can be saved by increasing the summa-

tion indices in (2.6.6) by increments larger than unity with subsequent multiplication of individual terms by the value of the increments. Special care must be taken for small values of m' where $P(m' \mid \bar{n}_0)$ changes rapidly as m' increases. Experience showed that m' should be incremented by unity over the range $1 \leq m' < 100$. Trial and error methods indicated that differences in the results from trial to trial could be maintained below 1% for increments of m and m' (when $m' \geq 100$) which were of the order of several hundred.

In the numerical computations, the subroutine for the integration was set to have a relative error less than 1%. The limits of the two sums in (2.6.6), M and M' , were chosen according to the procedure given in the previous subsection. The proper increments for the indices m and m' (when $m' \geq 100$) of the sums in (2.6.6) were 2,200 and 500 respectively. Therefore about 50 values of m were needed to estimate the outer sum and about 350 values of m' (including 100 points for $0 \leq m' \leq 99$) were needed to estimate the inner sum. As a result, It required about two CPU minutes to compute one value of WEP on a VAX 8600 computer.

Chapter 3. Experimental Setup and Measurements

A laboratory optical communication system was built with an AlGaAs laser diode and a silicon APD. The system used Q=4 PPM signaling and operated at a source data rate of 25×10^6 bits per second. The final receiver BER was measured as a function of the average number of detected photons per information bit and the results were compared with the numerical results from the theoretical analysis of Chapter 2. Perfect timing recovery at the receiver was assumed by using the same PPM slot clock and the word clock as those in the transmitter. The timing recovery system and the receiver BER when using the recovered timing signals will be given in Chapter 4 and Chapter 5.

3.1. Optical Setup

A schematic diagram of the entire optical setup is shown in Figure 3.1. The transmitter consisted of an AlGaAs laser diode and a collimating lens. Channel losses between the transmitter and the receiver were simulated by a set of neutral density attenuators ($\sim$60dB). An optical filter was formed with a diffraction grating in Littrow configuration [38] that included the focal lens next to the attenuators, the collimation lens in front of the grating, and the iris at the focal plane. The lens behind the iris was used to focus the filtered light beam to the small photosensitive area of the APD.

The laser diode (Hitachi HL8314) had a wavelength of 833 nm and a maximum cw power limit of more than 30 mW. The temperature of the diode was kept at 20° C by the use of a temperature compensated mount. The output power vs. injection current and the modulation levels are plotted in Figure 3.2. The bias level was set at 40 mA, which was below the

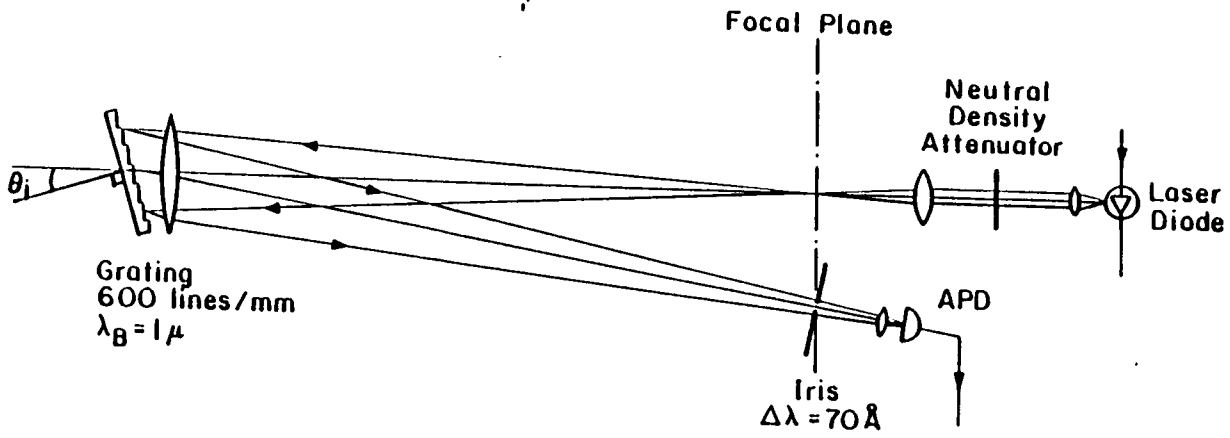

Figure 3.1. Optics setup

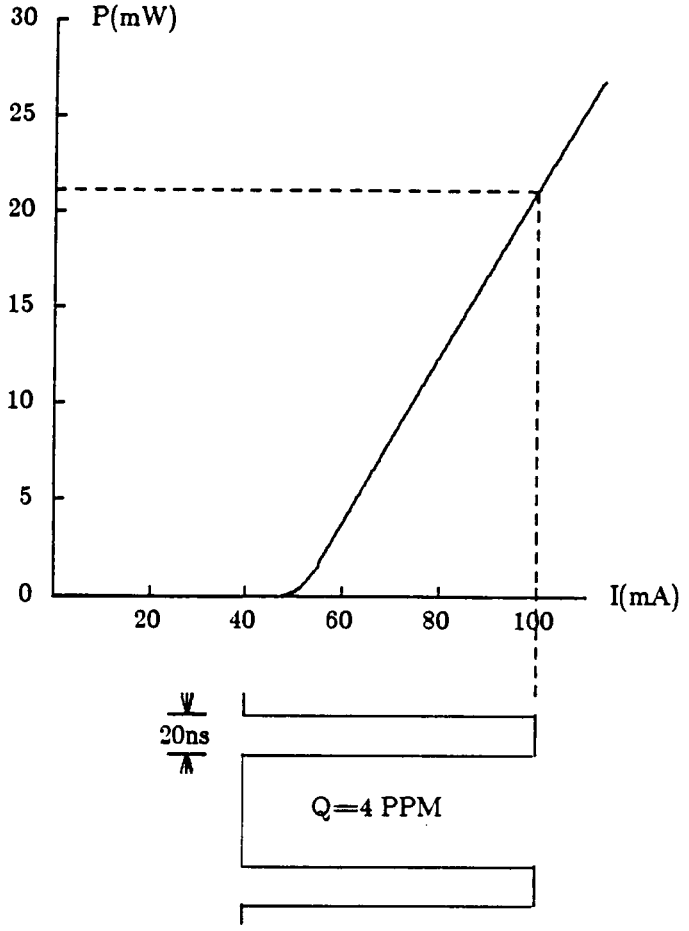

Figure 3.2. P-I curve of the laser diode.

lasing threshold current in order to keep a high extinction ratio of the laser diode between ON and OFF states. The peak power of the laser diode was set below the cw power limit, as shown in Figure 3.2, to prolong the lifetime of the device.

An optical filter in front of the APD was necessary to cut out background radiation and broad band noise emission from the pulsed laser diode. A diffraction grating filter was used for the convenience of adjustability of both center frequency and bandwidth. A simple interference filter with fixed center frequency and bandwidth could be substituted. The angular dispersion of the grating is given by [39]

$$\frac{d\theta}{d\lambda} = \frac{\tan\theta_i}{\lambda} \tag{3.1.1}$$

where θ is the angle of the diffracted beam, λ is the wavelength, and θ_i is the angle of the incident beam with respect to the normal vector of the grating surface, as shown in Figure 3.1. The bandwidth of the light, $\Delta\lambda$, that passes through the iris can be derived from (3.1.1) as

$$\Delta\lambda \approx \frac{d\lambda}{d\theta}\Delta\theta = \frac{\lambda}{\tan\theta_i}\cdot\frac{f}{\phi_{iris}} \tag{3.1.2}$$

where f is the distance from the grating to the focal plane, and ϕ_{iris} is the diameter of the iris. The resolution power of the grating is defined as the ratio of the minimum resolvable wavelength difference to the center wavelength and is given by

$$\frac{\Delta\lambda_{min}}{\lambda} = \left(\frac{2W}{\lambda}\sin\theta_i\right)^{-1} \tag{3.1.3}$$

where W is the width of the grating which is illuminated by the incident beam. Since $\Delta\lambda_{mim}$ is a measure of how sharply the frequency response of the filter cuts off at the limits of the passband, a good optical filter should

have $\Delta\lambda_{min} << \Delta\lambda$. In the system constructed, ϕ_{iris}= 2mm, f=1000mm, θ_i= 15°, and W ≃20mm. Therefore, the bandwidth of the filter was $\Delta\lambda \approx$7nm, and the minimum resolvable wavelength difference was $\Delta\lambda_{min} \approx$ 0.067nm. The grating used had 600 lines/mm and was blazed for the wavelength of λ=1μm. The transmission efficiency was measured to be 30∼40%. With proper blazing of the groves, a diffraction grating filter can achieve an efficiency of 80% [39].

The APD used was an RCA-C30902S which had extremely low noise and low bulk leakage current. This device had a useful diameter of the photosensitive surface of 0.5mm and a frequency response up to 1 GHz. Typical rise and fall times were 0.5ns. The typical quantum efficiency at λ=830 was 77% [37].

No special attention was paid to the transmission efficiency of the optical components. In a practical system, however, all the optics should be coated for antireflection, the grating filter should be replaced with an interference filter to reduce the size of the system, and the elliptical beam profile emitted by the laser diode should be corrected to a circular one through the use of a prism pair [40].

3.2. Transmitter Electronics

A block diagram of the transmitter circuit is shown in Figure 3.3. The binary data source consisted of a binary word generator (Hewlett Packard 8018A) which was driven at 25 MHz by an external clock provided by the PPM modulator. The electronic circuits of both the transmitter and receiver were built with Motorola MC10K series emitter coupled logic (ECL) chips on triple layer wire wrapping boards (Augat UVG series). These ECL

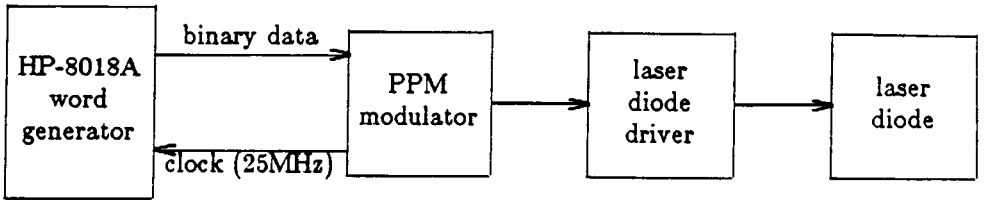

Figure 3.3. The transmitter.

circuits had rise and fall times of 2~3 ns and a potential operating speed of about 250 MHz [41]. The laser diode driver, which had a temperature control unit, was provided by the NASA Goddard Space Flight Center.

The details of the PPM modulator are shown in Figure 3.4. The timing base was provided by the crystal oscillator (Greenray ZY7410) and a counter. The crystal oscillator generated the PPM slot clock at 50 MHz. The output from the least significant bit (LSB) of the counter provided a clock at 25MHz for the binary data sequences. An OR gate was used to generate a PPM word synchronization signal which was normally "high", and became "low" when the counter state was "00". The circuit worked as follows. Shift register #1 was used in series shift mode to temporarily store the input binary data. The two binary bits in shift register #1 were encoded as a PPM word through a 1-to-4 address decoder. The resultant PPM word was loaded in parallel into shift resistor #2 at the time slot when the PPM word synchronization signal was in "low" state, and shifted out in series afterwards. The one to one correspondence between the binary pattern and the PPM word is shown in Figure 3.5. A timing diagram of this PPM modulator is shown in Figure 3.6. The bit time of the binary data was 40ns and the pulsewidth of the output PPM signal was 20ns. The time delay from the input binary data to the output PPM word was equal to the time span of two binary bits, 80ns.

3.3. Receiver Electronics

A block diagram of the entire receiver electronic circuit is shown in Figure 3.7. Descriptions of this circuit will be divided into the following subsections, except for the PPM slot and word clock recovery circuits drawn

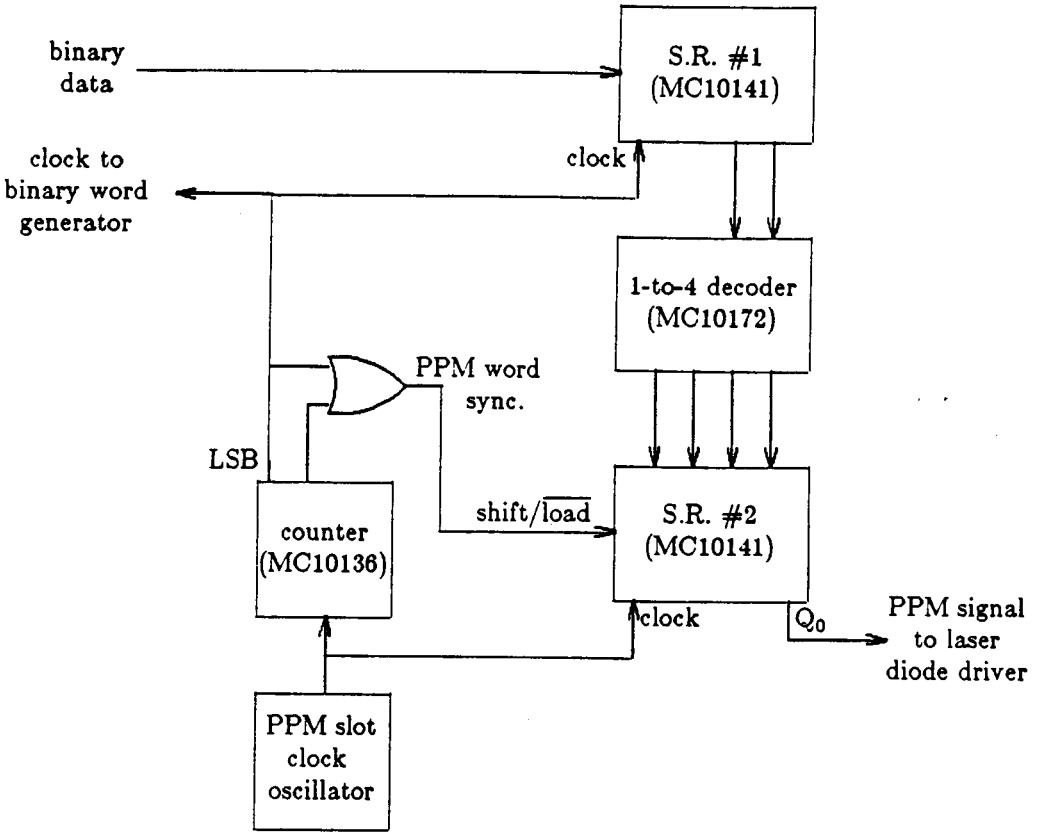

Figure 3.4. PPM modulator

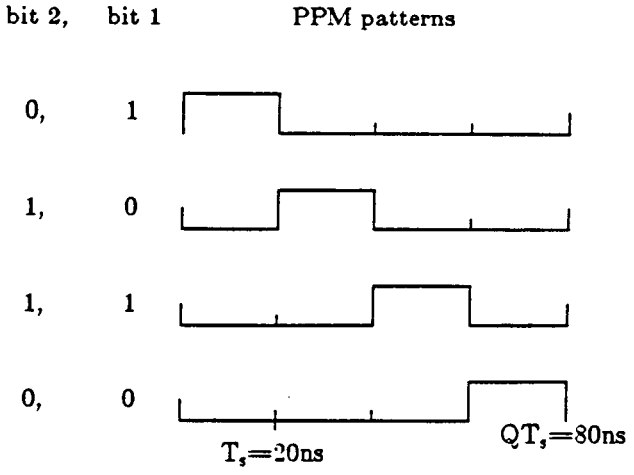

Figure 3.5. Binary patterns and the corresponding PPM patterns

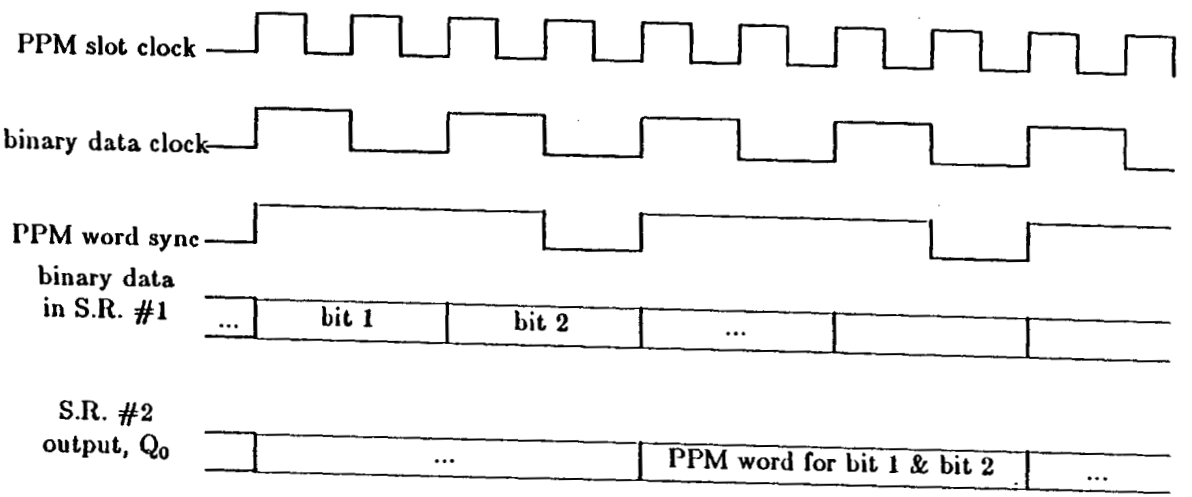

figure 3.6. Timing diagram of the PPM modulator

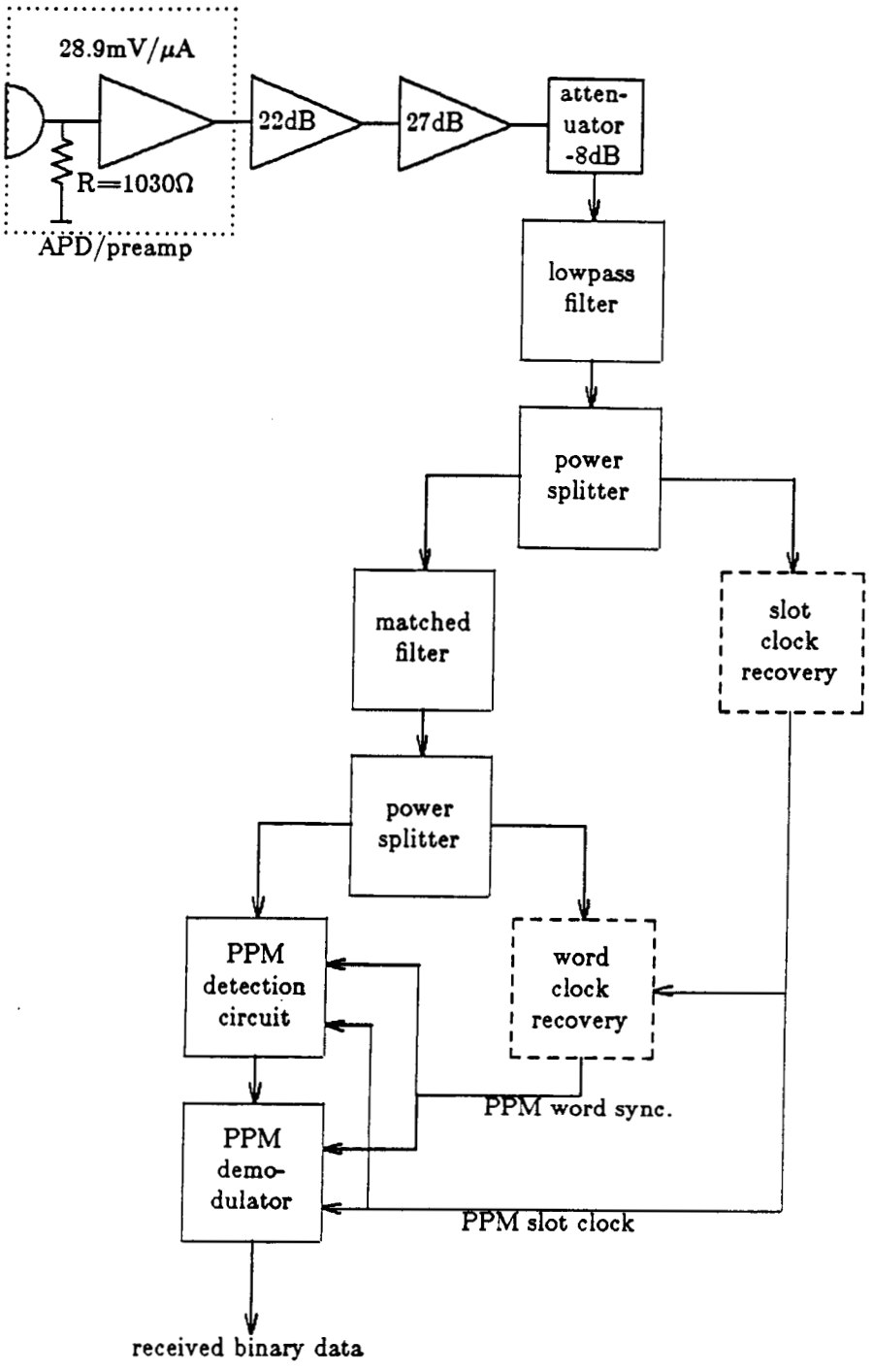

Figure 3.7. Block diagram of the receiver electronics.

in dashed blocks in Figure 3.7. Common transmitter/receiver clocks were used in the experiments and measurements described in this chapter. The analysis and experiments concerned with the timing recovery will be given in Chapters 4 and 5.

3.3.1. Signal Amplification

The output photocurrent from the APD was typical on the order of one microampere or less and further amplification was necessary for the following signal processing. The first stage amplifier, or the preamplifier, had to be designed very carefully because the receiver performance depended mainly on the noise at this stage.

The APD and the preamplifier enclosed in the dotted line in Figure 3.7 were in the same package which was electrically shielded. The package was made by Analog Modules, Inc.. The preamplifier had a gain of 28.9mV/μA, a bandwidth of 45KHz—440MHz, and an equivalent input noise current of 4.4pA/$\sqrt{\text{Hz}}$ according to the data sheet supplied by the manufacture. The load resistance seen by the APD was R=1030Ω. The APD gain could be adjusted by slightly changing the reverse bias voltage.

A Mini-Circuits ZFL500 power amplifier with 22dB of gain, and a Trontech P150D power amplifier with 27dB gain, were used to further amplify the signal from the preamplifier. The former had a bandwidth of 50KHz—500MHz and a noise figure of 5.3dB. The latter had a bandwidth of 30kHz—150MHz and a noise figure of 5dB. The noise figures were the ratios of the variance of the equivalent input noise to that of the input resistor of the amplifier. The thermal noises from these two amplifier were insignificant compared to the noise of the preamplifier. The resistive

attenuator following the amplifiers was used for adjustment of the signal levels.

The lowpass filter after the attenuator, Allen Avionics F2971, was used to limit the noise acceptance bandwidth of the circuit. The filter was also a part of the matched filter to be described in the next subsection. The cutoff frequency of the lowpass filter was 97MHz, which was determined primarily by the PPM pulsewidth and the design of the matched filter. The two 1-to-2 power splitters in Figure 3.7 were Mini-Circuits ZMSC-2-1, which had a bandwidth of 100KHz-400MHz. The lower limit of combined bandwidth of the entire circuit was 100KHz, and therefore, the effects of low frequency 1/f noise could be neglected.

3.3.2. The Matched Filter

The integration of the APD output photocurrent over each time slot required by the maximum likelyhood PPM receiver design can be realized in hardware with the use of a matched filter. When the pulses output by the APD are assumed to have a rectangular pulse shape and a pulsewidth of T_s seconds, the impulse response of a matched filter should have the same rectangular pulse shape [42]. The output from such a matched filter at time t is equal to the integration of the input signal over the interval $[t,t+T_s]$. If the filter is sampled every T_s second at the PPM slot boundaries, each sample is equal to the integration of the APD output photocurrent over the previous time slot.

The matched filter used is shown in Figure 3.8, which had a tapped delay line structure as described in [42]. The time delays consisted of RG316 coax cables cut to the proper lengths. The power splitter and the

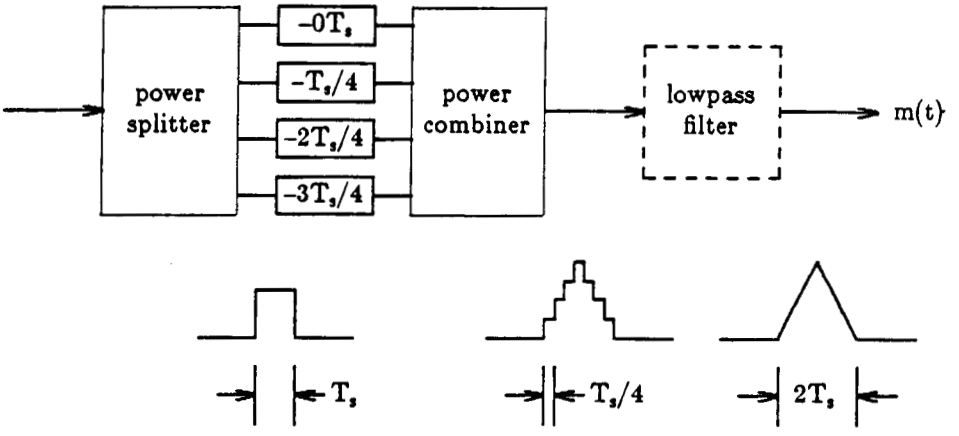

Figure 3.8. The matched filter

power combiner in Figure 3.8 were Mini-Circuit ZMSC-4-1 1-to-4 power splitters, which had a bandwidth of 100KHz-200MHz. The lowpass filter, shown as the dashed block in Figure 3.8, was actually the same lowpass filter shown in Figure 3.7, since the power splitter and the lowpass filter were both linear devices and the order in which the signal passes through each of them could be interchanged. The filter was necessary to smooth out the staircase output from the power combiner of Figure 3.8. Lowpass filters of 50MHz, 97MHz, and 200MHz cutoff frequencies were tested to see which gave the smallest receiver BER. The one with 97MHz cutoff frequency was finally chosen.

The response of an ideal matched filter to a rectangular input pulse is a symmetric triangle waveform of base $2T_s$. A value at the top of the triangle is proportional to the total energy contained in the received optical pulse. In practice, the triangular pulse shape will be distorted because there can only be finite number of delay taps in a real implementation of the matched filter. The triangular pulse shape output from the matched filter of Figure 3.8 can be derived as follows. A rectangular pulse input to the power splitter can be expressed as

$$\mathrm{rec}(t) = u(t) - u(t-T_s) \tag{3.3.1}$$

where u(t) is the unity step function, i.e. u(t)=0 for $t<0$ and u(t)=1 for ≥ 0. The signal input to the lowpass filter is then

$$y(t) = \mathrm{rec}(t) + \mathrm{rec}(t-T_s/4) + \mathrm{rec}(t-2T_s/4) + \mathrm{rec}(t-3T_s/4). \tag{3.3.2}$$

Since the circuit is linear, the output of the lowpass filter can be written as

$$m(t) = m_0(t) + m_0(t-T_s/4) + m_0(t-2T_s/4) + m_0(t-3T_s/4) \tag{3.3.3}$$

where $m_0(t)$ is the response of the lowpass filter to a single input rectangular pulse. The Fourier transforms of $m_0(t)$ can be expressed as

$$M_0(\omega) = REC(\omega)H(\omega) \tag{3.3.4}$$

where REC(ω), $H(\omega)$ are the Fourier transforms of rec(t) and the impulse response of the lowpass filter, respectively. The Fourier transform of (3.3.1) is given by

$$X(\omega) = \frac{1}{j\omega} - \frac{1}{j\omega}e^{-j\omega T_s} \ . \tag{3.3.5}$$

Assuming the lowpass filter has a "brick wall" frequency response, i.e.,

$$H(\omega) = \begin{cases} 1 & |\omega| \leq 2\pi B \\ 0 & \text{otherwise,} \end{cases} \tag{3.3.6}$$

it follows that

$$\begin{aligned} m_0(t) &= \frac{1}{2\pi}\int_{-2\pi B}^{2\pi B}\frac{1}{j\omega}(1 - e^{-j\omega T_s})e^{j\omega t}d\omega \\ &= \frac{1}{2\pi}\int_{-2\pi B}^{2\pi B}\frac{\sin\omega t}{\omega}d\omega - \frac{1}{2\pi}\int_{-2\pi B}^{2\pi B}\frac{\sin\omega(t-T_s)}{\omega}d\omega \\ &= \frac{1}{\pi}\int_{0}^{2\pi Bt}\frac{\sin x}{x}dx - \frac{1}{\pi}\int_{0}^{2\pi B(t-T_s)}\frac{\sin x}{x}dx. \end{aligned} \tag{3.3.7}$$

The resultant distorted triangle is obtained by substituting (3.3.7) into (3.3.3). Figure 3.9 shows a normalized and centered version of this triangle waveform, i.e. $m_1(t)=m(t+0.875T_s)/4$. The dotted line in Figure 3.9 represents the perfect triangle pulse shape output from an ideal matched filter.

3.3.3. PPM Detection Circuit

The received PPM pulse sequence was detected and regenerated from the noisy signals output by the matched filter with the circuit shown in figure 3.10. The signal output from the matched filter was first split into four branches by a power splitter (Mini-Circuit ZMSC-4-1) and then delayed by 0, 1, 2, or 3 time slots. Those four signals were sampled simultaneously at the end of the last time slot of a PPM word. Each sample

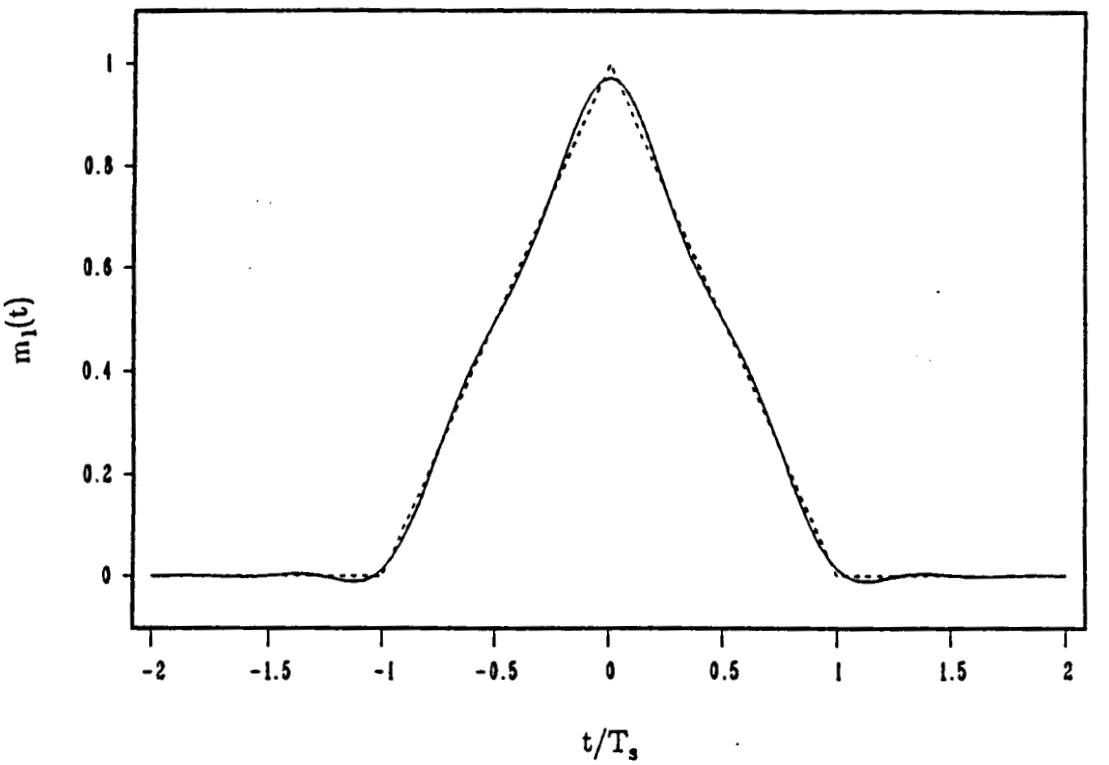

Figure 3.9. The output of the matched filter, $m_1(t)$, in response to a rectangular input pulse of width T_s. The dotted line is the response of an ideal matched filter. The bandwidth of the lowpass filter shown in Figure 3.8 is taken to be $B=2/T_s$.

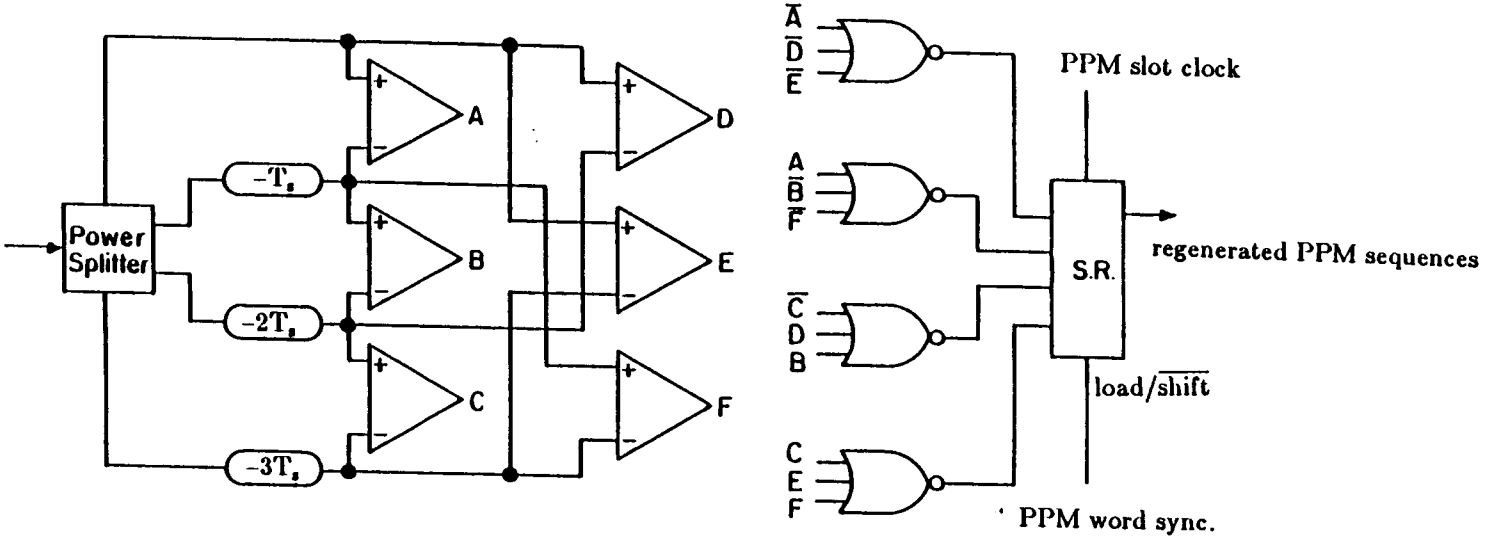

Figure 3.10. PPM signal detection circuit.

corresponded to the APD output photocurrent integrated over each time slot. Six high speed comparators were used to compare every two samples. The slot that contained the largest energy was determined from the comparator outputs through the use of the four NOR gates shown in Figure 3.10. The resultant PPM word pattern was loaded into a shift register at the end of each PPM word and shifted out serially afterwards. The sampling of the matched filter output was done by controlling the time at which the shift register of Figure 3.10 was loaded. The sampling could also be done by sampling the all six comparator outputs before the shift register was loaded. Experiments showed the two method gave the same receiver performance. The comparators in Figure 3.10 were Motorola MC1650 one bit A/D converters. The time delay between the detection of the received noisy PPM signal and the appearance of the regenerated digital PPM sequence was one PPM word time, 80 ns.

3.3.4. The PPM Demodulator

Figure 3.11 shows a schematic diagram of the PPM demodulator. It worked as follows. The pulse positions of received PPM words were represented by the state of a two bit counter driven by the PPM slot clock. The counter was synchronous with the counter of the PPM modulator shown in Figure 3.4. The two binary bits corresponding to a received PPM word were decoded by loading the two bits of the counter output into a shift register upon the arrival of a PPM pulse. The two binary bits were then loaded to another shift register at the end of each PPM word and shifted out serially. Figure 3.12 shows a timing diagram of this circuit. The time delay between the received PPM word and the output binary bits was four PPM time slots, or 80ns. Therefore, the total delay from the input

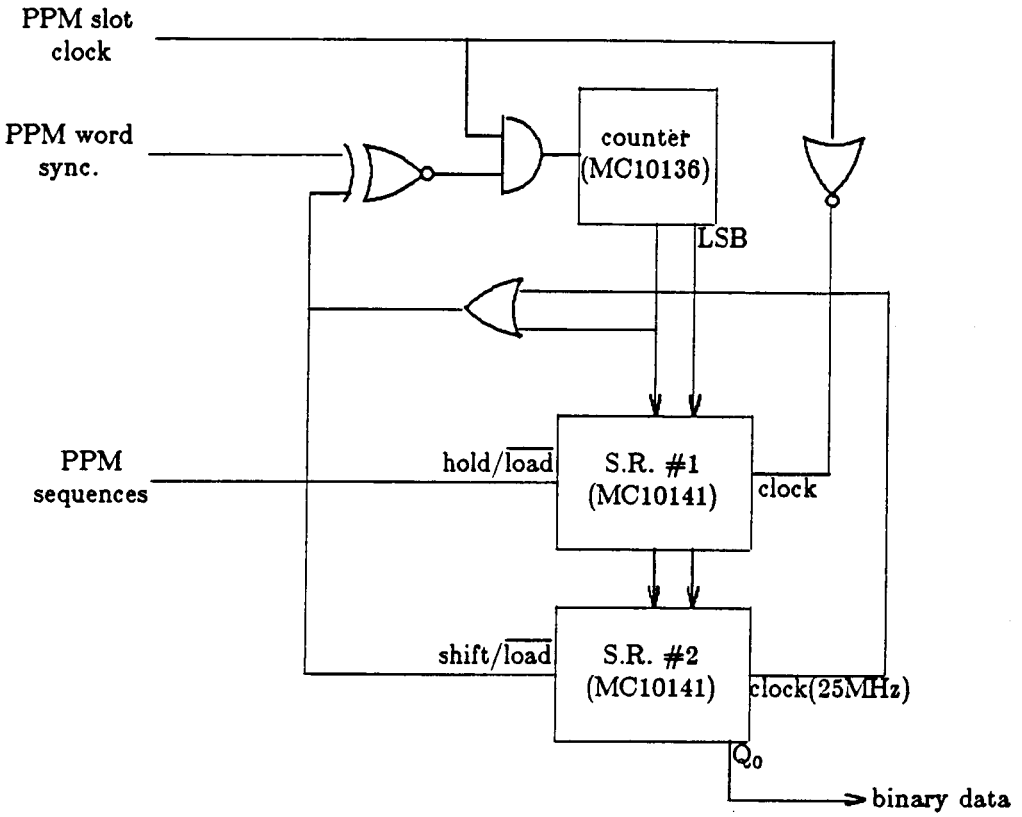

Figure 3.11. The PPM demodulator

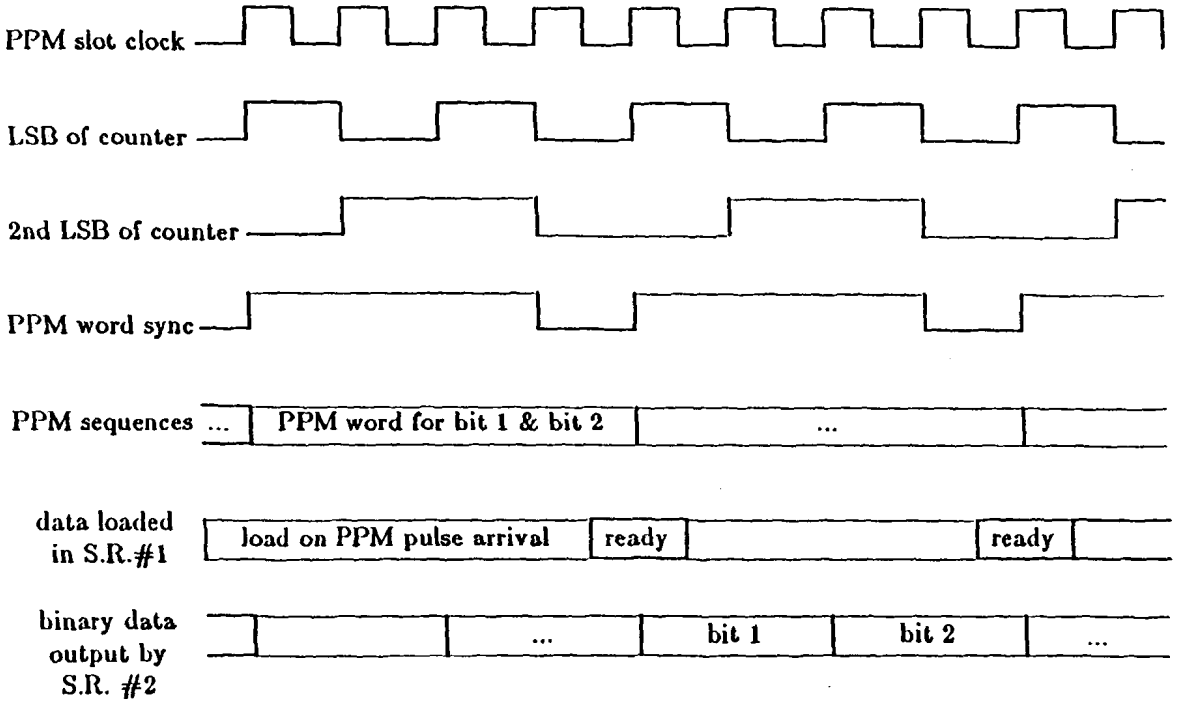

figure 3.12. Timing diagram of the PPM demodulator

source binary data to the received binary data was 12 time slots or 240 ns. This did not include delays caused by the optical propagation and the delays introduced by the diode driver, the amplifier, and the coax cables which were not part of the receiver.

The synchronization of the counter in Figure 3.11 was established as follows. The output of the OR gate in Figure 3.11 was used as the PPM word synchronization signal in the demodulator. A XNOR gate was used to compare this signal with the PPM word synchronization signal from the modulator in the transmitter. If the two signals disagreed, the outputs of the XNOR gate and the AND gate became "low", which blocked the clock that drove the counter. The counter state remained unchanged until its state coincided with that of the counter in the PPM modulator.

3.4. Measurements

Detailed descriptions about the procedures used to measure the receiver BER, the received optical signal levels, and other system parameters will be presented in this section. The measurement results will be compared with the theoretical results of Chapter 2.

3.4.1 Receiver BER vs. Detected Photons per Bit

The binary source data consisted of repetitions of a pseudo random sequence $2^{20}-1$ bits long. The received binary data sequences were directly compared with the properly delayed version of the source binary data sequences with the use of a XOR gate, as shown in Figure 3.13. The output of the XOR gate was sampled at the binary data clock rate through an AND gate to avoid miscounting consecutive bit errors. The AND gate output a short pulse every time there was a bit error between the received

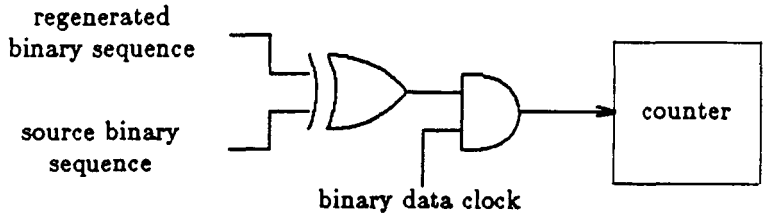

Figure 3.13. Measurement of receiver BER

binary data and the source binary data. A universal counter (Fluke 7250A) read out the number of bit errors per second or bit error frequency. The receiver BER was determined by dividing the bit error frequency by the data rate, 25×10^6 bits/second. The counter recorded at least 100 error events before an average bit error frequency was computed.

The signal levels received by the APD are expressed in terms of the average number of detected signal photons per transmitted information bit. This is given by the ratio of the number of detected photons per PPM pulse, $\overline{n}_s$, to the number of bits contained in a PPM word, $\log_2 Q$, i.e.,

$$\text{photons/bit} = \frac{\eta(P_1 - P_0)T_s}{hf \log_2 Q} \tag{3.4.1}$$

where η is the quantum efficiency of the APD, hf is the photon energy, and P_1, P_0 are the received optical power in Watts when a PPM pulse is present and absent, respectively.

Since the optical power meter used could only measure average power and not the peak power of the PPM pulses, P_1 was obtained by multiplying the average received optical power by the PPM alphabet size, Q=4, when the PPM signal was present. The average received optical power was measured by removing the APD and substituting the sensor of an optical power meter (UDT350 with UDT 260 sensor head). No other changes were made to the optics during the measurements. The APD was then repositioned and the receiver BER was again determined. The data were abandoned if the two average error frequencies had changed by more than 10%. This was done to avoid the effects of any drift in received optical power during the course of the measurements. The photosensitive area of the sensor head was much larger than that of the APD to ensure that all the light incident

on the APD was included in the measurement of the received optical power. On the other hand, the background radiation power received by the sensor head was much larger than that received by the APD which had a much smaller active area. Therefore, this background radiation power had to be subtracted from the readings of the optical power meter when measuring the average signal optical power received by the APD. The accuracy of the optical power meter was assured by comparing its readings with those given by other independently calibrated optical power meters.

The background radiation power actually received by the APD, P_0, was so small that it could not be directly measured with the optical power meter used to measure P_1. Alternatively, P_0 was determined by measuring the noise current output from the APD and using the relationship [32]

$$\frac{d<i_n^2>}{df} = 2e^2\frac{\eta P_0}{hf}G^2F \qquad (3.4.2)$$

Here $<i_n^2>$ is the variance of the noise current output from the preamplifier, and e is the electron charge. The RF noise power output from the preamplifier was measured with a RF power meter (HP-435B with 8282A sensor). The spectral density of the noise power was determined by dividing the total noise power by the bandwidth over which the noise power was measured. The spectral density of the noise current variance on the left hand side of (3.4.2) was determined by dividing the noise power spectral density by the square of the gain of the preamplifier. This method assumed the power spectral density of the noise was white, which was confirmed by direct measurement of the power spectrum of the APD output signal over the range dc to 100 MHz. The extinction ratio of the laser diode between ON and OFF states was assumed very high and its effect was ignored dur-

ing the measurements.

3.4.2. Measurements of Other System Parameters

The optimal average APD gain for a fixed received optical power level was determined by adjusting the APD reverse bias voltage until the receiver BER reached a minimum. The actual value of the APD gain was measured as follows. The APD preamplifier output signal was displayed on an oscilloscope, and the average value of the peak height of the output in time slots that contained the received light pulse was estimated by inspection. Since the gain of the preamplifier was g=28.9mV/μA and the received optical power, P_1, could be measured, the average APD gain was obtained by

$$G = \frac{V_p/g}{e\eta P_1/hf} \tag{3.4.3}$$

where V_p is the average peak amplitude of the APD response in volts. The measured APD gain was only approximate because of the way the peak amplitudes of the pulses was determined.

Amplifier thermal noise can be neglected compared with the APD excess noise when a strong cw background radiation is present. The excess noise factor, F, can be determined by measuring the noise current variance and using (3.4.2). The ionization ratio, k_{eff}, can be derived from (2.1.4) when the excess noise factor is known. Measurements made at several values of APD gain gave an average value of k_{eff} very close to 0.010. (0.0097 $\pm$ 0.0018).

The equivalent noise temperature of the preamplifier was obtained by measuring the noise power spectral density of the preamplifier when the APD bias voltage was reduced to nearly zero (G=0) so that only the amplifier thermal noise was present. The one sided noise power spectral

density, N, is related to the equivalent noise temperature, T_e, by

$$N = 4KT_e/R \quad A^2/Hz \,. \tag{3.4.4}$$

It was found that T_e=1100°K. The corresponding input rms noise current was 7.7pA/$\sqrt{Hz}$, somewhat larger than value given on the data sheet of the preamplifier of 4.4pA/$\sqrt{Hz}$. The extra noise was believed to come from the following amplifiers, cables, connectors, and etc..

The number of detected noise photons due to the APD bulk leakage current, I_b, is given by $\bar{n}_{bl}=I_bT_s/e$. The APD bulk leakage current was obtained from the data supplied by the manufacturer of the APD as follows. The spectral density of the noise current of the APD in the dark was given as $(d<i^2_{dark}>/df)^{-1/2}=3\times10^{-13}A/\sqrt{Hz}$ for G=600. The bulk leakage current was related to the noise current by $d<i^2_{dark}>/df=2e^2G^2FI_b$ [32]. It was found that I_d=0.0978pA or $\bar{n}_{bl}$=0.0122.

The total APD dark current, I_d, was 12 nA as given in the data sheet. Thus the APD surface leakage current was $I_s=I_d- GI_b$=11.9nA. The one sided noise spectral density due to this surface leakage current at the input of the preamplifier was $2eI_s=3.8\times10^{-27}A^2/Hz$. The noise spectral density of the preamplifier was $4KT_e/R=5.3\times10^{-23}A^2/Hz$. Therefore the APD surface leakage current had little effect on the measurements and system performance.

3.4.3. Results and Discussions

Figure 3.14 shows the results of numerical evaluations of the receiver BER, (2.6.6) and (2.3.8), as a function of the average APD gain for the received optical signal levels indicated in the graph. The curve with $\bar{n}_0$=12.5 corresponds to I_b=0.1nA and P_0=0. The curve with $\bar{n}_0$=0.0122

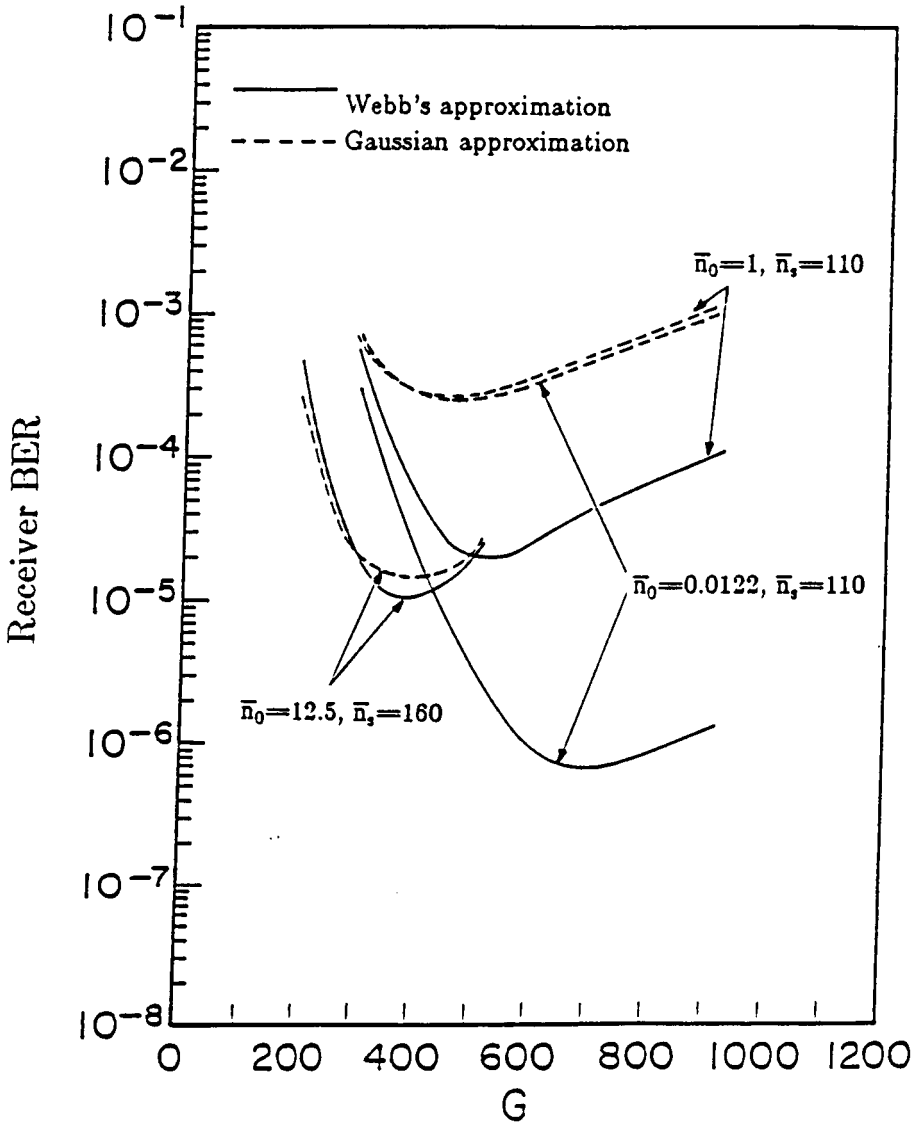

Figure 3.14. Receiver BER vs. average APD gain. The solid curve corresponds to the results of the Webb's approximation described in section 2.4. The dashed curve corresponds to the results of the Gaussian approximation described in section 2.3. Other parameters used were: APD ionization ratio k_{eff}=0.010. APD load resistance R=1030Ω. equivalent noise temperature of the preamplifier T_e=1100°K, APD surface leakage current I_s=11.9nA, and the PPM slot time T_s=20ns.

corresponds to our actual experimental conditions when no actual background light was present. The results based on the Gaussian approximation, (2.3.1) through (2.3.8) are also plotted (dashed curves) for the purpose of comparison. The measured optimal APD gain with $\bar{n}_0$=0.0122 was 700, which was in good agreement with the numerically computed results as shown in Figure 3.14. The Gaussian approximation works well for $\bar{n}_s$=12.5 but very poorly for $\bar{n}_0$=0.0122. The validity of equation (2.6.6) was further tested experimentally under the condition $\bar{n}_0$=1, which was set by arbitrarily introducing a background light source. The measured optimal APD gain in this case was 580, close to what the numerical evaluation had predicted, as shown in Figure 3.14.

Figures 3.15 through 3.17 are the numerical results of receiver BER as a function of the average number of detected photons per information bit, under $\bar{n}_0$=12.5, $\bar{n}_0$=1, and $\bar{n}_0$=0.0122, respectively. Figure 3.15 shows once again the appropriateness of Gaussian approximation under $\bar{n}_0$=12.5. The small crosses in Figure 3.16 and Figure 3.17 are the experimental results under each background noise level, and they are all very close to the numerical computation results based on equation (2.6.6) and (2.3.8). These results substantiate the validity of the numerical evaluation procedure described in the previous chapter using the Webb's approximation. The Gaussian approximation gives a very poor estimate for the optimal APD gain and the receiver BER under low background radiation level. At $\bar{n}_0$=0.0122 and $\bar{n}_s$=110, use of the Gaussian model underestimated the optimal APD gain by almost a factor of two and overestimated the bit error probability by more than two orders of magnitude over what was actually measured in the experiments. Figure 3.14 through Figure 3.17 also show that the

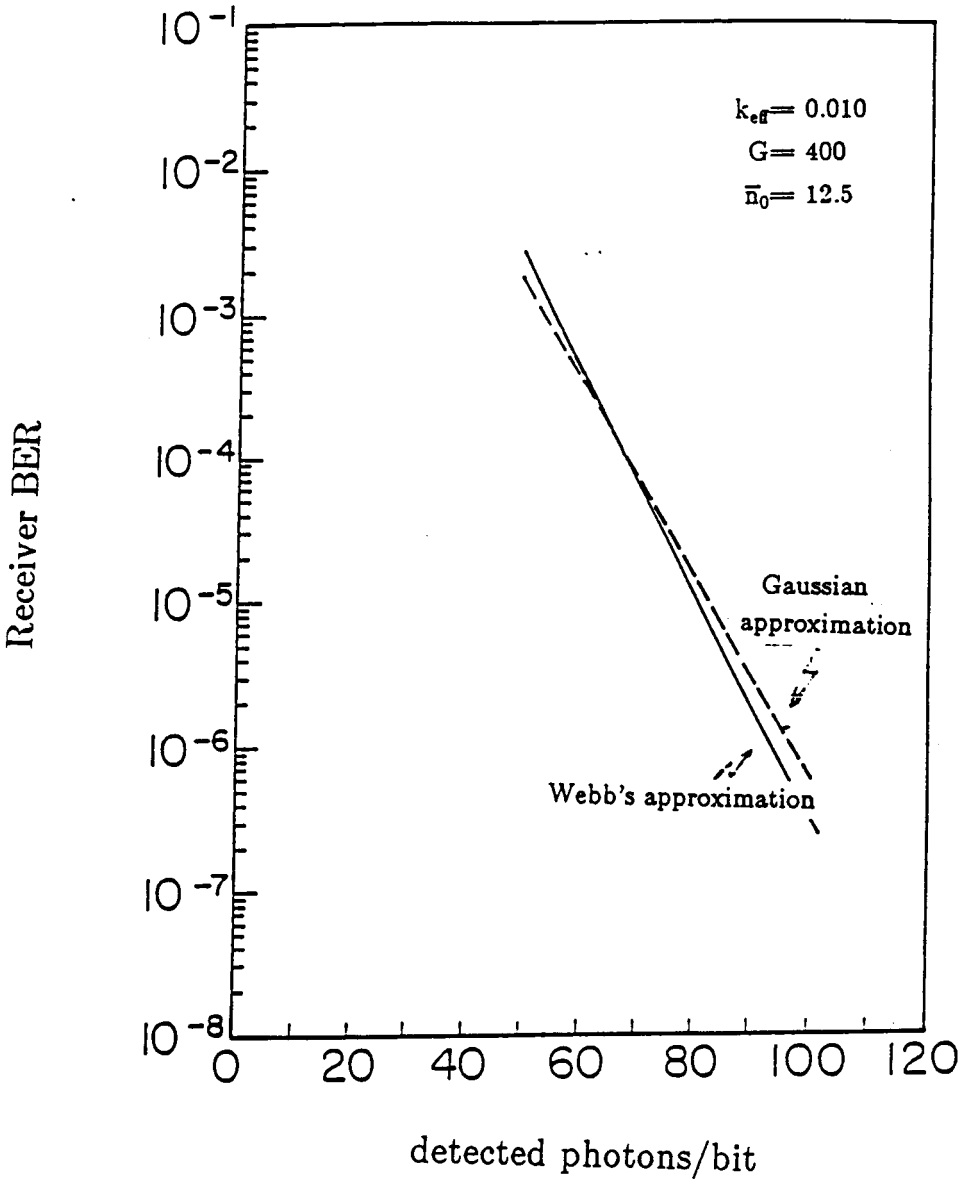

Figure 3.15. Receiver BER vs. average number of detected photons per information bit. The solid curve corresponds to the results of the Webb's approximation described in section 2.4. The dashed curve corresponds to the results of the Gaussian approximation described in section 2.3. The average APD gain used was G=400, the optimal value according to Figure 3.14. The background radiation level was $\bar{n}_0$=12.5. Other parameters used were the same as those in Figure 3.14.

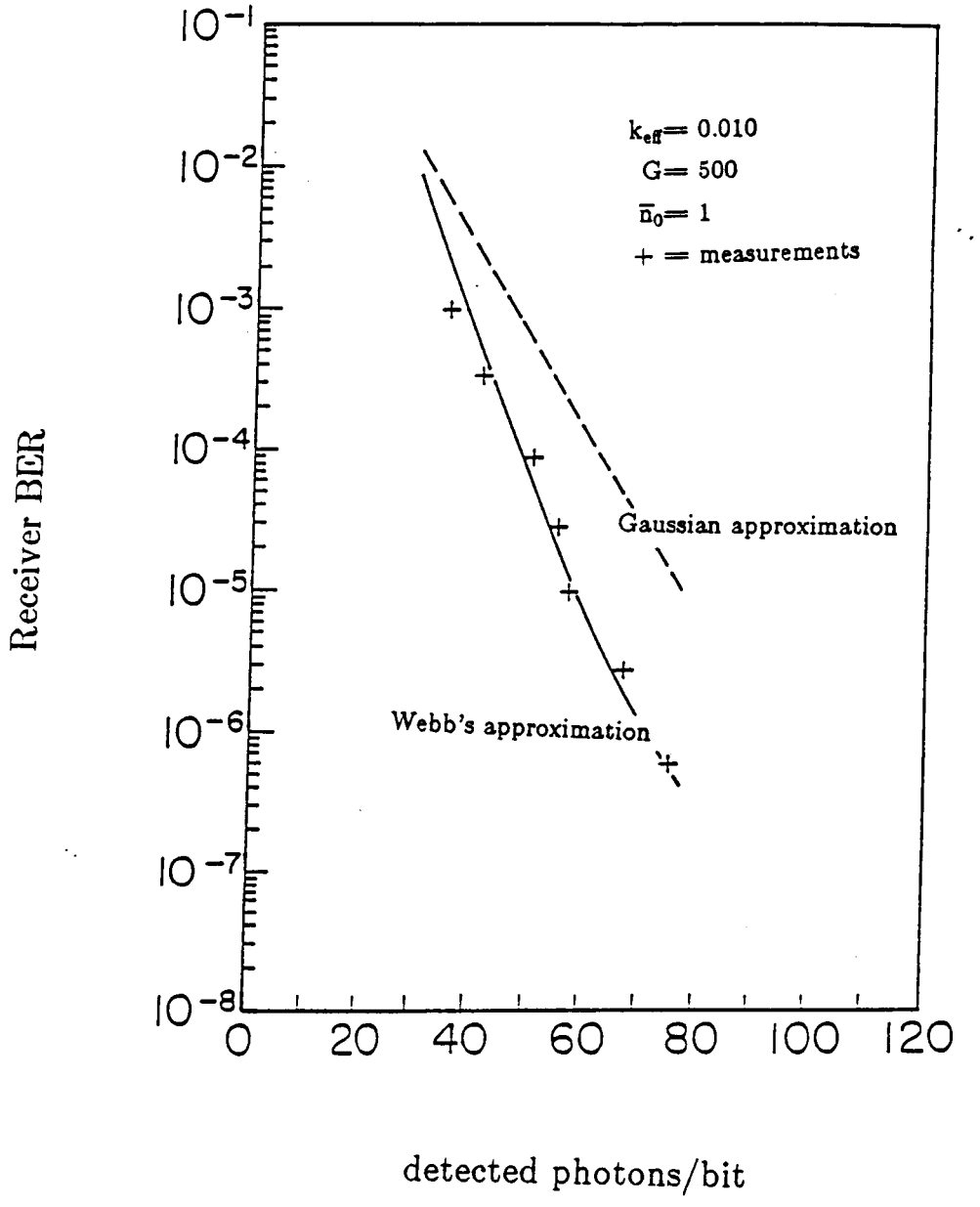

Figure 3.16. Same as Figure 3.15. but at a different background radiation level. $\bar{n}_0$= 1. The Gaussian approximation used G=450, and the Webb's approximation used G=500, which are the optimal values according to Figure 3.14. Other parameters used were the same as those in Figure 3.14.

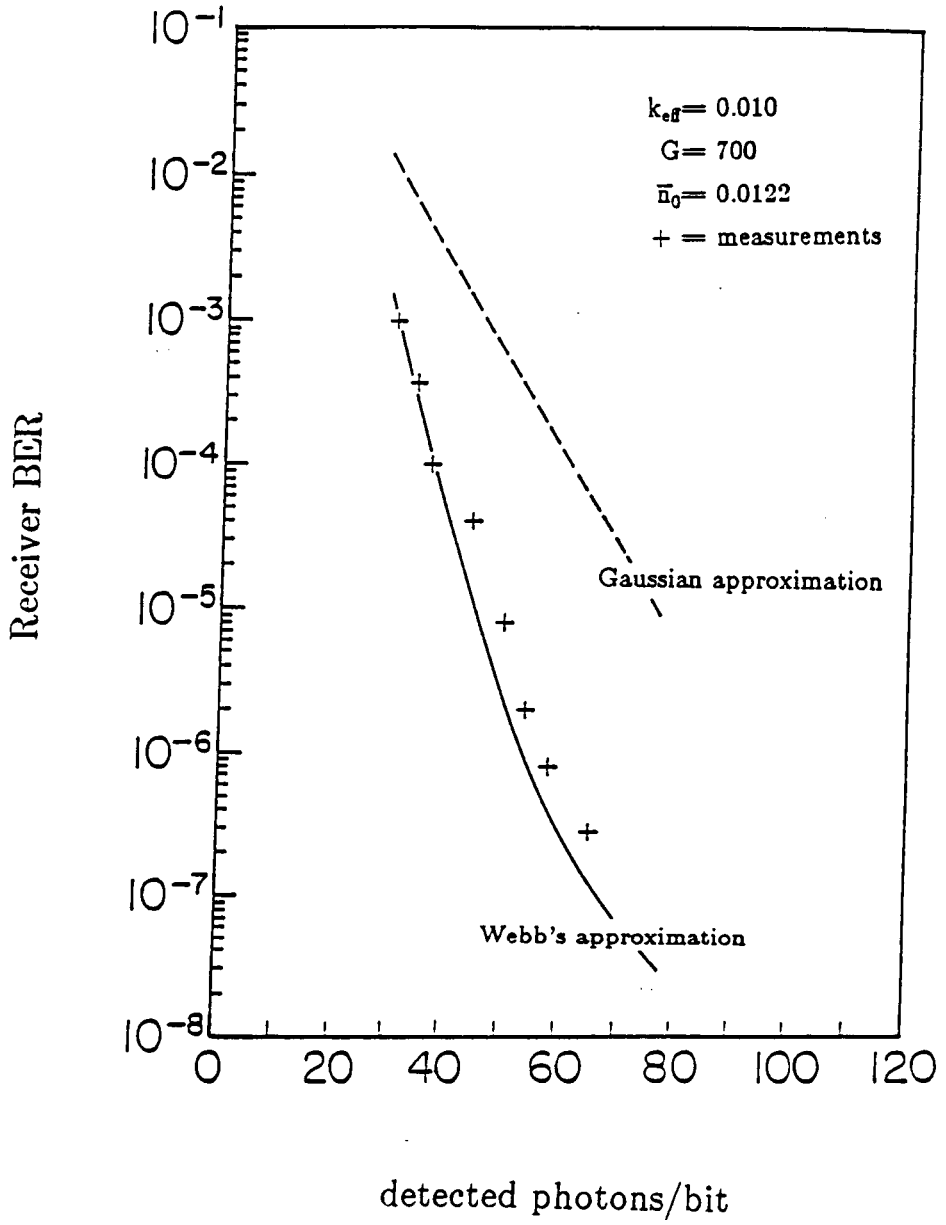

Figure 3.17. Same as Figure 3.15, but at a different background radiation level, $\bar{n}_0$= 0.0122. The Gaussian approximation used G=450, and the Webb's approximation used G=700, which are the optimal values according to Figure 3.14. Other parameters used were the same as those in Figure 3.14.

discrepancies between the results of the Gaussian approximation and the nearly exact Webb's approximation get bigger and bigger as the average number of background noise counts decreases. It may be concluded that Gaussian approximation should not be attempted when $\bar{n}_0 < 10$.

This system has achieved a BER of 10^{-6} at a received optical signal level corresponding to 55 average detected photons per information bit. The best performance reported so far for similar systems was 80 average detected photons per information bit under BER $\leq 10^{-6}$ [43, 25]. Therefore, the system described in this chapter has achieved the highest receiver sensitivity yet reported for direct detection optical communication systems that used semiconductor laser transmitters and APD photodetectors.

Chapter 4. PPM Slot Timing Recovery

It has been assumed in the previous two chapters that perfect synchronization between the transmitter and receiver was available. The establishment of such timing synchronization will be the major topic of the rest of this dissertation. PPM slot synchronization and word synchronization will be addressed in this chapter and the next, respectively.

4.1. Introduction

One of the basic problems in a communication system that uses PPM signaling is to establish timing synchronization between the transmitter and the receiver. As mentioned in Chapter 1, the optimal receiver for a direct detection PPM optical communication system consists of a device which integrates the APD output current over each time slot and compares the Q integrated outputs to find the largest. As a result, the receiver requires both PPM slot timing recovery and PPM word timing recovery. Any offset or jitter in the recovered time slot boundaries directly affects the results of the integrations of the APD output over the time slots. Any part of the signal energy that spills over into the adjacent time slot acts as background noise and the performance of the entire system is degraded. Incorrect PPM word boundaries will cause the receiver to compare the integrated APD outputs from time slots that do not belong to the same PPM word. Furthermore, PPM word timing errors will paralyze the PPM demodulator and cause catastrophic errors in the demodulated binary data sequences.

In practice, slot timing synchronization requires a regenerated clock waveform at the receiver at the slot clock frequency which is synchronized with the clock at the transmitter. Once the correct slot timing is provided,

PPM word synchronization can be established by a properly initialized modulo-Q counter driven by the regenerated slot clock. Details about PPM word timing recovery will be given in Chapter 5. This chapter addresses only the issues of slot clock synchronization for receivers that use APD photodetectors.

Generally speaking, all the technologies for bit timing extraction in conventional microwave telecommunication systems can be used for slot timing recovery in optical PPM communication systems. Modification is necessary, however, to cope with the shot noise of photodetectors that appears with the additive Gaussian noise of subsequent amplifiers. The use of APD's improves detector sensitivity significantly but also introduces so-called excess noise, which is nonadditive and follows the Conradi distribution [14, 15]. Several conventional means of timing recovery have been studied for use in optical communications [44, 45, 46, 18, 19, 47] and some of them are widely used in optical fiber telecommunication systems [48]. Free space optical communication systems, however, are characterized by transmission channels which have very high losses but can be considered as dispersion free. For example, the losses under diffraction limited operation between two geosynchronous satellites 120° apart (73,000 km) is about 66dB if 20 cm diameter telescopes are used as the transmitter and receiver antennas. Optical fiber communication systems, on the other hand, are dispersion limited rather than propagation loss limited. The received signal levels are usually much higher than those of free space optical communication systems. Furthermore, timing recovery in PPM systems is different than in the case of OOK signal format which are widely used in optical fiber systems. PPM signaling has a fixed duty cycle or pulse rate regardless

of the data transmitted.

This chapter is organized as follows. The next section gives a brief review of previous studies of slot clock timing recovery for direct detection optical communication systems. Section 4.3 discusses transition detector type clock recovery schemes, which are widely used in conventional digital communication systems but have not yet been studied for optical communication systems. A theoretical analysis associated with this system is also developed. Section 4.4 discusses the effects of slot timing jitter on system performance. Section 4.5 describes the experiments and measured performance of this slot timing recovery system.

4.2. Review of Slot Clock Timing Recovery in Direct Detection Optical Communication Systems

The response of an APD to an incident optical field can be modeled as a filtered compound doubly stochastic Poisson process [5] if there is no amplifier thermal noise. The basic problem of timing recovery is to estimate slot clock waveforms from the times at which photons are detected from the received optical pulse train. One optimal procedure is to use maximum likelihood (ML) estimation. Under the assumptions that the APD has an unlimited frequency response, the APD output can be modeled as a compound Poisson random point process with intensity function, $\lambda(t)$, which is proportional to the intensity of the received optical field. The likelihood function to be maximized can then be expressed as [5]

$$p[\{N_\sigma;\, t_1 \le \sigma < t_2\} \mid \lambda(t)] = \exp\left\{ -\int_{t_1}^{t_2} \lambda(\sigma)d\sigma + \sum_{i=1}^{N_{t_1,t_2}} \ln[\lambda(\sigma_i)] + \sum_{i=1}^{N_{t_1,t_2}} \ln[P(m_i)] \right\} \qquad (4.2.1)$$

where $p[\{N_\sigma;\, t_1 \le \sigma < t_2\} \mid \lambda(t)]$ is the sample function density for the

occurrence times, the σ_i's, of the photon absorptions, and N_{t_1,t_2} is the total number of photon absorptions within the interval $[t_1,t_2]$. The number of secondary photoelectrons generated in the avalanche region of the APD in response to each photon absorption is denoted as m_i, the probability, $P(m_i)$, is given in [49] and does not explicitly contain the σ_i.

If the data pattern is known, i.e. the shape of $\lambda(t)$ is known except for the time origin, the maximization procedure requires finding the time origin and the set of subsequent pulse boundaries within $[t_1,t_2]$ which maximize (4.2.1). If the slot period is known, the only parameter to be estimated is the time origin. When the data pattern is not known, the likelihood function is obtained by averaging (4.2.1) over all possible data patterns. Such ML estimation schemes usually require too many computation steps to be carried out in real time. Georghiades [20] derived an approximate likelihood function that reduced the amount of computation significantly and yet gave almost as good synchronization performance as that of the exact likelihood function under the conditions of high signal to noise ratio. A digital computer is still necessary, however, to store the photon absorption times, evaluate the approximate likelihood functions for different time slot boundary shifts, and to then find the maximum through comparisons. In situations where the bandwidth of the APD is limited and the data rate is high, the amplified APD output current cannot be modeled as a point Poisson process, and therefore, the ML synchronization methods described above have to be modified accordingly.

In conventional digital communication systems, a commonly used ML synchronization scheme uses an analog device to compute the derivative of the likelihood function. The result is used to derive an error signal to

correct the frequency of the clock oscillator at the receiver. When the data pattern is unknown, an estimated data pattern based on a previously estimated timing base may be used to compute the derivative of the likelihood function. This is referred to as data-added or decision-directed synchronization [50, 51]. The same method was studied for use in optical communication systems by Gagliardi [9]. It was shown that the computation becomes reasonably simple only for a few special pulse shapes, for example, pulses of flat top and exponential rise and fall edges. Rectangular shapes, which are optimal for peak power limited optical transmitters, such as semiconductor laser diodes, are not appropriate for this kind of ML estimation scheme.

A popular variant of ML estimation for rectangular pulses is the early-late gate scheme [52] though it is not mathematically optimal. The early gate integrates the received signal over the first half of the time slot interval and the late gate integrates the signal over the second half of the interval, based on previously estimated time slot boundaries. If the system is perfectly synchronized, the two values of the integrations will be exactly equal on average. Therefore, the difference of the two integrations can be used to derive an error signal to adjust the frequency of the slot clock oscillator. A detailed study of early-late gate synchronization in an optical communication context has been given by Gagliardi [9].

A phase lock loop (PLL) can be used to regenerate the slot clock at the receiver. Since PPM signals with non return-to-zero (NRZ) rectangular pulse shapes do not contain a frequency component at the slot clock fundamental frequency [53], some nonlinearity must be introduced to generate the desired frequency component. Several possible nonlinearities have been

studied, among them are square law, absolute value, ln(cosh) and fourth power [18, 47]. The PLL may be replaced by a much simpler narrowband filter. The disadvantage is the resultant static phase error when the input slot clock frequency shifts due to Doppler effects or slow frequency drifts of the clock oscillator in the transmitter. The static phase error resultant from a PLL with an active loop filter is usually negligible. The static phase error resultant from a narrowband filter is given by $\Delta\phi \approx \tan^{-1}(2Q_f\Delta f/f_0)$, where Q_f is the quality factor of the narrowband filter, Δf is the frequency shift, and f_0 is the center frequency of the filter. Since the quality factor of the narrowband filter is usually high in order to reduce the jitter of the output slot clock, a small frequency shift of the input slot clock may cause a significant static phase error in the output. Andreucci and Mengali [44] have studied timing recovery schemes that use narrowband filters for return-to-zero (RZ) data.

Another class of timing recovery schemes, popular in conventional digital communication systems, are called transition detectors [52]. They generate unipolar output pulses at positive or/and negative going transitions of the input pulses. The power spectrum of the resulting unipolar pulse sequence contains a discrete frequency component at the slot clock fundamental frequency, which can then be tracked by a PLL or a narrowband filter. This method was used in our system and is demonstrated to be a simple, and yet very effective means of establishing receiver slot clock synchronization.

4.3. Slot Clock Recovery with a Transition Detector

4.3.1. Transition Type Slot Clock Recovery System

The shot noise of an APD is signal dependent. Unlike the noise in conventional communication systems, it is neither a stationary nor a Gaussian random process. The mean and the variance of the APD output current, $i_A(t)$, is given by [32]

$$E\{i_A(t)\} = G \int_{-\infty}^{\infty} [\frac{e\eta P_o(\tau)}{hf} + I_d] h_A(t-\tau)\, d\tau \qquad (4.3.1)$$

$$var\{i_A(t)\} = eG^2F \int_{-\infty}^{\infty} [\frac{e\eta P_o(\tau)}{hf} + I_d] h_A^2(t-\tau)\, d\tau \qquad (4.3.2)$$

where $P_o(t)$ is the incident optical power in Watts, I_d is the total APD dark current, and $h_A(t)$ is the causal response of the APD to a single photon absorption. Other parameters in the above equations are defined the same as in Chapter 2. The APD output current has to be further amplified and the amplifier noise, which is stationary and Gaussian, has to be added to the total noise. As shown in (4.3.1) and (4.3.2), both the signal and the noise output from the APD increase with the average APD gain. The amplifier thermal noise, on the other hand, is independent of the APD gain. Therefore, there exists an optimal value for the average APD gain under which the overall receiver performance including the timing recovery is optimized. Since the timing error in the recovered clock can always be reduced by using a smaller loop bandwidth for the PLL, the average APD gain may simply be optimized such that the receiver BER is a minimum, assuming perfect slot timing recovery is available. Under such an optimal APD gain, the APD shot noise is usually the major contribution to the total noise [54]. The amplified APD output signal contains mostly amplitude noise due to the multiplicative nature of the APD shot noise. The transition detector, by intuition, is the least affected by amplitude

fluctuations of all the commonly used nonlinearities that can be employed to introduce the desired frequency component at the slot clock fundamental frequency in the received PPM waveform. Consequently, it was used rather than one of the other methods in our system.

Figure 4.1 is a block diagram of the transition detector type slot clock recovery circuit. The input to this circuit is the amplified APD output which consists of rectangular pulses of width T_s corrupted by signal dependent shot noise and lesser amounts of additive Gaussian noise. The lowpass filter accounts for the limited bandwidth of the APD and the following amplifiers. The comparator acts as a threshold crossing detector which outputs a clean but jittered pulse to the pulse shaper in response to a received light pulse. The output of the pulse shaper is a rectangular pulse of width $T_s/2$ with its rising edge lined up with that of the input pulse. This choice of pulsewidth maximizes the amplitude of the fundamental frequency component at the slot clock frequency [52]. The pulse shaper has a "dead time" so that it cannot be triggered more than once within one time slot.

4.3.2. Phase Errors of the Recovered Slot Clock

The theory of PLL tracking systems has been well developed for conventional communication systems and several studies have been done on optical communication systems as well. It has been shown that for a sufficiently narrow loop bandwidth, the phase error of the regenerated clock waveform has variance given approximately by [18]

$$\sigma_\phi^2 \approx \frac{2B_L N(\omega_s)}{P_s} \qquad (4.3.3))$$

Here $N(\omega)$ is the two sided noise power spectrum, ω_s is the angular frequency of the locked PLL, P_s is the power of the sinusoidal component of

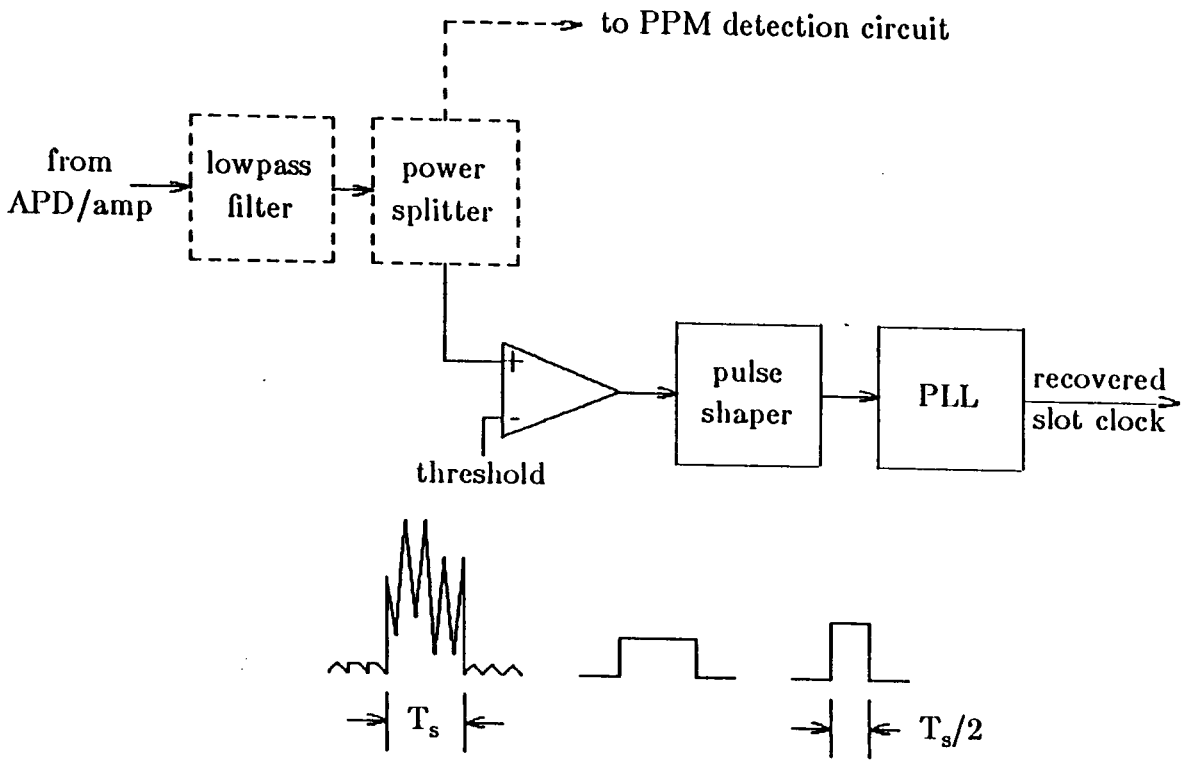

Figure 4.1. Block diagram of the slot clock recovery circuit. The dashed blocks are the same as those in Figure 3.7.

the input signal at the lock frequency, and B_L is the loop bandwidth given by

$$B_L = \int_0^\infty | H_{PLL}(2\pi f) |^2 df, \qquad (4.3.4))$$

where $H_{PLL}(2\pi f)$ is the transfer function of the linearized model of the PLL given in [52].

The phase error of the recovered slot clock obtained with a narrowband filter can also be approximated by (4.3.3) with the effective loop bandwidth B_L given by [52]

$$B_L = \int_{f_0}^\infty | H_{nbf}[2\pi(f - f_0)] |^2 df, \qquad (4.3.5)$$

where $H_{nbf}(2\pi f)$ is the system function of the filter, and f_0 is the center frequency.

Both the signal power and noise spectral density used in (4.3.3) can be obtained from the power spectrum of the signal at the input of the PLL. Since the received noisy PPM signal is not a stationary random process, the power spectrum at the input of the PLL cannot be obtained by taking the Fourier transform of its autocorrelation function. The alternative is to use the definition given in [53]

$$S(\omega) = \lim_{T\to\infty} \frac{1}{2T} E\{ | X_T(\omega) |^2 \} \qquad (4.3.6)$$

where $X_T(\omega)$ is the Fourier transform of a sample of the signal waveform from -T to T given by

$$X_T(\omega) = \int_{-T}^{T} x(t) e^{-j\omega t} dt \qquad (4.3.7)$$

As in Chen's approach in [18], the input signal to the PLL is defined as

$$x(t) = \sum_n p(t - nQT_s - c_n T_s - \tau_n) \qquad (4.3.8)$$

where p(t) represents the rectangular pulse shape, T_s is the duration of a PPM time slot, c_n is an integer from 0 to (Q-1) used to indicate the random PPM pulse position, and τ_n represents random jitter in threshold crossing times. If all transmitted data are equally likely, the $\{c_n\}$ form a set of independent, identically distributed (i.i.d) random variables. The $\{\tau_n\}$ can also be considered to be i.i.d. random variables. A derivation of the power spectrum under these assumptions is given in the next subsection.

4.3.3. Power Spectrum of the Input to the PLL

Substitute (4.3.8) into (4.3.7) and let $T=NQT_s$ with N an integer,

$$X_T(\omega) = \sum_{n=-N}^{N} P(\omega) e^{-j\omega(nQT_s + c_n T_s + \tau_n)}. \tag{4.3.9}$$

Since the c_n's and the τ_n's are two independent sets of i.i.d. random variables,

$$\begin{aligned} E\{ | X_T(\omega) |^2 \} &= | P(\omega) |^2 \sum_{m,n=-N}^{N} e^{j\omega QT_s(m-n)} E\{e^{j\omega T_s(c_m - c_n)}\} E\{e^{j\omega(\tau_m - \tau_n)}\} \\ &= | P(\omega) |^2 [(2N+1) + \\ &\qquad + | E\{e^{j\omega T_s c_n}\} |^2 | E\{e^{j\omega \tau_n}\} |^2 \sum_{m \neq n} e^{j\omega QT_s(m-n)}] \\ &= | P(\omega) |^2 [(2N+1) (1 - | C(\omega) |^2 | M_\tau(\omega) |^2) \\ &\qquad + | C(\omega) |^2 | M_\tau(\omega) |^2 | \sum_{n=-N}^{N} e^{-j\omega QT_s n} |^2], \end{aligned} \tag{4.3.10}$$

where $P(\omega)$ is the Fourier transform of the pulse shape p(t), $C(\omega)$ and $M_\tau(\omega)$ are the characteristic functions of the c_n and τ_n, respectively. These are given by

$$C(\omega) \equiv E\{e^{j\omega T_s c_n}\} = \frac{1}{Q} \sum_{n=0}^{Q-1} e^{j\omega T_s n} \tag{4.3.11}$$

and

$$M_\tau(\omega) \equiv E\{e^{j\omega\tau_n}\}. \tag{4.3.12}$$

The power spectrum (4.3.6) can be obtained by taking the limit of (4.3.10) as $T\to\infty$, therefore,

$$S(\omega) = |P(\omega)|^2\left[\frac{1}{QT_s}(1-|C(\omega)|^2|M_\tau(\omega)|^2) + |C(\omega)|^2|M_\tau(\omega)|^2 \lim_{T\to\infty}\frac{1}{2T}\left|\sum_{n=-N}^{N} e^{-j\omega QT_s n}\right|^2\right]. \tag{4.3.13}$$

Since $\sum_{n=-\infty}^{\infty} e^{-jxn} = 2\pi\sum_{k=-\infty}^{\infty}\delta(x-2\pi k)$, and $\delta(ax)=\frac{1}{|a|}\delta(x)$,

$$\lim_{T\to\infty}\frac{1}{2T}\left|\sum_{n=-N}^{N} e^{-j\omega QT_s n}\right|^2 = \lim_{T\to\infty}\frac{1}{2T}\left[\frac{2\pi}{QT_s}\sum_{n=-\infty}^{\infty}\delta(\omega-2\pi n/QT_s)\right]^2$$
$$= \frac{4\pi^2}{(QT_s)^2}\sum_{n=-\infty}^{\infty}\lim_{T\to\infty}\frac{1}{2T}\delta^2(\omega-2\pi n/QT_s). \tag{4.3.14}$$

Using the relationship that

$$\delta(\omega)=\frac{1}{2\pi}\lim_{T\to\infty} 2T\frac{\sin(\omega T)}{\omega T} \tag{4.3.15}$$

each term in the sum of (4.3.14) reduces to

$$\lim_{T\to\infty}\frac{1}{2T}\delta^2(\omega-2\pi n/QT_s)= \lim_{T\to\infty}\frac{1}{2T}\cdot\frac{1}{2\pi}2T\frac{\sin(\omega-2\pi n/QT_s)T}{(\omega-2\pi n/QT_s)T}\cdot\delta(\omega-2\pi n/QT_s)$$
$$= \frac{1}{2\pi}\delta(\omega-2\pi n/QT_s). \tag{4.3.16}$$

According to (4.3.11),

$$|C(\omega)| = \frac{1}{Q}\left|\frac{1-e^{j\omega T_s Q}}{1-e^{j\omega T_s}}\right| = \frac{1}{Q}\left|\frac{\sin(\omega T_s Q/2)}{\sin(\omega T_s/2)}\right|, \tag{4.3.17}$$

therefore, $|C(2\pi n/QT_s)|=1$ if $n=kQ$ for any integer k, and $|C(2\pi n/QT_s)|=0$ otherwise. Substituting (4.3.14), (4.3.16), and (4.3.17) into (4.3.13), the power spectrum of PPM signal becomes

$$S(\omega) = |P(\omega)|^2\left[\frac{1}{QT_s}(1-|C(\omega)|^2|M_\tau(\omega)|^2) + \frac{2\pi}{(QT_s)^2}|M_\tau(\omega)|^2\sum_{k=-\infty}^{\infty}\delta(\omega-2\pi k/T_s)\right]. \tag{4.3.18}$$

The first term in (4.3.18) corresponds to noise and the second term corresponds to the discrete frequency components at the slot clock fundamental frequency and its harmonics. Therefore, the noise power spectrum can be written as

$$N(\omega) = \frac{1}{QT_s} \mid P(\omega) \mid^2 (1 - \mid C(\omega) \mid^2 \mid M_r(\omega) \mid^2). \qquad (4.3.19)$$

The total power at the slot clock fundamental frequency is given by

$$P_s = \frac{2}{(QT_s)^2} \mid M_r(\omega_s) \mid^2 \mid P(\omega_s) \mid^2. \qquad (4.3.20)$$

4.3.4. Characteristic Function of the Threshold Crossing Time

If the random jitter at the threshold crossing time, the τ_n's, can be considered as i.i.d. zero mean Gaussian random variables, then

$$M_r(\omega) = e^{-\frac{1}{2}\sigma_r^2\omega^2} \qquad (4.3.21)$$

where σ_r^2 represents the variance of the threshold crossing times which will be determined next.

The input signal to the threshold crossing detector consists of the APD output current, $i_A(t)$, and amplifier thermal noise, $n_a(t)$. The threshold crossing time, t_c, is the solution to the equation $i_A(t_c) + n_a(t_c) = I_{th}$, where I_{th} represents the threshold level. The APD output current can be expressed as the sum of the signal and shot noise, as

$$i_A(t) = s(t) + n_s(t) \qquad (4.3.22)$$

where $s(t) = E\{i_A(t)\}$ and $n_s(t) = i_A(t) - E\{i_A(t)\}$. At high input optical signal levels, the threshold crossing time, t_c, varies within a small region about its mean value $T_c = E\{t_c\}$. Consequently, it is appropriate to approximate s(t) by the first two terms of its Taylor expansion about T_c, and write

$$I_{th} \approx s(T_c) + s'(T_c)(t_c - T_c) + n_s(t_c) + n_a(t_c). \tag{4.3.23}$$

Since $n_s(t)$ and $n_a(t)$ are independent and $s(T_c)=I_{th}$, it follows that

$$[s'(T_c)]^2\sigma_r^2 = E\{n_s^2(t_c)\} + E\{n_a^2(t_c)\}. \tag{4.3.24}$$

The variance of the amplifier noise is given as in Chapter 2,

$$E\{n_a^2(t_c)\} = \frac{4KT_eB}{R} \tag{4.3.25}$$

where K is Boltzmann's constant, T_e is the amplifier equivalent noise temperature, B is the bandwidth of the lowpass filter, and R is the load resistance seen by the APD.

The variance of the shot noise, $E\{n_s^2(t_c)\}$, is equal to the variance of the APD output current, which is a function of t_c. Conditioned on t_c, the APD output current is a filtered compound Poisson process with variance given by [5]

$$E\{n_s^2(t_c) \mid t_c\} = e^2G^2F \int_{-\infty}^{t_c} \lambda(t)h^2(t_c - t)dt. \tag{4.3.26}$$

where h(t) is the impulse response of the lowpass filter and $\lambda(t)$ is the photon counting intensity function. As far as threshold crossing time is concerned, one may assume

$$\lambda(t) = \begin{cases} \lambda_1 & t \geq t_0 \\ \lambda_0 & t < t_0 \end{cases} \tag{4.3.27}$$

where t_0 is the pulse transition time prior to t_c. If the laser has a high on-off extinction ratio and the background radiation appears to be small, i.e. $\lambda_1 >> \lambda_0$,

$$\begin{aligned} E\{n_s^2(t_c) \mid t_c\} &\approx e^2FG^2\lambda_1 \int_{t_0}^{t_c} h^2(t_c - t)dt \\ &= e^2FG^2\lambda_1 \left[\int_0^{T_c - t_0} h^2(u)du + \int_{T_c - t_0}^{t_c - t_0} h^2(u)du \right]. \end{aligned} \tag{4.3.28}$$

Since $t_c - T_c$ is very small, the integrand of the second term in (4.3.28) can be approximated by

$$h^2(u) \approx h^2(T_c - t_0) + 2h(T_c - t_0)h'(T_c - t_0)[u - (T_c - t_0)]. \quad (4.3.29)$$

Averaging both sides of (4.3.28) over t_c,

$$E\{n_s^2(t_c)\} \approx e^2 F G^2 \lambda_1 \left[\int_0^{T_c - t_0} h^2(u)du + h(T_c - t_0)h'(T_c - t_0)\cdot\sigma_r^2 \right]. \quad (4.3.30)$$

Next, according to [5],

$$s(t) = E\{i_A(t)\} = eG \int_{-\infty}^{t} \lambda(u)h(t-u)du \quad (4.3.31)$$

then

$$s'(t) \approx eG\lambda_1 h(t - t_0) \quad (4.3.32)$$

where $\lambda_1 >> \lambda_0$ is assumed. Substituting (4.3.25), (4.3.30) and (4.3.32) into (4.3.24), the variance σ_r^2 can be solved as

$$\sigma_r^2 = \frac{FG^2\lambda_1 \int_0^{T_c - t_0} h^2(u)du + \dfrac{4KT_eB}{Re^2}}{[G\lambda_1 h(T_c - t_0)]^2 - FG^2\lambda_1 h(T_c - t_0)h'(T_c - t_0)}. \quad (4.3.33)$$

Equation (4.3.33) may be evaluated by assuming that the lowpass filter is ideal and has a "brick wall" like frequency response, i.e.

$$H(j2\pi f) = \begin{cases} e^{-j2\pi f t_d} & |f| \leq B \\ 0 & \text{otherwise,} \end{cases} \quad (4.3.34)$$

or

$$h(t) = 2B \cdot \frac{\sin 2\pi B(t - t_d)}{2\pi B(t - t_d)} \quad (4.3.35)$$

where t_d is the time delay of the filter.

4.3.5. Average Threshold Crossing Time

There is an optimal value for the average threshold crossing time T_c, at

which (4.3.33) is minimized. In practice, it corresponds to an optimal threshold level applied to the threshold crossing detector. Figure 4.2 is a plot of the normalized rms threshold crossing time jitter, σ_τ/T_s, as a function of normalized threshold crossing time, $\Delta T_c B$, where $\Delta T_c = T_c-(t_0+t_d)$. In other words, ΔT_c is denoted as the time difference between the mean threshold crossing time, T_c, and the midpoint of the rising edge of the input pulse, t_0+t_d. The curve in Figure 4.2 is fairly flat near $B\Delta T_c = -0.1$. In fact, σ_τ/T_s increases by only 3% when $B\Delta T_c$ changes from its optimal value ($\approx$–0.08) to zero. Consequently, the value $B\Delta T_c=0$ can be used in (4.3.33) to a good approximation. This corresponds to a threshold level at one half the peak amplitude of the APD output pulses.

The impulse response of the low pass filter (4.3.35) and its derivative at time $t=T_c-t_0$ can be rewritten by substituting the new variable $\Delta T_c \equiv T_c-(t_0+t_d)$, as,

$$h(T_c-t_0) = 2B\frac{\sin 2\pi B\Delta T_c}{2\pi B\Delta T_c} \tag{4.3.36}$$

$$\frac{d}{dt}h(T_c-t_0) = 2B\frac{2\pi B\Delta T_c\cos 2\pi B\Delta T_c - \sin 2\pi B\Delta T_c}{2\pi B\Delta T_c^2}. \tag{4.3.37}$$

Furthermore,

$$\int_0^{T_c-t_0} h^2(u)du = \int_{-t_d}^{T_c-t_0-t_d} h^2(v+t_d)dv \approx \int_{-\infty}^{\Delta T_c} (2B\frac{\sin 2\pi Bv}{2\pi Bv})^2 dv$$

$$= B + \frac{2B}{\pi}\int_0^{2\pi B\Delta T_c} (\frac{\sin x}{x})^2 dx, \tag{4.3.38}$$

where the relationship $\int_{-\infty}^{0} (\frac{\sin x}{x})^2 dx = \frac{\pi}{2}$ has been used. When $B\Delta T_c \to 0$, equation (4.3.36), (4.3.37), and (4.3.38) reduce to $h(T_c-t_0) = 2B$, $\frac{d}{dt}h(T_c-t_0) = 0$, and $\int_0^{T_c-t_0} h^2(u)du = B$. Substituting these into (4.3.33), the

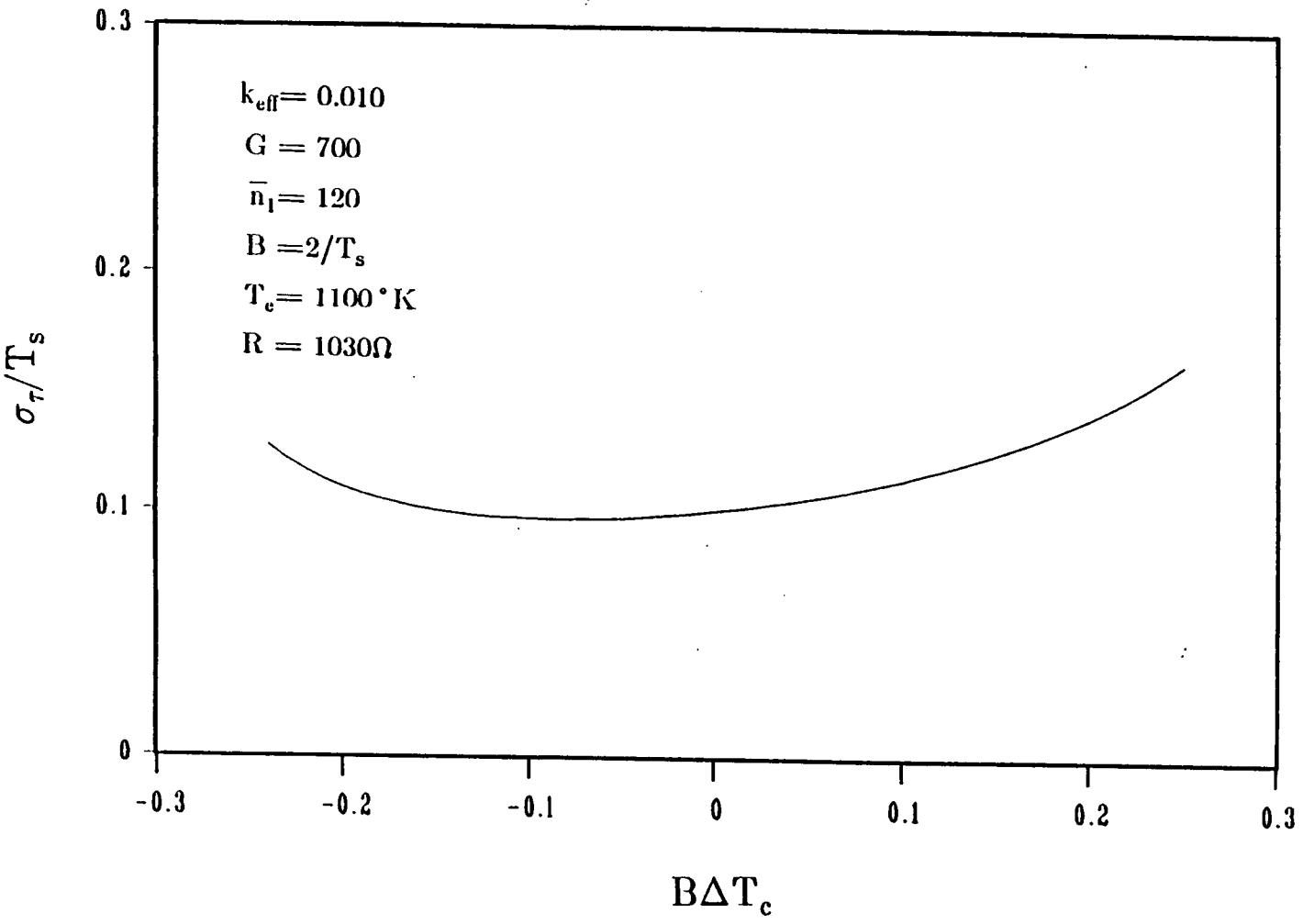

Figure 4.2. Normalized rms threshold crossing time, σ_τ/T_s, vs. normalized mean threshold crossing time, $B\Delta T_c$.

variance of threshold crossing time at $B\Delta T_c=0$ becomes

$$\sigma_\tau^2 = \frac{FG^2\lambda_1 + \dfrac{4KT_e}{Re^2}}{4BG^2\lambda_1^2}. \qquad (4.3.39)$$

Finally, substituting (4.3.39), (4.3.21), (4.3.20), (4.3.19) and (4.3.11) into (4.3.3), the variance of the phase error in the recovered slot clock is given by

$$\sigma_\phi^2 = QT_sB_L\cdot\{\exp\left[\frac{\pi^2}{BT_s}\cdot\frac{FG^2\overline{n}_s + 4KT_eT_s/Re^2}{G^2(\overline{n}_s)^2}\right] - 1\}. \qquad (4.3.40)$$

where $\overline{n}_s \approx \lambda_1 T_s$ is the average number of detected signal photons per PPM pulse.

The phase error variance, σ_ϕ^2, decreases as the bandwidth of the lowpass filter, B, increases. However, the effect of false triggering by noise spikes is not included in (4.3.40). This may contribute significantly to the overall phase error when the bandwidth of the lowpass filter becomes too large. In practice, B is also limited by the frequency responses of the APD and the amplifiers. In our experiment, $B=2/T_s$ was used.

4.4. Effects of Slot Clock Jitter on the Receiver BER

Jitter in recovered slot clock at the receiver results in the appearance of part of the received signal energy in an adjacent PPM slot, and hence acts as a source of background noise. If the integrators are ideal, the amount of signal energy which spills over into the adjacent slot is proportional, on average, to the amount of offset in the slot boundaries. If the timing offset of the recovered slot clock is ΔT_s, the fractional offset is given by $\epsilon = \Delta T_s/T_s$, and the effective average number of detected signal pho-

tons per PPM pulse becomes

$$\bar{n}_s' = (1-\epsilon)\bar{n}_s. \tag{4.4.1}$$

Assuming the actual number of detected background noise photons is $\bar{n}_0$, the effective average number of noise photons in the adjacent slot becomes

$$\bar{n}_0' = \bar{n}_0 + \epsilon\bar{n}_s \ . \tag{4.4.2}$$

The average number of detected noise photons in the remaining Q-2 time slots is still $\bar{n}_0$. The probability of a PPM word error is now given by

$$PWE(\epsilon) = 1 - \int_0^\infty p(x \mid \bar{n}_s' + \bar{n}_0)[\int_0^x p(y \mid \bar{n}_0')dy][\int_0^x P(z \mid \bar{n}_0)dz]^{Q-2}dx \tag{4.4.3}$$

where $p(u \mid \lambda T_s)$ is the probability density function of the APD output given in Section 2.4 for the average number of absorbed photons equal to $\bar{n}_s' + \bar{n}_0$, $\bar{n}_0'$, and $\bar{n}_0$, respectively.

Equation (4.4.3) usually requires excessive computation time when evaluated numerically. One alternative is to use the union bound as shown below,

$$PWE(\epsilon) \approx \int_0^\infty p(x \mid \bar{n}_s' + \bar{n}_0)\int_x^\infty p(y \mid \bar{n}_0')dydx + (Q-2)\int_0^\infty p(x \mid \bar{n}_s' + \bar{n}_0)\int_x^\infty p(y \mid \bar{n}_0)dydx. \tag{4.4.4}$$

The union bound gives a good approximation when the input signal to noise ratio is high and the timing offset is small, i.e. $\bar{n}_s/\bar{n}_0 >> 1$ and $\epsilon << 1$. A detailed description of an efficient numerical evaluation of (4.4.4) is given in Chapter 2.. The overall probability of a PPM word error is obtained by averaging (4.4.4) over ϵ. If the timing jitter is assumed to have Gaussian distribution with zero mean and standard deviation given as $\sigma_\epsilon = \sigma_\phi/2\pi$, it follows that

$$\mathrm{PWE} = \int_{-\infty}^{\infty} \mathrm{PWE}(\epsilon) \frac{1}{\sqrt{2\pi}\sigma_\epsilon} e^{-\frac{\epsilon^2}{2\sigma_\epsilon^2}} d\epsilon. \tag{4.4.5}$$

The receiver BER is related to PWE by (2.3.8).

In reality, none of the high speed integration circuits implemented in hardware is ideal and the amount of received signal energy in adjacent slots can not be determined simply by using (4.4.1) and (4.4.2). As an example, the integrations over the PPM time slots in our experiment were realized by sampling the output of the tapped delay line matched filter shown in Figure 3.8. Ideally, the impulse response of the matched filter should be a rectangle of width T_s, so that the output in response to a rectangular input pulse is a symmetric triangle of base $2T_s$. A sample at the top of the triangular waveform is proportional to the integration of the input signal over the previous time interval of length T_s. There is no intersymbol interference because the triangle waveform vanishes completely at the next sampling time. However, due to the limited bandwidth of the system, all three corners of the triangle become rounded. If the input rectangular pulse has zero rise time and fall time, and the lowpass filter has a "brick wall" like frequency response with cutoff frequency $2/T_s$, the output of the matched filter can be shown as in Figure 3.9. In practice, input rectangular pulses have finite rise and fall times, and no lowpass filters have true "brick wall" frequency response. In fact, it may be impossible to derive the actual distorted triangle shape, and consequently determine the exact amount of received signal energy that spills over into an adjacent slot due to timing offset. However, when the triangle output by the matched filter becomes rounded, the values of samples at the three corners of the triangle waveform become less sensitive to the sampling time accuracy. Consequently, jitter in

the recovered slot clock has less effect on the system performance than when a perfect integrator is used. Therefore, (4.4.5) can be used as an upper bound for the effect of jitter in the recovered slot clock on the receiver performance. The numerical results of (4.4.5) will be presented in the next section. To save computation time, only 40 points of the integrand were evaluated during the process of integration.

4.5. Experiments and Performance Measurements

4.5.1. The Electronic Circuit

The slot clock recovery system shown in Figure 4.1 was constructed. It used a high speed comparator (Motorola MC1650) as the threshold crossing detector and a monostable multivibrator (Motorola MC10198) as the pulse shaper. The inherent recovery time (dead time) of the multivibrator prevented it from triggering more than once within one slot period. Other types of pulse shaper may be used also. For example, the circuit shown in Figure 4.3 was tested and the resultant phase jitter of the output of the PLL was about the same as when using a monostable multivibrator. The pulse shaper of Figure 4.3 can work at very high speed although it consists of several relatively large size components, such as power splitters and coax delay cables.

The PLL consisted of a double balanced analog mixer (Motorola MC12002), an active second order loop filter, and a voltage controlled crystal oscillator (VCXO, Greenray N-471D). The active loop filter was built with a LM747NC operational amplifier. A detailed circuit diagram of the PLL is shown in Figure 4.4 along with a list of the component values.

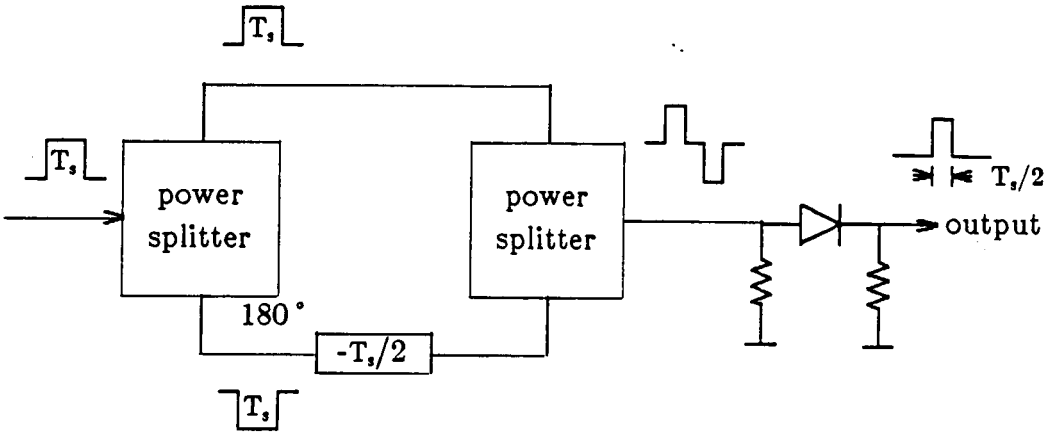

Figure 4.3. Example of another type of pulse shaper.

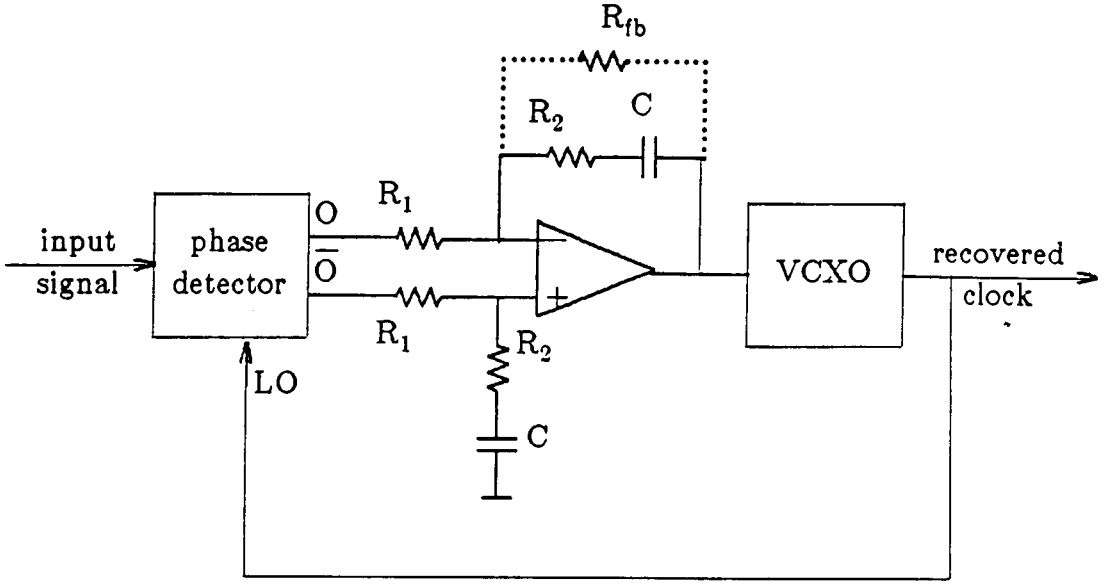

R_1=4.7KΩ, R_2=6.8KΩ
C = 0.10 μF
R_{fb} = 1MΩ
phase detector gain: K_d = 0.159 V/rad.
VCXO gain: $K_o = -2\pi \times 1.63 \times 10^4$ rad/sec./V
natural frequence $\omega_n \simeq$ 300 Hz
damping factor $\varsigma \approx 0.6$
loop noise bandwidth $B_L \simeq$ 1000 Hz

Figure 4.4. The PLL circuit.

All the analysis and measurements of the PLL were based on the model given by Gardner [52]. The linearized system function of the PLL is given as

$$H_{PLL}(s) = \frac{\theta_o(s)}{\theta_i(s)} = \frac{2\varsigma\omega_n s + \omega_n^2}{s^2 + 2\varsigma\omega_n s + \omega_n^2} \qquad (4.5.1)$$

with $\theta_o(s)$ the $\theta_i(s)$ the Laplace transforms of the output and input phase processes, ς the damping factor, and ω_n the natural frequency. These are given by $\omega_n=(K_oK_d/R_1C)^{-1/2}$ and $\varsigma=\omega_nR_2C/2$, where K_o and K_d are the gain of the VCXO and the phase detector, respectively. In the system built, $K_o=-2\pi\times1.63\times10^4$ radians/second/volt, and $K_d=0.0159$ volt/radian, therefore, the nature frequency and the damping factor were $\omega_n\approx2\pi\times300$ radians/second and $\varsigma\approx0.63$. These were verified by the experimental measurements. The resultant effective loop bandwidth was $B_L\approx1$ KHz. The lock-in range of the PLL was measured to be $\pm$40KHz, which was, as expected, the same as the tuning range of the VCXO. The pull-in range was found to be $\pm$5KHz when a large feedback resistor, shown as a dotted line in Figure 4.4, was used to prevent the operational amplifier from saturating due to small DC offsets of the input signals. In a real satellite-to-satellite communication system, a more sophisticated frequency acquisition circuit may have to be added to extend the pull-in range to cope with the Doppler effect.

4.5.2. Phase Error Measurement Apparatus

Timing errors were measured with the use of an rms phase error detector as shown in figure 4.5. A double-balanced frequency mixer (ASM-15) was used as the phase error detector. Under the conditions of small phase error, the output voltage of the frequency mixer can be approximated as

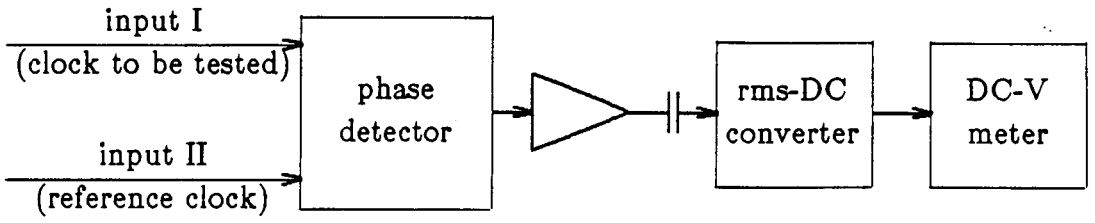

Figure 4.5. Apparatus of rms phase error measurements.

$V_{pd}=K_{pd}\sin\Delta\theta$, $\approx K_{pd}\Delta\theta$, where K_{pd} is the phase detector gain, and $\Delta\theta$ is the small phase difference between the two input signals. The amplified output of the phase detector was input to an rms to DC converter (Burr-Brown 4341), which had a bandwidth of DC to 450 KHz. The output of the phase detector often contained a DC component because it was difficult to completely balance out a static phase shift between the two input signals. Since the random phase jitter was often very small compared to static phase shifts, a coupling capacitor was inserted between the phase detector output and the rms to DC converter input. The capacitor and the input resistance of the converter formed an RC filter. The capacitor was chosen such that the 3dB cutoff frequency was below 0.1 Hz. Therefore, the bandwidth of the entire circuit was 0.1Hz—450KHz. Two identical slot clock waveforms with a series of known fixed phase shifts were used to calibrate the circuit. It was found that the circuit had a nearly constant gain of 7.62 V/radian for input phase shifts up to $\pm\pi/4$ radians.

Other sources of phase errors that appeared in the phase error measurements included noise of circuit components, such as the amplifiers, and the small phase jitter inherent in the VCXO. These phase errors were not included in our model used to compute the phase error, and therefore, they should be excluded from the final measurement results. The rms value of these phase errors was determined by feeding the jitter free clock signal into the PLL and then measuring the phase error of the VCXO output against the input clock. Since the phase jitter of the recovered slot clock is statistically independent of the VCXO noise and other circuit noise, the following relationship holds,

$$\sigma^2_{\phi\text{total}} = \sigma^2_{\phi} + \sigma^2_{\phi\text{n}} \tag{4.5.2}$$

where $\sigma_{\phi\text{total}}$ is the total measured rms phase error, σ_ϕ is the rms phase error of the recovered clock described by (4.3.20), and $\sigma_{\phi\text{n}}$ accounts for the phase error due to the noises of the VCXO and the circuit. The jitter of the recovered slot clock is then given by

$$\sigma_\phi = \sqrt{\sigma^2_{\phi\text{total}} - \sigma^2_{\phi\text{n}}} \approx \sigma_{\phi\text{total}}[\,1 - \frac{1}{2}(\frac{\sigma_{\phi\text{n}}}{\sigma_{\phi\text{total}}})^2] \qquad (4.5.3)$$

Measurements revealed that $\sigma_{\phi\text{n}}$ was about 7.6×10^{-4} radians. Since the smallest value of $\sigma_{\phi\text{total}}$ measured was about 5×10^{-3} radians, the approximation $\sigma_\phi \approx \sigma_{\phi\text{total}}$ was used throughout the measurements.

The average APD gain was set to G=700$\sim$800 which was the optimal value for the receiver with a common transmitter/receiver slot clock as described in Chapter 2 and 3. The optimal threshold level for the threshold crossing detector was set experimentally such that the observed phase error achieved a minimum. As predicted in Section 4.3.5, the optimal threshold was found to be near one half of the average peak amplitude of the APD output pulses, and small deviations from the optimal level resulted in negligible increases in the measured rms phase error.

4.5.3. Measurement Results

Figure 4.6 is a plot of the normalized rms phase error of the recovered slot clock, $\sigma_\phi/2\pi$, as a function of the average number of detected signal photons per information bit. The small squares represent the measurement data and the solid curve was obtained from the theoretical analysis. The feedback resistor shown as a dotted line in Figure 4.4 was disconnected during the phase error measurements in order to keep the analysis simple. The PLL was brought to lock by momentarily shorting the output and the input of the operational amplifier. The rms phase error increased by less than

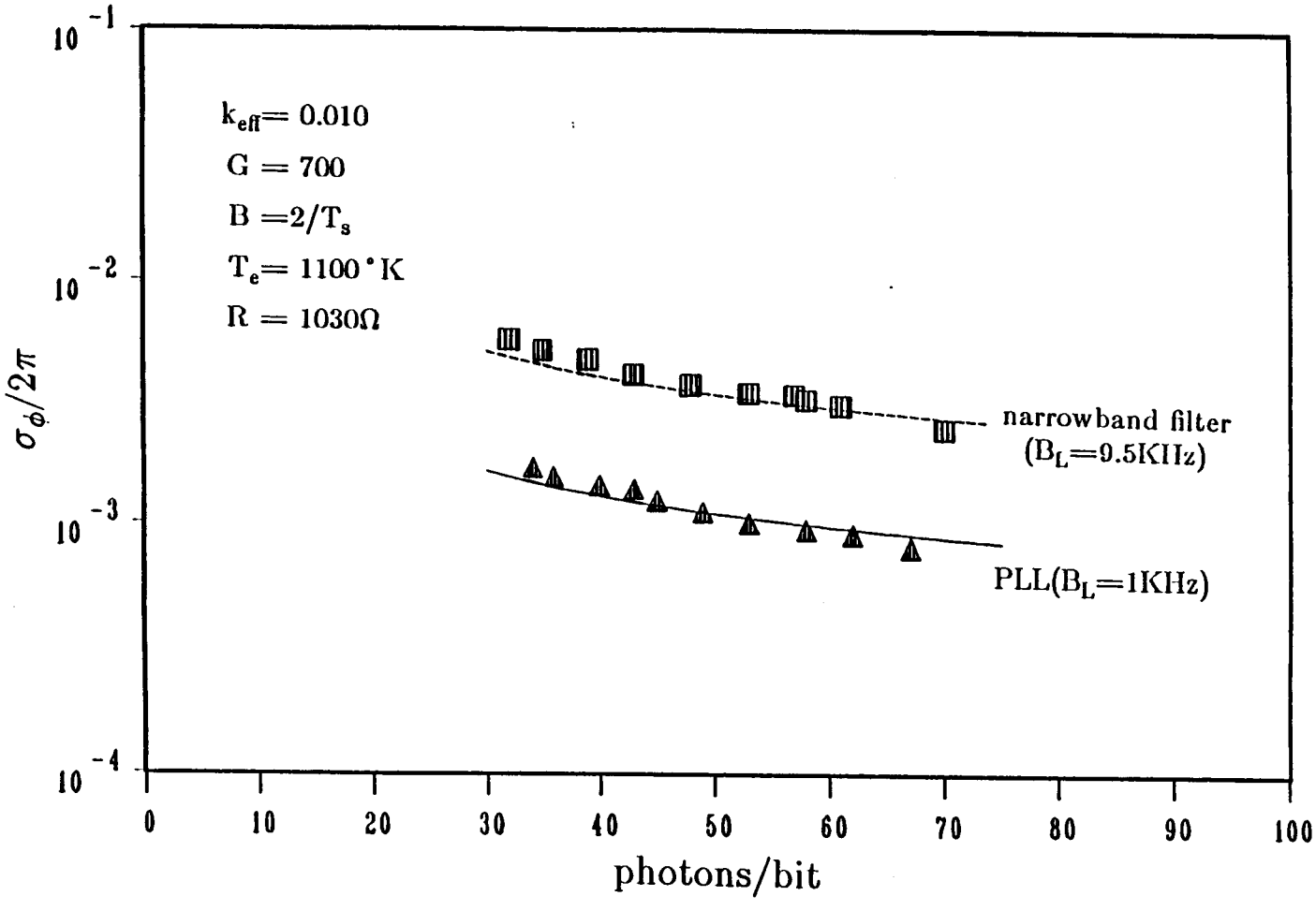

Figure 4.6. Normalized rms phase error of the recovered slot clock, $\sigma_\phi/2\pi$, vs. average number of detected signal photons per bit when using a PLL of B_L=1KHz and a narrowband filter of B_L=9.5KHz. The curves are the theoretical results of Section 4.4. The small squares and triangles represent the measurement data.

20% when the feedback resistor was connected. The measured phase errors of the recovered slot clock using a crystal bandpass filter of effective loop bandwidth B_L=9.5 KHz (full bandwidth 19KHz) are also plotted in Figure 4.6 (small triangles) along with the theoretical results (dashed curve). It is shown that the analysis agreed very well with the measurement data.

Finally, the recovered slot clock was used in the receiver and the system BER was measured as a function of the average number of detected signal photons per information bit. This was to show the effect of jitter in the recovered slot clock on system performance. The PPM word timing at this stage was provided by dividing the recovered slot clock with a 2 bit counter. The counter was synchronized as shown in Figure 4.7. The circuit worked as follows. The PPM word synchronization signal was a pulse train corresponding to counter state "00". The two synchronization signals from the transmitter counter and the receiver counter were compared with the use of an XOR gate. When the normally closed push button switch was open, the output of the XOR gate was used to gate the slot clock that drove the receiver counter until the two counters were synchronized. When the push button switch was released, the output of the XOR gate was overrid and the transmitter PPM word synchronization signal was disconnected from the receiver.

Figure 4.8 shows the results obtained with the slot clock regenerated by the PLL (small triangles) along with the results obtained with the common transmitter/receiver slot clock (small crosses). The solid curve corresponds to the numerical computations using Webb's approximation as described in Chapter 2 which assumed perfect slot timing recovery. The dotted curve represents the numerical results for the upper bound given in

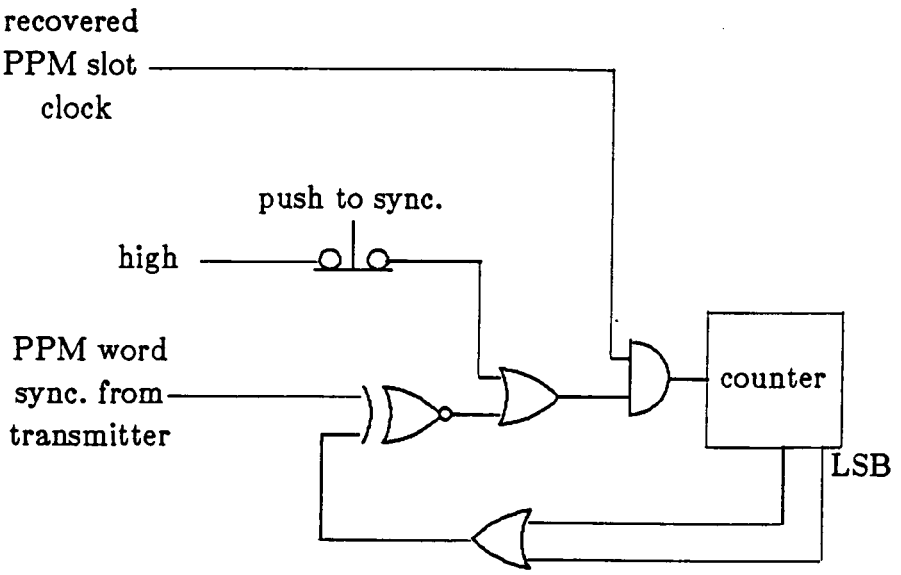

Figure 4.7. Initial synchronization of the receiver counter.

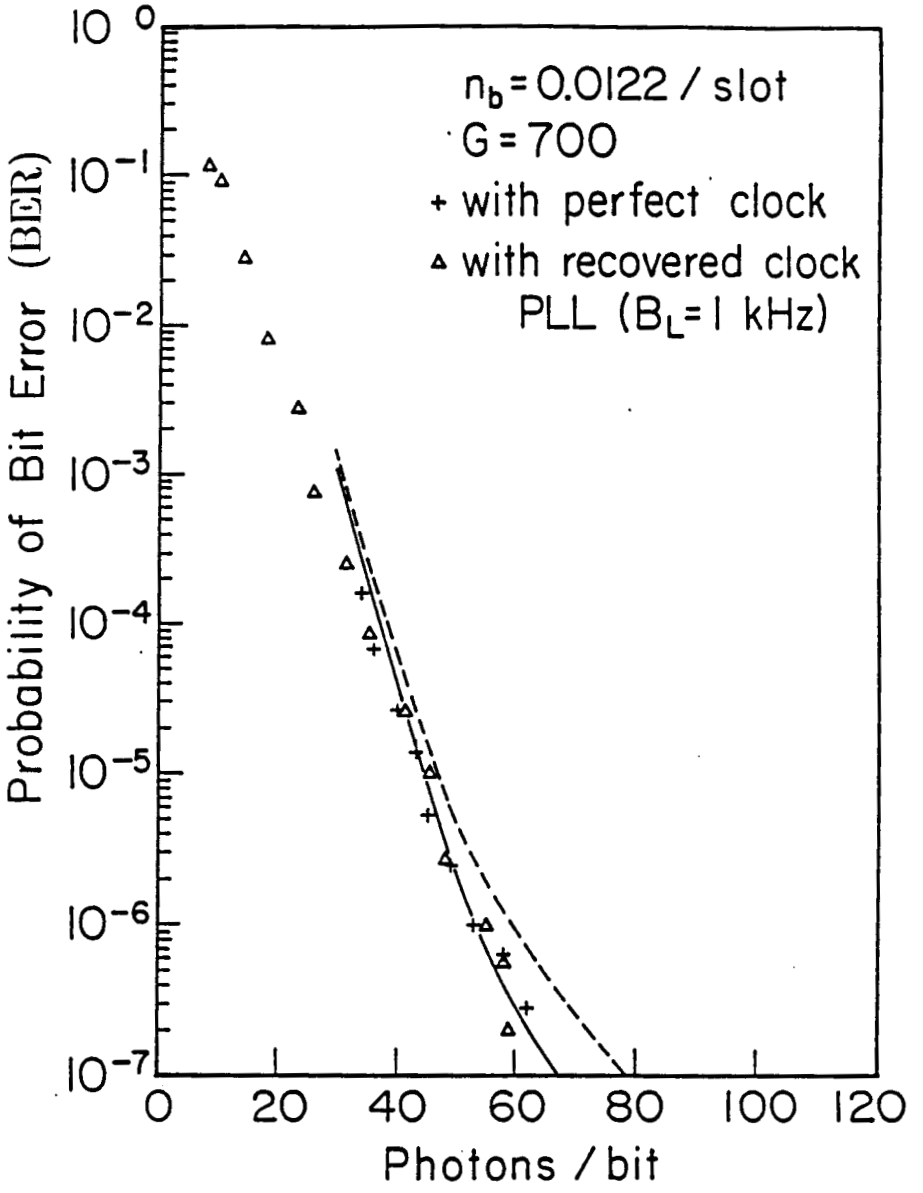

Figure 4.8. Receiver BER vs. average number of detected signal photons per bit when using the slot clock regenerated by a PLL (B_L=1KHz). The average number of detected background noise photons per time slot was $\bar{n}_0$=0.0122. The solid curve is obtained as in Chapter 2 assuming perfect slot timing recovery. The dashed curve represents the upper bound given by (4.4.5). The small crosses and triangles represent the experimental data when using a common transmitter/receiver slot clock (perfect slot timing recovery) and the recovered slot clock. Other parameters used were T_e=1100°K, k_{eff}=0.010, and R=1030Ω.

(4.4.5) with σ_ϕ determined by (4.3.40). It is shown that the recovered clock worked so well that no measurable penalty was observed in terms of detected photons per bit at a BER smaller than 10^{-2}. No cycle slipping and loss of lock were observed until the received optical power dropped below 15 photons per bit (30 photons per pulse) which corresponded to a bit error probability above 0.01. Figure 4.9 is similar to Figure 4.8 except that the bandpass filter (B_L=9.5KHz) was used in place of the PLL. The dotted curve is again the upper bound given by (4.4.5) and (4.3.40). Cycle slipping in this case occurred only when the detected optical power dropped below 30 photons per bit (60 photons per pulse). The measured performance was shown to be below the upper bound. The limited bandwidth of the matched filter made system performance less sensitive to small amounts of jitter in the times at which the output waveform of the matched filter were sampled.

Our results for the rms phase errors of the recovered slot clock are comparable with the theoretical results obtained by Chen [18] and Ling [19], which used different methods but did not consider the effect of the amplifier noise and the randomness of the APD gain. For example, under the conditions of $B_L T_s = 2.0\times10^{-5}$, 60 average detected photons per information bit, and no background radiation, the result in [18] corresponded to $\sigma_\phi/2\pi = 3.5\times10^{-4}$ using a square law device followed by a PLL. The result in [19] with an early-late gate scheme was $\sigma_\phi/2\pi = 8.2\times10^{-4}$. Our result under the same conditions was $\sigma_\phi/2\pi = 9.8\times10^{-4}$, and included the effects of the random APD gain and amplifier thermal noise.

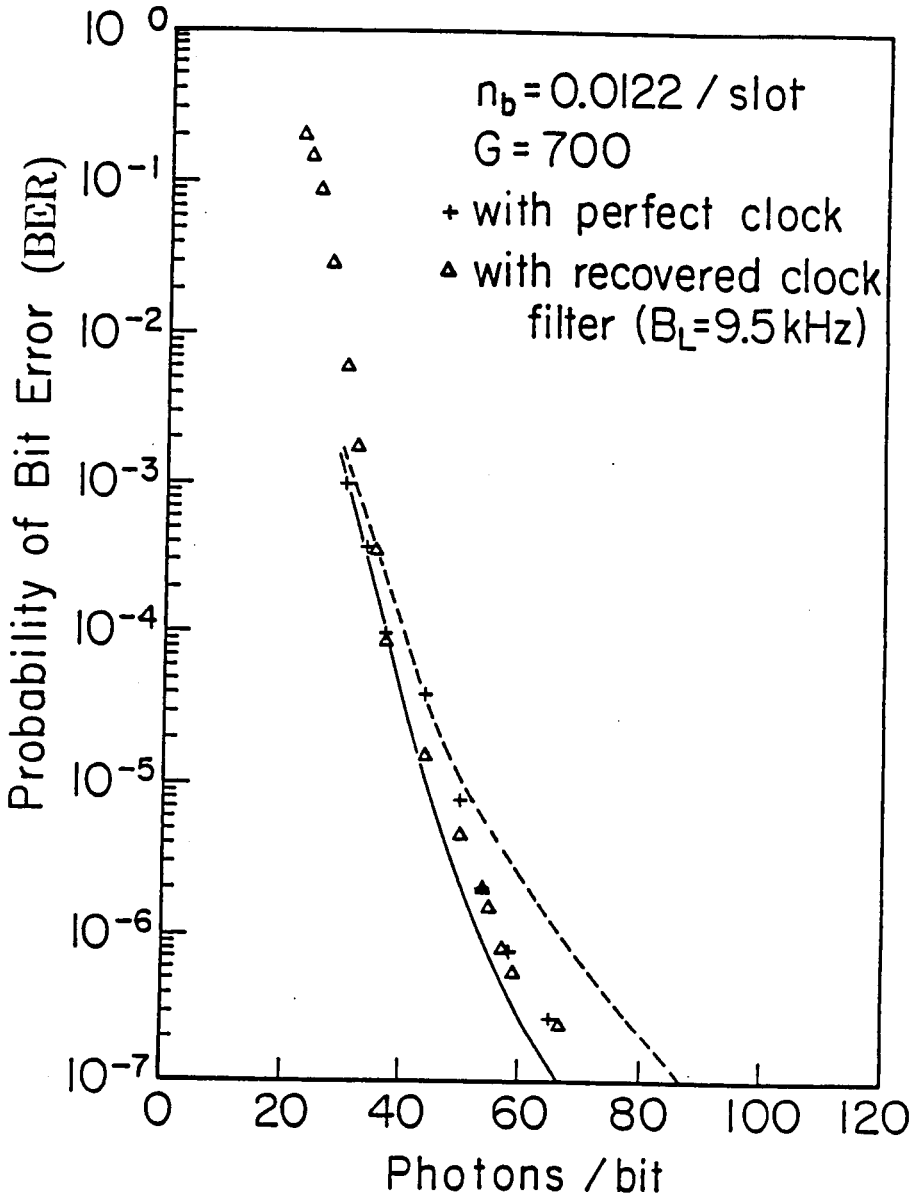

Figure 4.9. Same as Figure 4.8, but with the PLL being replaced by a narrowband filter of B_L=9.5KHz.

Chapter 5. PPM Word Timing Recovery

This chapter discusses a novel PPM word timing recovery scheme which regenerates the PPM word clock through the detection of back-to-back PPM pulse pairs in the received random PPM sequences and the use of a PLL. The presence of a recovered FPM slot clock with negligible phase jitter is assumed available.

5.1. Introduction

PPM word timing recovery is accomplished by establishing a PPM word clock which defines the boundaries of PPM words. Generally speaking, all the word timing recovery schemes for block codes may be applied to a PPM system because PPM signaling is in fact a block code. The most popular and easiest scheme to implement requires the inclusion of timing markers or synchronization patterns in the transmitted data stream [55]. The receiver detects these synchronization patterns and reconstructs the PPM word clock. The synchronization patterns usually consist of a sequence of code words which is relatively easily distinguished from random data. The transmitted data are usually divided into frames each of which consists of a synchronization pattern prefix and a number of data words. Word synchronization in this case is equivalent to frame synchronization. Frame synchronization should be based on a number of detected synchronization patterns in order to average out detection errors.

Several studies have already been done on frame synchronization methods for optical PPM communication systems [56, 57, 20, 58, 59, 60, 21, 22]. Two suggestions may be made here though they are not among the main topics of this chapter. First, synchronization

patterns in a PPM system may be constructed such that they are not a sequence of legitimate PPM words, e.g. three consecutive pulses followed by 3(Q-1) empty time slots. Such synchronization patterns are completely distinct from the random data sequence, and therefore, can be detected more reliably. Second, binary source data, such as computer data, are often coded and already contain synchronization patterns in binary form. In this case, PPM word synchronization may be combined with frame synchronization of the binary data through the use of the existing binary synchronization patterns. One can establishs PPM word synchronization by shifting the PPM word boundaries slot by slot until the frame synchronization patterns of the demodulated binary data appear as expected.

A special property of PPM signaling is that some PPM word subsequences in random PPM pulse trains can serve as synchronization patterns to determine the PPM word timing of the entire random PPM sequence [23]. One obvious example is a PPM sequence in which a PPM pulse in the Q th time slot is followed by a PPM pulse in the first time slot, e.g. the second and the third PPM pulses in the PPM sequence of Figure 5.1. This back-to-back pulse pair marks the boundary of the two consecutive PPM words as well as the boundaries of other PPM words in the sequence because there are exactly Q time slots in each PPM word. The probability that there exists at least one back-to-back pulse pair in a random PPM sequence of finite length is given in [59] although it is quite complicated to evaluate. A lower bound for the average frequency of occurrence of back-to-back PPM pulse pairs is given by $(1/Q)^2$. The probability that a random PPM sequence contains at least one pair of back-to-back PPM pulses approaches unity as the length of the sequence increases. Therefore, PPM

Figure 5.1. Example of a self synchronizable PPM sequence.

word synchronization can almost always be established in the absence of any inserted synchronization patterns as long as the memory of the receiver is sufficiently long. Because back-to-back pulses appear at random and errors may exist in the regenerated PPM sequence, a memory device and an averaging process are necessary in order to regenerate a smooth and accurate PPM word clock. This synchronization scheme eliminates the channel use "over head" associated with the transmission of inserted synchronization patterns. It also eliminates the need for framing the binary source data in order to insert the prescribed PPM synchronization patterns.

When the transmitted data are not equally likely but have some other probability distribution, some kind of source encoding may be necessary to ensure the appearance of back-to-back PPM pulse pairs. The binary source data can be either scrambled so that they appear equally likely, or they can be encoded such that the most likely data patterns correspond to PPM sequences that contain back-to-back pulse pairs. There are of course other PPM patterns besides back-to-back pulse pairs that may be used to recover the PPM word clock, for example, two PPM pulses 2(Q-1) time slots apart.

The rest of this chapter is organized as follows. Next section contains a detailed description of this PPM word timing recovery system based on the detection of back-to-back PPM pulse pairs and the use of a phase lock loop (PLL). A special PLL was also devised that locked the recovered word clock with the slot clock and therefore corrected the phase error presented in the recovered word clock. Section 5.3 contains the theoretical analysis of the random phase errors in the recovered PPM word clock. Section 5.4 describes the experimental system and the results of actual performance measurements.

5.2. Word Timing Recovery Based on the Occurrence of Back-to-back PPM Pulse Pairs.

The key components of the system consist of a back-to-back PPM pulse filter and a long memory averaging device. Since the PPM sequences regenerated from the maximum likelihood detector of Chapter 2 and 3 assume the existence of PPM word synchronization, they cannot be used for PPM word timing recovery. As a result, PPM sequences used for word timing recovery have to be regenerated by comparing the received photon energy integrated over each time slot against a threshold, as in an OOK system. The error probability of these PPM sequences is higher than for those of the maximum likelihood detector. Figure 5.2 gives a schematic diagram of the circuit. The photodetector output is integrated over each time slot with the use of a matched filter. The signal is then compared against a threshold level with the use of a comparator. The shift register samples the output of the comparator at the end of every time slot, and consequently, restores the PPM sequences. The two bit shift register and AND gate form a filter which passes only back-to-back pulse pairs. The PLL tracks on these pulses and generates a synchronous PPM word clock at the frequency $f=1/QT_s$ (Hz), with T_s the time duration of a PPM time slot.

The word clock output by the PLL contains random phase errors because the occurrences of back-to-back pulse pairs are random. However, since the PPM word clock should be in phase with the slot clock, phase errors of less than half a slot clock period can always be corrected by further phase locking the word clock to the slot clock. Here the recovered PPM slot clock is assumed to have much less phase jitter than the recovered word clock. Figure 5.3 shows the circuit that performs the phase

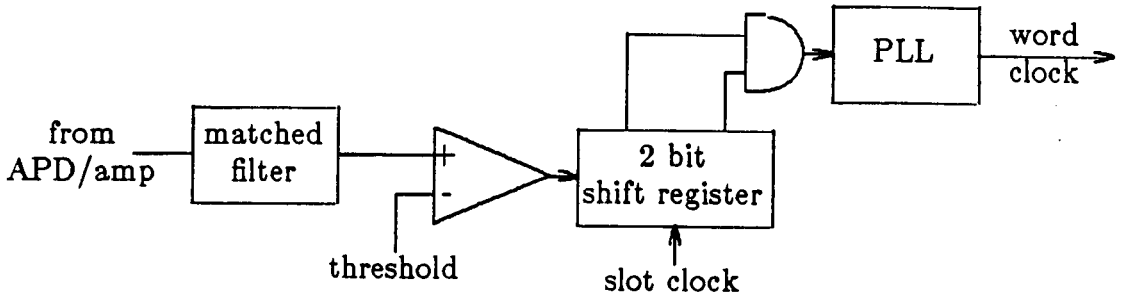

Figure 5.2. PPM word timing recovery circuit.

locking. The circuit is in fact a different kind of PLL with an exclusive NOR gate acting as the phase detector, an AND gate as the loop filter, and a counter driven by the slot clock as the voltage controlled oscillator. The input signal to this circuit consists of the word clock generated by the PLL of Figure 5.2. The exclusive NOR gate compares this input word clock with a second word clock obtained by dividing the slot clock with the use of the $\div Q$ counter. The two word clocks have the same waveform except for a possible time shift which may have resulted from the phase error in the input word clock and the randomness of the initial phase of the second word clock generated by the counter. The error signal output by the exclusive NOR gate is then used to gate the slot clock and subsequently shift the initial phase of the resultant word clock until the two are in lock. For example, assuming the two word clocks are initially out of phase π radians ($2T_s$ second time delay), the exclusive NOR gate will output a "low" state and block the first two ticks of the slot clock that drives the counter. The word clock output from the counter is then delayed by two slot clock periods and then is locked to the input word clock. The time for this circuit to lock up is less than one half a word clock cycle or $QT_s/2$ seconds. As shown in the timing diagram Figure 5.4, the error signal output by the exclusive NOR gate has no effect on the gated slot clock when the loop is in lock and the time shift of the input word clock due to random phase errors is within $+T_s/2$ second. In other words, when the loop is in lock, the word clock output by the counter is always in phase with the slot clock if the phase error of the input word clock is within $+\pi/Q$ radians. The input word clock may be delayed by $T_s/4$ seconds to change the maximum correctable phase error to $\pm\pi/2Q$ rad.

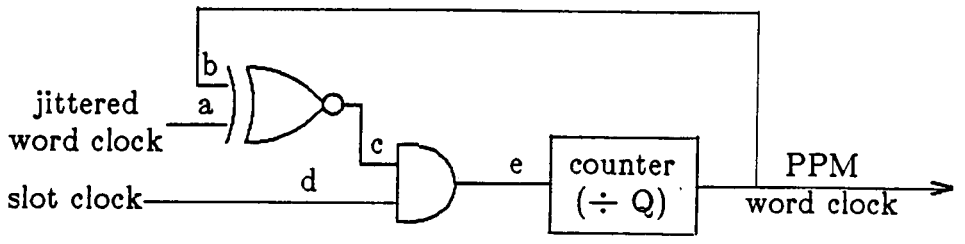

Figure 5.3. Phase lock between word clock and slot clock.

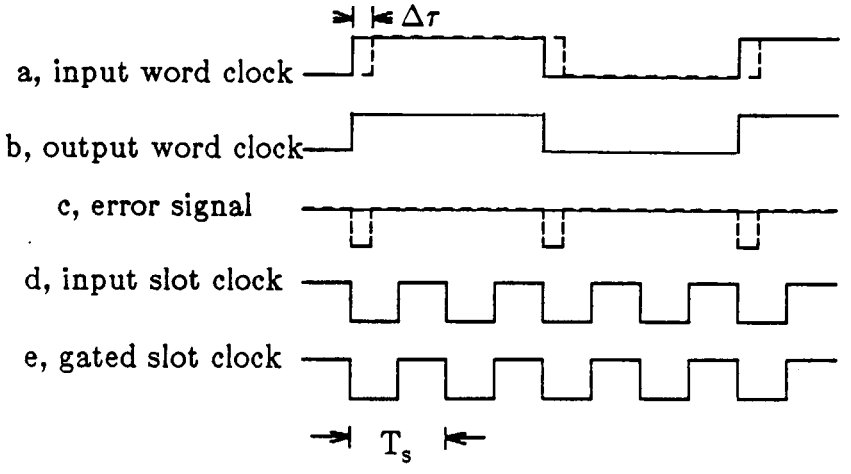

Figure 5.4. Timing diagram of the circuit in Figure 5.3.

5.3. Phase Error Analysis

5.3.1. Phase Error Variance of the PLL

The phase error variance of the word clock output by the PLL of Figure 5.2 can be computed in the same way as in Chapter 4.3.2. The phase error variance, σ_ψ^2, is given by

$$\sigma_\psi^2 = \frac{2B_L N(\omega_w)}{P_w} \quad (\text{rad.}^2), \tag{5.3.1}$$

where $N(\omega_w)$ represents the noise spectral density at the word clock frequency $\omega_w = 2\pi/QT_s$, and P_w represents the power of the sinusoidal component at the fundamental word clock frequency. The loop bandwidth of the PLL, B_L, is defined by

$$B_L = \int_0^\infty |H_{PLL}(2\pi f)|^2 df \quad (\text{Hz}) \tag{5.3.2}$$

where $H_{PLL}(2\pi f)$ is the transfer function of the linearized model of the PLL given in [52].

Both $N(\omega_w)$ and P_w in (5.3.1) can be obtained from the power spectrum of the input signal to the PLL of Figure 5.2, defined as

$$W(\omega) = \lim_{T\to\infty} \frac{1}{2T} E\{ | \int_{-T}^{T} y(t) e^{-j\omega t} dt |^2 \} \quad (\text{Watts/Hz}). \tag{5.3.3}$$

The input signal, y(t), to the PLL consists of rectangular pulses of width T_s seconds, each of which corresponds to the detection of a back-to-back pulse pair. The input signal can be modeled as

$$y(t) = \sum_{n=-\infty}^{\infty} a_n p(t - nQT_s) \quad (\text{volts}/\sqrt{R_i}), \tag{5.3.4}$$

where p(t) is the pulse shape function, $a_n = 0,1$ is a random variable corresponding to the presence or absence of an input back-to-back pulse

pair, and R_i is the input resistance of the PLL. When the transmitted random PPM words are mutually independent and equally likely, the probability of the a_n's can be written as

$$\begin{cases} \Pr(a_n=1) = (\frac{1}{Q})^2 \\ \Pr(a_n=1 \mid a_{n\pm1}=1) = 0 \,. \end{cases} \tag{5.3.5}$$

A detailed derivation of the power spectrum (5.3.3) is given in the next subsection.

5.3.2. Power Spectrum of the Input to the PLL

Taking $T=NQT_s$ with N an integer, the Fourier transform of (5.3.4) from -T to T becomes

$$\int_{-T}^{T} y(t)e^{-j\omega t}dt = P(\omega) \sum_{n=-N}^{N} a_n e^{-j\omega nQT_s} \tag{5.3.6}$$

where $P(\omega)$ is the Fourier transform of p(t). Since $E\{a_n a_n\}=1/Q^2$, $E\{a_n a_{n\pm1}\}=0$ and $E\{a_n a_m\}=E\{a_n\}E\{a_m\}=1/Q^4$ for $\mid n-m \mid \neq 0,1$,

$$E\{ \mid \int_{-T}^{T} y(t)e^{-j\omega t}dt \mid ^2\} = \mid P(\omega) \mid ^2 \sum_{m,n=-N}^{N} E\{a_n a_m\} e^{-j\omega QT_s(n-m)} \tag{5.3.7}$$

$$= \mid P(\omega) \mid ^2 [\, (2N+1)\frac{1}{Q^2} + \sum_{\substack{m,n=-N \\ \mid n-m \mid \neq 0,1}}^{N} \frac{1}{Q^4} e^{-j\omega QT_s(n-m)} \,]$$

$$= \mid P(\omega) \mid ^2 [\, (2N+1)(\frac{1}{Q^2} - \frac{1}{Q^4})]$$

$$- \frac{2N}{Q^4}(e^{-j\omega QT_s} + e^{j\omega QT_s}) + \frac{1}{Q^4} \mid \sum_{n=-N}^{N} e^{-j\omega QT_s n} \mid ^2] \,. \tag{5.3.8}$$

The power spectrum (5.3.3) becomes

$$W(\omega) = \lim_{T\to\infty} \frac{1}{2T} E\{ \mid \int_{-T}^{T} y(t)e^{-j\omega t}dt \mid ^2\}$$

$$= |P(\omega)|^2 \left[\frac{1}{QT_s}\left(\frac{1}{Q^2} - \frac{1}{Q^4}\right) - \frac{1}{QT_s}\cdot\frac{2}{Q^4}\cos(\omega QT_s) \right.$$

$$\left. + \frac{1}{Q^4}\lim_{T\to\infty}\frac{1}{2T}\left|\sum_{n=-N}^{N} e^{-j\omega QT_s n}\right|^2 \right]. \qquad (5.3.9)$$

As in Section 4.3.3, the last term of (5.3.9) can be written as

$$\lim_{T\to\infty}\frac{1}{2T}\left|\sum_{n=-N}^{N} e^{-j\omega QT_s n}\right|^2 = \frac{2\pi}{(QT_s)^2}\sum_{k=-\infty}^{\infty}\delta(\omega-2\pi k/QT_s). \qquad (5.3.10)$$

Substituting (5.3.10) into (5.3.9), the power spectrum becomes

$$W(\omega) = |P(\omega)|^2\left[\frac{1}{QT_s}\left(\frac{1}{Q^2}-\frac{1}{Q^4}\right) - \frac{1}{QT_s}\cdot\frac{2}{Q^4}\cos(\omega QT_s)\right]$$

$$+ |P(\omega)|^2\frac{1}{Q^4}\frac{2\pi}{(QT_s)^2}\cdot\sum_{k=-\infty}^{\infty}\delta(\omega-2\pi k/QT_s). \qquad (5.3.11)$$

The first term in (5.3.11) represents the noise spectral density and the second term represents discrete spectral components at the PPM word clock frequency and its harmonics. Therefore, the power of the sinusoidal signal component and the noise spectral density at the frequency $\omega_w = 2\pi/QT_s$ can be expressed as

$$P_w = |P(\omega_w)|^2\frac{1}{Q^4}\frac{2}{(QT_s)^2} \quad \text{(Watts)} \qquad (5.3.12)$$

$$N(\omega_w) = |P(\omega_w)|^2\frac{1}{QT_s}\left[\frac{1}{Q^2}\left(1-\frac{3}{Q^2}\right)\right] \quad \text{(Watts/Hz)}. \qquad (5.3.13)$$

Substituting (5.3.12) and (5.3.13) into (5.3.1), the phase error variance of the regenerated PPM word clock becomes

$$\sigma_\psi^2 = QB_LT_s(Q^2-3) \quad \text{(rad.}^2\text{)}. \qquad (5.3.14)$$

5.3.3. Design of the PLL

Since the circuit in Figure 5.3 can correct for phase errors up to $\pm\pi/2Q$ radians, the loop noise bandwidth of the PLL should be designed such that $\sigma_\psi \ll \pi/2Q$. The probability of having uncorrectable phase errors is there-

fore negligibly small. However, B_L should be large enough for the PLL to have a reasonable tracking capability. The tracking range of the word timing recovery system should be close to that of the PPM slot timing recovery system.

The acquisition time of the entire word clock recovery system is determined mainly by the PLL in Figure 5.2. The PLL can lock up within one cycle if the frequency of the received word clock and the free running frequency of the VCXO are within the lock-in range [52]. If the input word clock frequency is out of the lock-in range, some kind of added frequency acquisition circuit may be necessary and the acquisition time becomes limited by the circuit used. Details about added frequency acquisition circuits can be found in [52]. The frequency uncertainty of the input PPM word clock is caused by the jitter of the clock oscillator in the transmitter and frequency shifts due to the Doppler effect. The jitter of a crystal clock oscillator is typically 0.005% and the percentage Doppler shift of the PPM word clock is equal to the ratio of the relative velocity between the transmitter and the receiver to the velocity of light.

The PLL may slip cycles or even break lock after acquisition is completed. The average cycle slipping time may be used as a lower bound for the average time during which the receiver can maintain its PPM word synchronization. It is shown in [52] that the time between cycle slips is exponentially distributed with mean given by

$$T_{AV} = (1/B_{L)} \exp(\pi SNR_L), \tag{5.3.15}$$

where B_L is the loop bandwidth given by (5.3.2), and SNR_L is the loop signal to noise ratio defined as

$$SNR_L = \frac{P_W}{2B_L N(\omega_W)} . \tag{5.3.16}$$

5.3.4. Effects of Detection Errors

Errors in the PPM sequences output by the comparator cause the signal to noise ratio to decrease at the input of the PLL. There are two types of errors, namely, misses and false alarms. Misses in the detection cause the signal power to decrease and false alarms cause the noise to increase. A quantitative analysis is given as follows.

First, if there are only misses present, (5.3.5) should be rewritten as

$$\begin{cases} Pr(a_n=1) = (\frac{1-p_{ms}}{Q})^2 \\ Pr(a_n=1 \mid a_{n\pm1}=1) = 0 \end{cases} \tag{5.3.17}$$

where p_{ms} is the probability of a miss. A derivation similar to the one in Section 5.3.2 shows the signal power and the noise power spectral density become

$$P_w' = (1-p_{ms})^4 P_w \quad \text{(Watts)} \tag{5.3.18}$$

$$N'(\omega_w) = (1-p_{ms})^2 \frac{Q^2-3(1-p_{ms})^2}{Q^2-3} N(\omega_w) \quad \text{(Watts/Hz)} \tag{5.3.19}$$

where P_w and $N(\omega_w)$ are the signal power (5.3.12) and noise spectral density (5.3.13) in the absence of detection errors.

When there are both misses and false alarms, the signal power is still given by (5.3.18), but the noise spectral density increases because some of the detected back-to-back pulse pairs are erroneous. An erroneous pulse pair may consist of either two false alarm pulses or a false alarm pulse and a correctly detected PPM pulse. The probability that two false alarmed pulses appear in a pair of consecutive time slots is given as

$$p_1 = \begin{cases} p_{fa}^2 \frac{2}{Q}, & \text{if the two slots are in one PPM word} \\ p_{fa}^2 (\frac{Q-1}{Q})^2, & \text{if the two slots are in two PPM words} \end{cases} \quad (5.3.20)$$

where p_{fa} is the probability of a false alarm. The probability that one false alarmed pulse and a correctly detected PPM pulse appear in a pair of consecutive time slots is given as

$$p_2 = \begin{cases} 2\frac{1}{Q}p_{fa}, & \text{if the two slots are in one PPM word} \\ 2\frac{1}{Q}\frac{Q-1}{Q}p_{fa}, & \text{if the two slots are in two PPM words.} \end{cases} \quad (5.3.21)$$

The factor of two in (5.3.21) accounts for the two different orders possible for the two pulses. If the probability of a false alarm is small, the effects of the appearance of incorrect back-to-back pulse pairs from two false alarmed pulses can be neglected since $p_1 \ll p_2$ as $p_{fa} \ll 1$. Under these assumptions, the extra noise input to the PLL of Figure 5.2 due to false alarms alone can be approximated as

$$n_{fa}(t) = \sum_{n=-\infty}^{\infty} b_{nl}p(t-c_nT_s-nQT_s) + b_{nr}p[t-(c_n+1)T_s-nQT_s] \quad (5.3.22)$$

where b_{nl}, b_{nr} are two random variables, equal to zero or one, which indicate that a false alarmed pulse has appeared to the left or right side of the correctly detected PPM pulse, and c_n is an integer from 0 to (Q-1) used to indicate the pulse position of the n th PPM word. For equally likely random data, the c_n's form a set of i.i.d. random variables with uniform distribution. The probabilities of b_{nl} and b_{nr} can be approximated as $Pr(b_{nl}=1) = Pr(b_{nr}=1) = p_{fa}$.

The power spectral density of this extra noise signal at the PPM word clock frequency can be derived as follows. The Fourier transform of (5.3.22)

from -T to T is given by

$$\int_{-T}^{T} n_{fa}(t)e^{-j\omega t}dt = P(\omega)\sum_{n=-N}^{N} e^{-j\omega nQT_s}.e^{-j\omega c_n T_s}(b_{nl}+ b_{nr}e^{-j\omega T_s}) \quad (5.3.23)$$

where $T=NQT_s$. The power spectrum at frequency $\omega_w=2\pi/QT_s$ can be written as

$$\begin{aligned} N_{fa}(\omega_w) &= \lim_{T\to\infty}\frac{1}{2T}E\{\,|\int_{-T}^{T} n_{fa}(t)e^{-j\omega_w t}dt\,|^2\} \\ &= |P(\omega_w)|^2 \lim_{T\to\infty}\frac{1}{2T}\sum_{n,m=-N}^{N} E\{e^{-j2\pi(c_n-c_m)/Q}\} \\ &\quad \cdot E\{(b_{nl}+b_{nr}e^{-j2\pi/Q})(b_{ml}+b_{mr}e^{j2\pi/Q})\}\,. \end{aligned} \quad (5.3.24)$$

For $m\neq n$,

$$\begin{aligned} E\{e^{-j2\pi(c_n-c_m)/Q}\} &= |E\{e^{-j2\pi c_n/Q}\}|^2 \\ &= |\frac{1}{Q}\sum_{c_n=0}^{Q-1} e^{-j2\pi c_n/Q}|^2 = 0\,. \end{aligned} \quad (5.3.25)$$

For $m=n$,

$$E\{e^{-j2\pi(c_n-c_m)/Q}\} = 1 \quad (5.3.26)$$

and

$$E\{(b_{nl}+b_{nr}e^{-j2\pi/Q})(b_{ml}+b_{mr}e^{j2\pi/Q})\} = 2p_{fa}+2p_{fa}^2\cos\frac{2\pi}{Q} \approx 2p_{fa}\,. \quad (5.3.27)$$

Substituting (5.3.25), (5.3.26) and (5.3.27) into (5.3.24),

$$N_{fa}(\omega_w) = 2p_{fa}\frac{1}{QT_s}|P(\omega_w)|^2 = 2p_{fa}\frac{Q^4}{Q^2-3}N(\omega_w)\,, \quad (5.3.28)$$

where $N(\omega_w)$ is given by (5.3.13). The total noise power spectral density at the input to the PLL of Figure 5.2 can be considered approximately as the sum of (5.3.19) and (5.3.28), i.e.

$$N_{total}(\omega_w) = [\,(1-p_{ms})^2\frac{Q^2-3(1-p_{ms})^2}{Q^2-3} + 2p_{fa}\frac{Q^4}{Q^2-3}\,]\,N(\omega_w)\,, \quad (5.3.29)$$

with $N(\omega_w)$ given by (5.3.13). The phase error variance at the output of the

PLL can be obtained by substituting (5.3.18), (5.3.12), (5.3.29), and (5.3.13) into (5.3.1), as

$$\sigma_\psi^2 = QB_L T_s\left[\frac{Q^2}{(1-p_{ms})^2} - 3 + \frac{2p_{fa}Q^4}{(1-p_{ms})^4}\right] . \tag{5.3.30}$$

5.3.5. Probabilities of Miss and False Alarm

As in Chapter 2, the input signal to the comparator can be considered as the electrical charge output from the APD and an equivalent amount of amplifier thermal noise accumulated over a time slot. The probabilities of a miss or false alarm are given by

$$p_{ms} = \int_{-\infty}^{x_T} p(x \mid \bar{n}_1)dx \tag{5.3.31}$$

$$p_{fa} = \int_{x_T}^{\infty} p(x \mid \bar{n}_0)dx \tag{5.3.32}$$

where x_T is the threshold level, $\bar{n}_1$ and $\bar{n}_0$ are the average numbers of the detected photons over a PPM time slot when a PPM pulse is present and absent, respectively, and $p(x \mid \bar{n})$ with $\bar{n}=\bar{n}_1,\bar{n}_0$ is the appropriate probability density function. The average symbol error rate of the regenerated PPM sequence is related to p_{ms} and p_{fa} by

$$p_e = \frac{1}{Q}p_{ms} + \frac{Q-1}{Q}p_{fa} . \tag{5.3.33}$$

The average APD gain should be determined by the PPM detection circuit rather than the word timing recovery circuit. The threshold levels applied to the comparator may be varied such that the symbol error probability, (5.3.33), is minimized.

The probability density function, $p(x \mid \bar{n})$, using Webb's approximation

is given in Chapter 2.4 as

$$p(x \mid \bar{n}) = \sum_{m=0}^{\infty} p(x \mid m)P(m \mid \bar{n}) \tag{5.3.34}$$

$$p(x \mid m) = \frac{1}{\sqrt{2\pi\sigma}} e^{-\frac{(x-\bar{x}_m)^2}{2\sigma^2}} \tag{5.3.35}$$

$$\text{with } \bar{x}_m = me + I_s T_s \text{ and } \sigma_2 = (eI_s + \frac{2KT_e}{R})T_s$$

and

$$P(m=0 \mid \bar{n}) = e^{-\bar{n}} \tag{5.3.36}$$

$$P(m \mid \bar{n}) = \frac{1}{(2\pi\bar{n}G^2F)^{1/2}} \cdot \frac{1}{[1+\frac{m-G\bar{n}}{\bar{n}GF/(F-1)}]^{3/2}} \cdot \exp\left[-\frac{(m-G\bar{n})^2}{2\bar{n}G^2F(1+\frac{m-G\bar{n}}{G\bar{n}F/(F-1)})}\right], \quad m>0 \tag{5.3.37}$$

where m represents the number of secondary photoelectrons generated by the APD, I_s is the APD surface leakage current, e is the electron charge, K is Boltzmann's constant, T_e is the equivalent noise temperature, R is the load resistance seen by the APD, F is the excess noise factor given by $F = k_{eff}G + (2-1/G)(1-k_{eff})$, k_{eff} is the ratio of the APD ionization coefficients of electrons and holes, and G is the average APD gain.

When (5.3.31) and (5.3.32) are evaluated numerically, the infinite sum of (5.3.34) can be approximated by the first M terms. The resultant errors may by upper bounded as follows. Substituting (5.3.34) through (5.3.37) into (5.3.31),

$$\epsilon_{ms} = \int_{-\infty}^{x_T} \sum_{m=M_{ms}}^{\infty} p(x \mid m)P(m \mid \bar{n}_1)dx$$

$$< \int_{-\infty}^{x_T} p(x \mid M_{ms})dx \cdot \sum_{m=M_{ms}}^{\infty} P(m \mid \bar{n}_1)$$

$$< \int_{-\infty}^{\frac{x_T-\bar{x}_{M_{ms}}}{\sigma}} \frac{1}{\sqrt{2\pi}} e^{-\frac{t^2}{2}} dt . \qquad (5.3.38)$$

Next, substituting (5.3.34) through (5.3.37) into (5.3.32),

$$\epsilon_{fa} = \int_{x_T}^{\infty} \sum_{m=M_{fa}}^{\infty} p(x \mid m) P(m \mid \bar{n}_0) dx$$

$$< \sum_{m=M_{fa}}^{\infty} P(m \mid \bar{n}_0) < \int_{M_{fa}-1}^{\infty} P(m \mid \bar{n}_0) dm . \qquad (5.3.39)$$

As shown by (2.6.15) through (2.6.18) of Chapter 2, for $M_{fa} >> \bar{n}_0 G$,

$$\epsilon_{fa} < \frac{\bar{n}_0 e^{\bar{n}_0/2F}\sqrt{F}}{2\sqrt{\pi(F-1)^3}} \cdot \int_0^{\frac{2GF}{M_{fa}-1-\bar{n}_0 G}} \frac{1}{\sqrt{u}} e^{-1/u} du . \qquad (5.3.40)$$

The values of M_{ms} and M_{fa} should be chosen such that $\epsilon_{ms} << p_{ms}$ and $\epsilon_{fa} << p_{fa}$ based on (5.3.38) and (5.3.40). For example, the values used to obtain the numerical results presented in the next section were $M_{ms} > M_T + 30{,}000$ and $M_{fa} > 100{,}000$ for $\epsilon_{ms}, \epsilon_{fa} < 10^{-8}$. The parameters used were: $G=800$, $k_{eff}=0.010$, $\bar{n}_0=0.0122$, $I_s=11.9$nA, $T_r=1000\,^{\circ}$K, $R=1030\Omega$, and $T_s=20$ns.

The error bounds derived above can also be used to compute the error probability of communication systems that use OOK signaling.

5.4. Experiments and Measurements

The circuits shown in Figure 5.2 were constructed. The matched filter was the same one shown in Figure 3.7. The comparator used was a Motorola MC1650 and the shift register was a Motorola MC10141. The PLL was constructed as shown in Figure 5.5, which consisted of a phase detector (MC12002), an operational amplifier (LN747NC), and a VCXO.

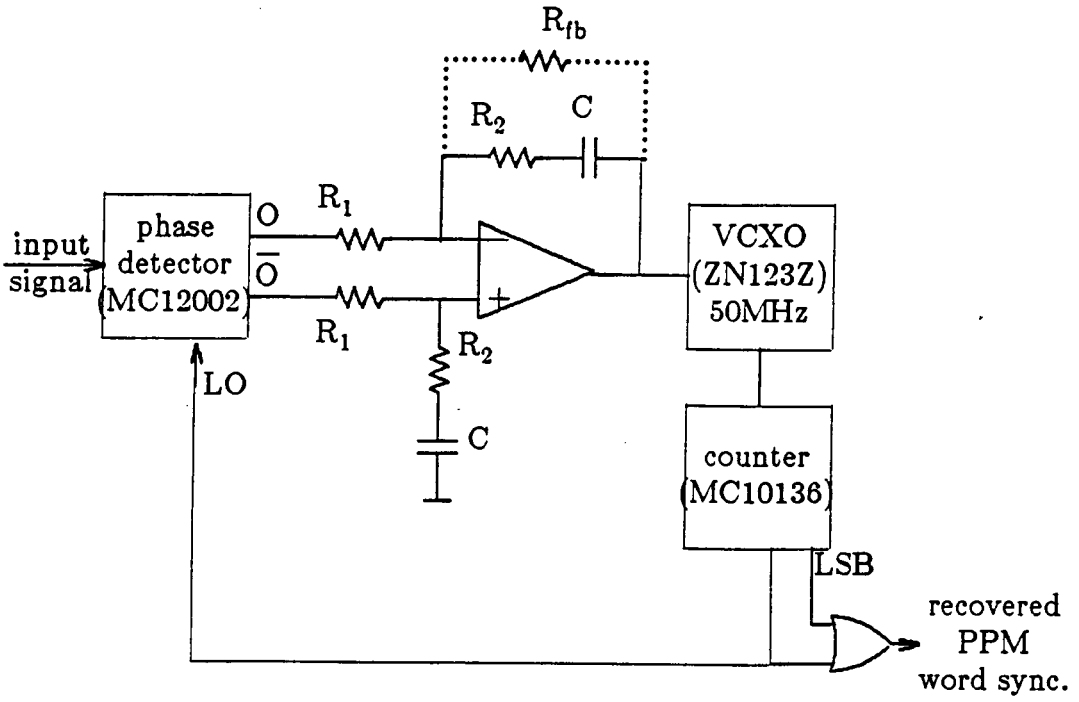

R_1=1.0KΩ, R_2=10KΩ
$C = 0.10\ \mu F$
$R_{fb} = 4.7M\Omega$
phase detector gain: $K_d = 7.64\times10^{-3}$ V/rad.
VCXO gain: $K_o = -2\pi\times1.08\times10^3$ rad/sec./V
nature frequence $\omega_n \simeq 110$ Hz
damping factor $\varsigma \approx 0.4$
loop noise bandwidth $B_L \simeq 380$ Hz

Figure 5.5. The PLL circuit for PPM word timing recovery.

The VCXO (Greenray ZN-123Z) had a center frequency of 50MHz which was Q=4 times the word clock frequency. Therefore, a two bit counter (MC10136) had to be used to divide the frequency down to the correct value of 12.5 MHz. The OR gate in Figure 5.5 served to generate a unsymmetric word clock, which was "low" only when the counter output was "00", the same as the PPM word synchronization signal defined in Chapter 3. The resistors and capacitor values of the loop filter were R_1=1KΩ, R_2=10KΩ, and C=0.1μF. The resultant loop noise bandwidth was $B_L \approx$380Hz according to [52]. The standard deviation of the phase error of the output word clock was σ_ψ=0.020 radian according to (5.3.14).

The circuit of Figure 5.3 was implemented equivalently as shown in Figure 5.6. The symmetric input word clock in Figure 5.3 was changed to the the PPM word synchronization signal generated by the PLL in Figure 5.5. The output of the $\div$Q counter in Figure 5.3 was also changed to the PPM word synchronization signal. No separate circuit shown in Figure 5.6 was actually built since it was already part of the PPM demodulator shown in Figure 3.11. Since all phase errors within $\pm\pi/2Q=\pm$0.39 radians could be corrected, the final word clock contained virtually no phase errors at all.

The average symbol error rate of the detected PPM pulse sequences, p_e, was measured with apparatus similar to that shown in Figure 3.13. The results are plotted in Figure 5.7 (small squares) as a function of the average number of detected signal photons per information bit. The threshold level applied to the comparator was optimized for each received optical signal power level such that the measured symbol error rate achieved a minimum. The numerical results of (5.3.33) are shown as the solid curve in Figure 5.7. At the optimal threshold levels, of the total number of symbol errors in the

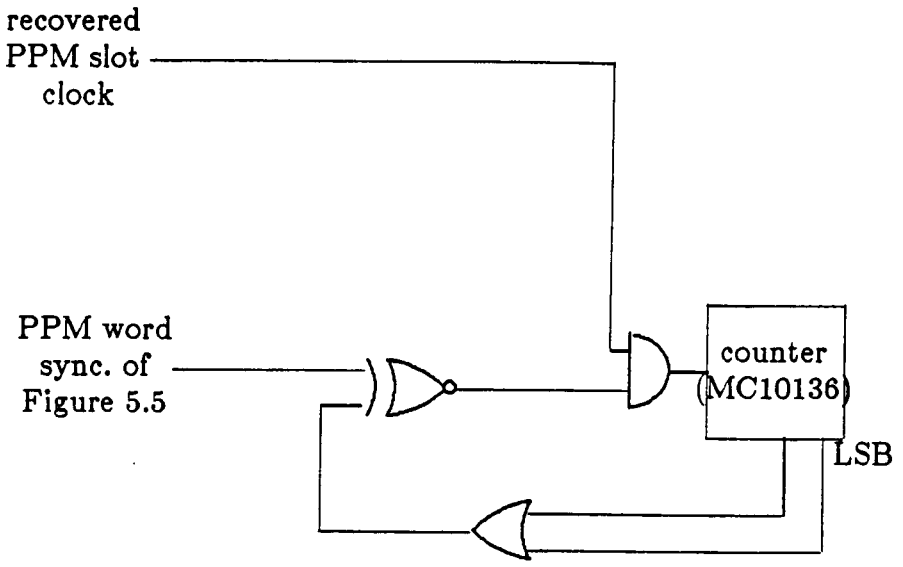

Figure 5.6. Implemented circuit of Figure 5.3.

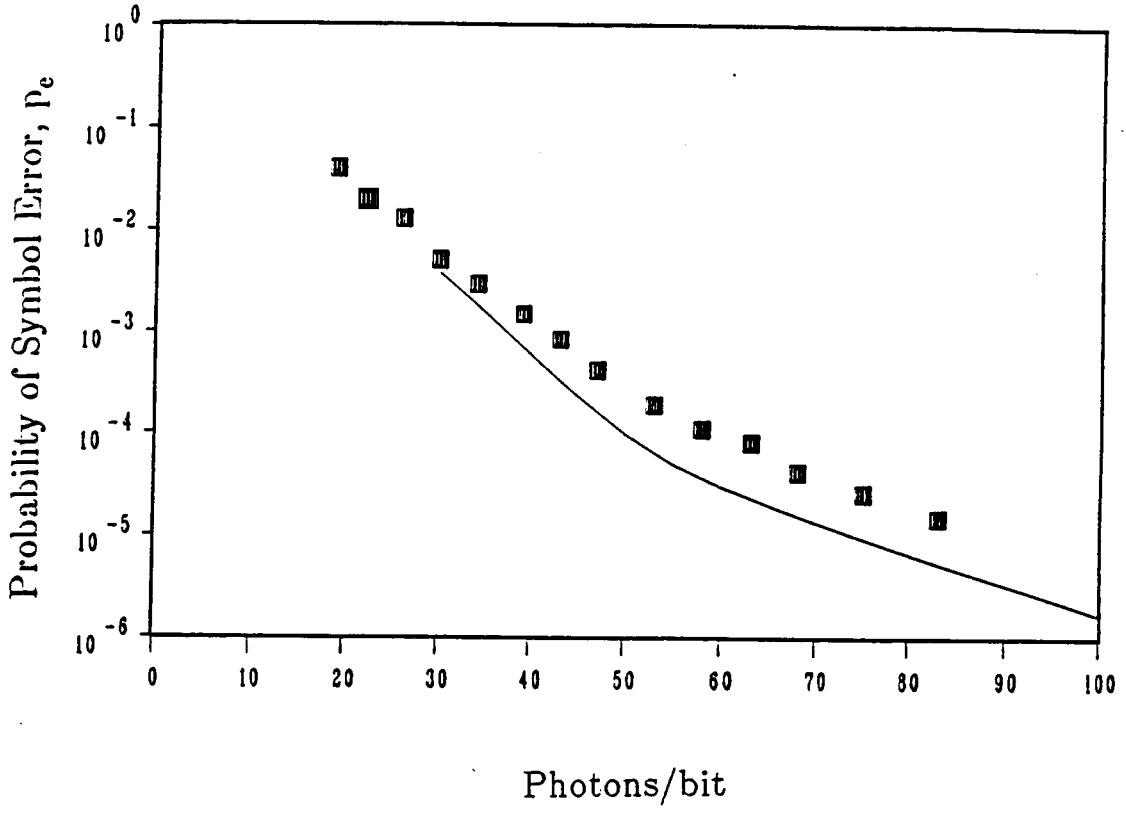

Figure 5.7. Probability of symbol errors of the PPM sequences at the shift register of Figure 5.2 vs. average number of detected photons per information bit at optimal threshold levels. The small squares represent the measurement data and the solid curve represents the theoretical result given by (5.3.33). The parameter values used were: background radiation level $\bar{n}_0 = 0.0122$, average APD gain G=300, k_{eff}=0.010, APD quantum efficiency η=77%, APD load resistance R=1030 ohm, equivalent noise temperature T=1100°K, APD surface leakage current I_s=11.9nA and PPM slot time T_s=20ns.

detected PPM pulse sequences, 1/Q are misses and (Q-1)/Q are false alarms. In other words, we can use $p_{ms} \approx p_e/Q$ and $p_{fa} \approx p_e(Q-1)/Q$ when evaluating (5.3.18), (5.3.29) and (5.3.30).

Figure 5.8 is a plot of normalized optimal threshold levels as a function of the average number of detected photons per bit, where the normalization is with respect to the average peak values of the matched filter output. It was found that the optimal threshold levels varied from 24% to 32% of the peak value of the matched filter output. The average DC level of the matched filter output was 25% of the peak value and independent of the received signal level. Since the matched filter and the comparator were AC coupled, the effective threshold levels were automatically adjusted close to the optimal values if the threshold level was fixed at zero volts.

Figure 5.9 shows a measured power spectrum of the input signal to the PLL of Figure 5.2 at a received signal level corresponding to an average of 55 photons/bit. The false alarm and miss probabilities were negligibly small ($\sim 10^{-4}$) at this received signal level. The measured data agreed well with the results obtained from the theoretical analysis (5.3.12) and (5.3.13) for rectangular ECL pulses and a 50Ω input resistance. The calculated power of the sinusoidal word clock component was -22.4dBm according to (5.3.12), and the measured power, indicated by the marker in Figure 5.9, was about -23.4dBm. The one sided noise spectral density according to (5.3.13) was -82dBm/Hz, and the measured value was about -83dBm/Hz (-32dBm in the 100KHz resolution bandwidth). The PLL loop signal to noise ratio defined by (5.3.16) was therefore about 30 dB. The average cycle slipping time is, according to (5.3.15), over 10 years for SNR_L=9.1dB and B_L=380Hz. This implies that the system could achieve PPM word

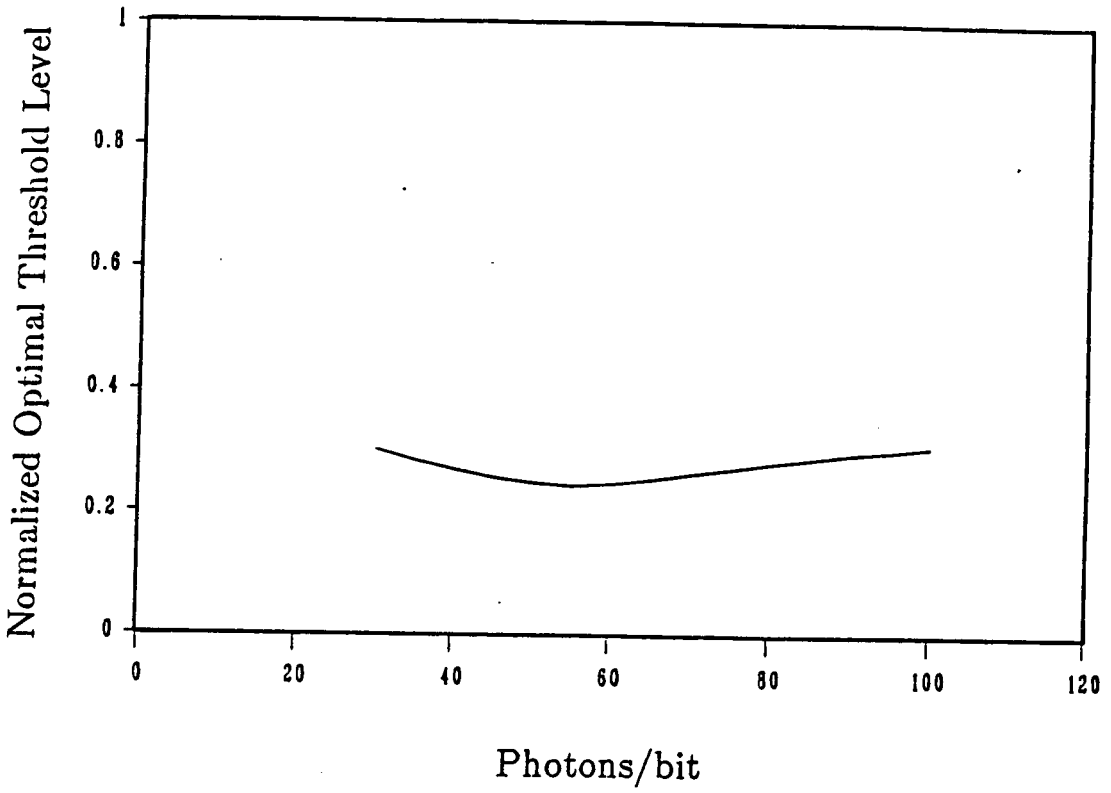

Figure 5.8. Optimal threshold levels normalized to the peak matched filter output vs. detected photons/bit. The parameters used are the same as those in Figure 5.7.

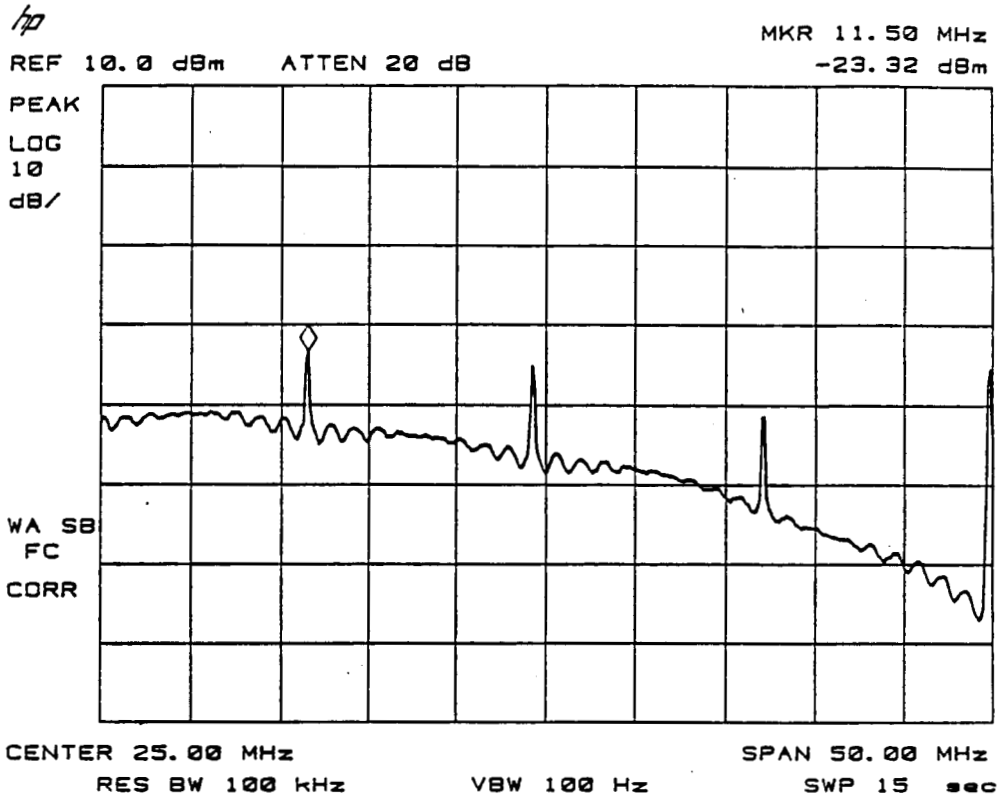

Figure 5.9. Power spectrum of the signal input to the PLL of Figure 5.2, at 55 detected signal photons per bit. Other parameters were the same as in Figure 5.7.

clock synchronization with virtually no cycle slips at a SNR_L much lower than 30dB. The system could tolerate at least a 20dB reduction in SNR_L that might result from higher error rates in the detected PPM pulse sequences and/or less frequent occurrences of back-to-back PPM pulse pairs.

To show the effects of misses and false alarms, the threshold level applied to the comparator of Figure 2 was changed such that detection errors in the PPM pulse sequences consisted mainly misses or false alarms. The results of the measurements agreed with those obtained from the theoretical analysis, (5.3.18) and (5.3.29). For example, when the threshold level was set well above the optimal value such that $p_{fa} \ll p_{ms}$ and $p_{ms}=0.121$, the measured signal power and noise spectral density decreased by about -2.46 dB and -1.1 dB, respectively. These values were close to the values computed from (5.3.18) and (5.3.29), of -2.24dB and -0.90 dB. When the threshold level was set well below the optimal value such that $p_{ms} \ll p_{fa}$ and $p_{fa}=0.0267$, the measured noise spectral density increased by about 3.0 dB, which again agreed with the value predicted by (5.3.29), of 3.1 dB.

Finally, the recovered word clock, the recovered slot clock, and the PPM detection/demodulation circuit were all integrated together as a completely self synchronized optical PPM receiver. The bit error probabilities of the output binary sequences were measured as a function of the average number of detected photons per information bit, as shown in Figure 5.10 (small triangles). The results from the experiments and the numerical computations under perfect receiver synchronization are also plotted in Figure 5.10 (small squares and the solid curve). It was found that the performance

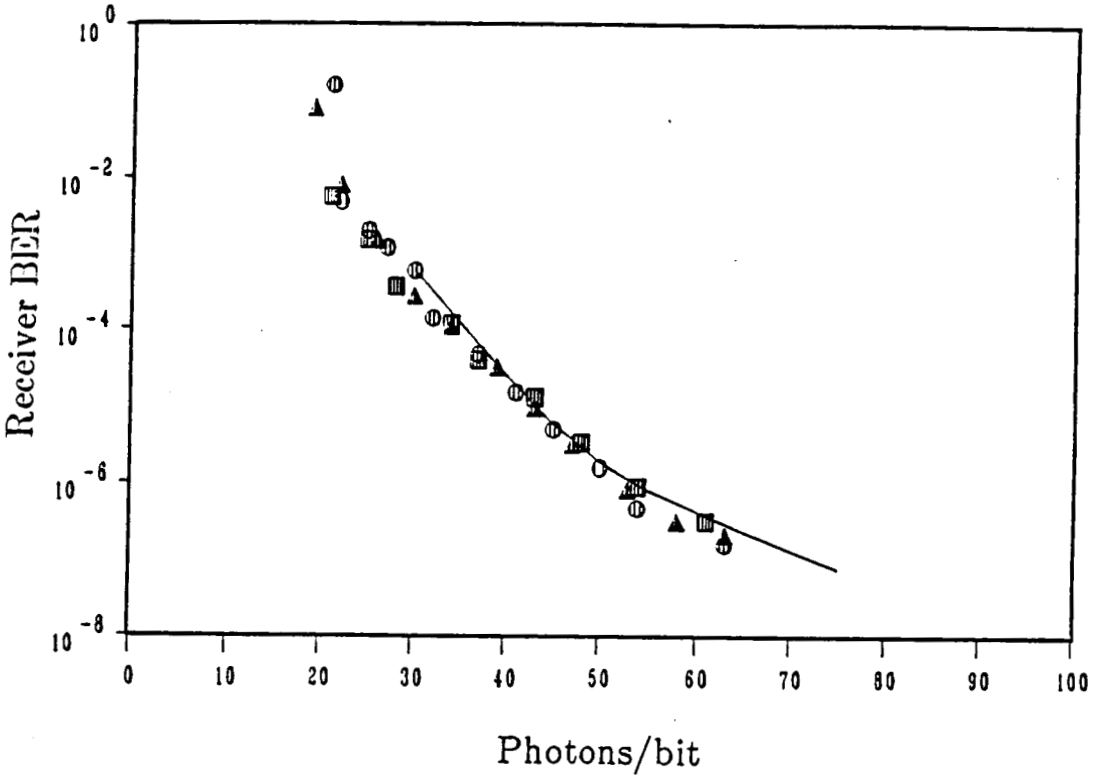

Figure 5.10. Receiver BER vs. average number of detected signal photons per information bit. The small triangles represent the measurement data when the recovered clocks were used. The small squares represent the measurement data with perfect slot and word timing recovery. The solid curve are the numerical results assuming perfect timing recovery, as given in Chapter 2. The small circles represent the measured results when a fixed threshold level of the comparator was used. The parameters used were the same as those in Figure 5.7.

of the self synchronized receiver was the same as the performance of the receiver with perfect synchronization for received optical signal levels greater than 25 detected photons/bit. The receiver could acquire and hold both slot and word synchronization for received optical signal levels as low as 20 detected photons/bit (40 photons per PPM pulse). The small circles in Figure 5.10 represent the measured data when the matched filter and the comparator were AC coupled and the threshold level of the comparator was fixed at zero volts. The measured bit error probabilities were unaffected by the use of this close to optimal threshold level except when the received signal levels were very low.

Chapter 6. Conclusion

The results of this research showed that a Q=4 PPM direct detection optical communication system operating at a source data rate of 25 Mbits/second using an AlGaAs laser diode transmitter (λ=833nm) and a silicon APD photodetector could achieve BER$\leq 10^{-6}$ at received optical signal energies corresponding to an average of 55 detected photons per information bit. The receiver sensitivity achieved was the closest to the quantum limit yet reported for an optical communication system of this type. Analysis and experiments also showed that reliable PPM slot clock and word clock waveforms could be regenerated at the receiver with negligible phase jitter at these values of received optical signal energy. The theoretical analysis of receiver BER and rms phase errors in the recovered clock waveforms agreed very well with the results of actual measurements.

A new algorithm for computing receiver bit error rates was developed which used the nearly exact Webb's approximation for the APD output photocurrent but did not require excessively long computation times. The widely used Gaussian approximation for the APD output was found to severely underestimate the optimal value of the average APD gain and overestimate the receiver BER when the average number of detected background noise photons was less than one per PPM slot time. The numerical results obtained using Webb's approximation agreed well with the experimental measurements under very low background radiation levels. The results obtained using the Gaussian approximation converged with those obtained with the nearly exact Webb's approximation when the average number of detected photons per slot time due to background radiation noise was greater than ten. The mathematical model and the computational

procedure developed in Chapter 2 may be applied to other types of optical receivers that use APD photodetectors, such as a semiconductor laser radar system.

A transition detector type PPM slot clock recovery scheme was devised, analyzed, and implemented. This slot clock recovery scheme was demonstrated to be a reliable and simple way to regenerate PPM slot clock waveform from the received random PPM signals. A mathematical model was developed to accurately compute the rms phase error of the regenerated slot clock and it agreed very well with the results of experimental measurements. The limited bandwidth of the electronics allowed the PPM detection circuit to tolerate, without compromising the receiver sensitivity, an rms phase error which was less than one percent of a slot clock cycle. The experimental slot clock recovery system achieved an rms phase error of well below one percent of a slot clock cycle with a PLL loop bandwidth of 1KHz, or 2×10^{-5} of the slot clock frequency. Use of the recovered slot clock resulted in no observable penalty in the number of detected signal photons per bit required to achieve BER over the range of 10^{-3} to 10^{-7}. The theoretical analysis and the experimental measurements also showed that the PLL could be replaced with a simple crystal bandpass filter if the bandwidth of the filter was one half the PLL noise bandwidth. The only disadvantage in using a bandpass filter was the inherent static phase error in the output when the input frequency was shifted.

A novel PPM word timing recovery scheme was devised based on the detection of back-to-back PPM pulse pairs in the received random data and the use of a PLL. Unlike other existing word synchronization schemes, no prescribed synchronization patterns need to be periodically inserted in the

data stream and there is no channel use overhead associated with insertion of these patterns. Reliable PPM word clock recovery could be obtained as long as the transmitted random data were equally likely or back-to-back PPM pulses appeared frequently enough. The maximum acquisition time of the PPM word synchronization was on the order of a PPM word clock cycle. False PPM word synchronization might only occur when the received PPM sequence contained too few back-to-back pulse pairs. This could be avoided by properly encoding or encrypting the source data. A special PLL was devised which synchronized the recovered PPM word clock to the slot clock and therefore corrected the random phase error in the recovered word clock with respect to the slot clock. The recovered slot clock was more reliable and contained less jitter because the input signal to the slot clock recovery system consisted of PPM sequences which had a fixed pulse rate regardless of the transmitted data patterns. Use of the recovered PPM word clock in the receiver did not cause any measurable degradation in the receiver performance when compared to a receiver with perfect word timing.

The next phase of this work is to increase the binary source data rate to 100 megabits/second or more. The assumptions of rectangular pulse shape may not be valid because the rise and fall times of the output laser light pulses become comparable to the pulse width. The amplifier noise spectral density is no longer white but grows with frequency beyond 100 MHz. Therefore, a more complicated model for the amplifier noise given by Personick [32] has to be used. The thermal noise from the APD load resistor will increase because the resistance has to be reduced to provide the necessary preamplifier bandwidth. On the other hand, the PPM slot time over which the amplifier noise current is integrated becomes shorter. The overall

amplifier noise electron charge integrated over a time slot will be slightly larger than at the lower data rates , but the amplifier noise can always be overridden by increasing the average APD gain. The major factor which limits the receiver performance is the number of detected background noise photons per PPM time slot. If the extinction ratio of the laser can be kept high, the number of the background noise photons per slot decreases as the slot time decreases because the background radiation intensity and the APD bulk leakage current are constant. Therefore, the receiver sensitivity is expected to improve somewhat at a higher source data rate.

Appendix A. Computer Program of BER vs Photons/bit Using Webb's Approximation*.

```
      INTEGER   Q,IER
      REAL IS,KEFF,n0
      external FF
      common um1,varm,s1,cx1,GN0,DL0,DOS2,MM0,NN0,N00,n0,c13
c
c     System parameters
c
c n1=detected photons in a slot containing a PPM pulse
c n0=detected background noise photons per slot
c G=average APD gain
c
      n1=110
      G=700.0
      n0=0.0122
c
c Q=number of slot in a PPM word
c R=APD load resistance (Ohm)
c Tr=equivalent noise temperature (Kalvin)
c Keff=ratio of ionization coefficients of APD
c Is=APD surface leakage current in nanoamperes
c T=PPM slot duration in nanoseconds
c
      Q=4
      R=1030.0
      Tr=1100.0
      Keff=0.010
      Is=11.9
      T=20.0
c
c     Limits and increments of the summation indecies
c
c LG=increments of average APD gain
c
      LG=30
c
c MM1=lower limit of the outer sum index
c NN1=upper limit of the outer sum index
c N11=increments of the outer sum index
c
      MM1=n1+1
      rn1=real(n1)
      f=keff*G+(2.0-1.0/G)*(1.0-keff)
      xNN1=34.*f*g+2.*g*rn1
      NN1=int(xNN1)
      N11=n1*LG
c
c MM0=lower limit of the inner sum index
c NN0=upper limit of the inner sum index
c NN0=increment of the inner sum index
c
      N00=300
      MM0=100
      NN0=150000
```

* This is the basic version of the Fortran programs used in Chapter 2 for fixed parameter values only. Loops may be added to run for several sets of parameter values at a time. To use the program, first edit the system parameter section, compile the program, and then link it with IMSL (single precision) subroutine.

```
c
c Print out the upper limits and increments to the terminal
c
      print *,'N1/DN1/N0/DN0=  ',NN1,N11,NN0,N00
c
c
c     Globle Constants
c
c Constants used in the sums
c
      D1S=FLOAT(n1)*G*G*F
      D1=sqrt(D1S)
      D1S2=2.*D1S
      D0S=n0*G*G*F
      D0=sqrt(D0S)
      D0S2=2.*D0S
      DL1=REAL(n1)*G*F/(F-1.)
      DL0=N0*G*F/(F-1.)
      GN1=G*real(n1)
      GN0=G*n0
      cx1=Is*T*1.0e-18
      cx3=2.0*1.38e-23*Tr*T*1.0e-9/R
      cx4=1.6e-19*Is*T*1.e-18
      varm=cx3+cx4
      s1=sqrt(varm)
c
c s16=integration interval
c b=smallest temr to be collected for the outer sum
c c13=common factor of part of the inner sum
c
      s16=s1*6.0
      b=1.e-9*2.0*3.1416*D0/real(Q-1)
      c13=sqrt(2.0*3.1416)*D0
c
c c1=common factor of the sums
c
      c11=2.0*3.14*D1/real(N11)
      c12=sqrt(2.0*3.14)*D0/(real(q)-1.0)
      c1=c11*c12
c
c Absolute and relative errors of the integration routine
c
      AERR=0.0
      RERR=0.01
c
c
c     Beginning to Calculate
c
      xx=0.0
      do 100 m1=MM1,NN1,N11
      x1=real(M1)-GN1
      x2=x1/DL1+1.0
      x3=1.0/x2
      x5=x1*x1/D1S2*x3
      Pmn1=x3*sqrt(x3)*exp(-x5)
      um1=real(m1)*1.6e-19+cx1
      Am1=um1-s16
      Bm1=um1+s16
c
c call IMSL numerical integration subroutine "DCADRE"
c
      pem1=DCADRE(FF,Am1,Bm1,AERR,RERR,ERROR,IER)
      if (pem1.lt.b) goto 150
100   xx=xx+Pmn1*Pem1
c
c Print out the actual upper limit of the outer sum index
c
150   print *,'actual N1= ',m1
```

```
c
c Compute probability of word error and BER
c
      PWD=1./c1*xx
      c2=real(Q)
      c3=c2/2./(c2-1)
      BER=c3*PWD
c
c Print out results in file "FOR101.DAT"
c
      write(101,200)
200   format(1x,'MBIT/S  N0/T    G    KEFF   IS   RTEMP  RLOAD')
c
c     BR=bit rate
c     N=photons/bit (approximate ns=n1)
      rL=alog(c2)/alog(2.0)
      L=int(rL)
      BR=1./T/L*1000.0
      N=int(N1/L)
      write(101,250)BR,n0,G,KEFF,IS,TR,R
250   format(1x,F5.0,F7.4,F7.0,F6.4,F6.2,2F7.0)
      write(101,270)
270   format(1x,'Photons/bit    BER')
      write(101,300)N,BER
300   format(1x,I7,E15.4)
900   continue
      stop
      end
c
c Subroutine to compute the integrand
c
      REAL FUNCTION FF(X)
      real n0
      common um1,varm,s1,cx1,GN0,DL0,D0S2,MM0,NN0,N00,n0,c13
c
c   The inner sum from MM0 to NN0
c
      y=0.0
      do 500 m0=MM0,NN0,N00
      um0=real(M0)*1.6e-19+cx1
      y2=(um0-x)/s1
c
c  call IMSL subroutine "mdnor" = error function
c
      call mdnor(y2,y3)
      y4=real(m0)-GN0
      y5=y4/DL0+1.0
      y6=1.0/y5
      y7=y4*y4*y6/D0S2
      Pmn0=y6*sqrt(y6)*exp(-y7)
      yy=pmn0*y3
500   y=yy+y
c
c     The inner sum from 1 to MM0
c
      ys=0.0
      do 600 m0=1,MM0
      um0=real(m0)*1.6e-19+cx1
      y2=(um0-x)/s1
      call mdnor(y2,y3)
      y4=real(m0)-GN0
      y5=y4/DL0+1.0
      y6=1.0/y5
      y7=y4*y4*y6/D0S2
      Pmn0=y6*sqrt(y6)*exp(-y7)
      yy=pmn0*y3
600   ys=yy+ys
      y=y*real(n00)+ys
```

```
c
c     The m=0 term
c
      z1=(cx1-x)/s1
      call mdnor(z1,z2)
      z=z2*c13*exp(-n0)
      y=y+z
c
c    The complete integrand
c
      yy1=X-um1
      yy2=yy1*yy1/2.0/varm
      FF=exp(-yy2)/s1*y
      return
      end
```

References

1. K. Bhasin (editor), *Optical Technologies for Communication Satellite Applications,* Proceedings of SPIE, vol. 616, 1986.

2. J. C. Graebner and W. F. Casdmam, "Advanced communication technology satellite: system description," *IEEE Global Telecommunication Conference (GlobeCom'86),* Houston, TX, Dec. 1-4, 1986, Conference Record, vol. 1, pp. 559-567.

3. H. Lutz and G. Otrio (editors), *Optical Systems for Space Applications,* Proceedings of SPIE, vol. 810, part II, 1987.

4. B. G. Evans and R. J. Colby (editors), *International Journal of Satellite Communications,* vol. 6, no. 2, (Special issue on intersatellite links), April - June, 1988.

5. D. L. Snyder, *Random Point Processes* , John Wiley & Sons, New York, 1975.

6. J. Salz, "Modulation and detection for coherent lightwave communications," *IEEE Communications Magazine,* vol. 24, , no. 6, pp. 38-49, June 1986.

7. T. Okoshi, "Ultimate performance of heterodyne/coherent optical fiber communications," *Journal of Lightwave Technology,* vol. LT-4, no. 10, pp. 1556-1562, Oct. 1986.

8. V. Chan, "Laser for coherent detection systems," in *OSA Annual Meeting, 1988, Technical Digest Series, vol. 11,* (Optical Society of America, Washington, DC, 1988). p. 41, paper MG1

9. R. M. Gagliardi and S. Karp, *Optical Communication,* John Wiley & Sons, New York, 1976.

10. G. S. Mecherle, "Impact of laser diode performance on data rate capability of PPM optical communication," *IEEE Military Communications Conference (MilCom'85)* , Boston, MA, Oct. 20-23, 1985, Conference Record, vol 1, pp. 115-121.

11. J. Katz, "Average power constraints in AsGaAs semiconductor lasers under pulse-position-modulation conditions," *Optics Communications*, vol. 56, no. 5, pp. 330-333, Jan. 1986.

12. A. J. Viterbi, *Principles of Coherent Communication,* McGraw-Hill, New York, 1966, p. 226.

13. S. D. Personick, "Receiver design for digital fiber optic communication systems, II," *The Bell System Technical Journal*, vol. 52, no. 6, pp. 875-887, July-Aug. 1973.

14. R. J. McIntyre, "The distribution of gains in uniformly multiplying avalanche photodiodes: Theory," *IEEE Trans. Electron Devices*, vol. ED-19, no. 6, pp. 703-713, June 1972.

15. J. Conradi, "The distribution of gains in uniformly multiplying avalanche photodiodes: Experimental," *IEEE Trans. Electron Devices*, vol. ED-19, no. 6, pp. 713-718, June 1972.

16. S. D. Personick, P. Balaban, and J. H. Bobsin, "A detailed comparison of four approaches to the calculation of the sensitivity of optical fiber system receivers," *IEEE Trans. Commun.*, vol. COM-25, no. 5, pp. 211-221, May 1977.

17. L. Frecon and E. Sein, "Optical Intersatellite links with semiconductor laser," in *Proc. Int. Astronautical Fed., Int. Astronautical Congr., 35th*, Lausanne, Switzerland, Oct. 1984. paper IAF-84-69

18. C. C. Chen and C. S. Gardner, "Performance of PLL synchronized optical PPM communication systems," *IEEE Trans. Commun.*, vol. COM-34, no. 10, pp. 988-994, Oct. 1986.

19. G. Ling and R. Gagliardi, "Slot synchronization in optical PPM communications," *IEEE Trans. Commun.*, vol. COM-34, no. 12, pp. 1202-1208, Dec. 1986.

20. C. N. Georghiades, "Optimum joint slot and symbol synchronization for optical PPM channel," *IEEE Trans. Commun.*, vol. COM-35, no. 6, pp. 632-636, June 1987.

21. R. Gagliardi, J. Robbins, and H. Taylor, "Acquisition sequences in PPM communication," *IEEE Trans. Infor. Theory*, vol. IT-33, no. 5, pp. 738-744, Sept. 1987.

22. W. K. Marshall, "Word and frame synchronization with verification for PPM optical communications," *proc. IEEE Military Communications Conference (MilCom'86).* Monterey, CA, Oct. 5-9, 1986, vol. 3, pp. 45.3.1-45.3.5.

23. C. N. Georghiades, "On the synchronizability and detectability of random PPM sequences," to appear in *IEEE Trans. Information Theory.*

24. P. P. Webb, R. J. McIntyre, and J. Conradi, "Properities of avalanche photodiodes," *RCA Review*, vol. 35, pp. 234-278, June 1974.

25. T. V. Muoi, "Extremely sensitive direct detection receiver for laser communications," in *Conf. Laser Electro-Optics, (CLEO'87),*, Baltimore, MD, April. 26-May 1, 1987. Digest of Technical Paper, p. 302, paper THS4

26. K. Nosu, "Advanced Coherent Lightwave Technologies," *IEEE Com-*

munication Magazine, vol. 26, no. 2, pp. 15-21, Feb. 1988.

27. D. L. Begley, W. L. Casey, and K. O. Lippold, "Selection of laser diode beam combing techniques for free space communication," in *Optical Technologies for Communication Satellite Applications*, ed. Kul Bhasin, Proc. SPIE 616, pp. 276-280 (1986).

28. G. Stephen Mecherle, "Laser diode combining for free space optical communication," in *Optical Technologies for Communication Satellite Applications*, ed. Kul Bhasin, Proc. SPIE 616, pp. 281-291 (1986).

29. J. M. Senior, in *Optical Fiber Communications, principles and practice*, Prentice-Hall International, Inc., London, 1985.

30. M. C. Teich, K. Matsuo, and B. E. A. Saleh, "Counting distributions and error probabilities for optical receivers incorporating superlattice avalanche photodiodes," *IEEE Trans. Electron Devices*, vol. ED-33, no. 10, pp. 1457-1488, Oct. 1986.

31. M. Schwartz, *Information Transmission, Modulation and Noise*, McGraw-Hill, New York, 1970.

32. R. G. Smith and S. D. Personick, "Receiver design for optical fiber communication systems," in *Semiconductor Devices for Optical Communication*, ed. H. Kressel, Spring-Verlag, New York, 1980. ch. 4.

33. J. B. Abshire, "Performance of OOK and low-order PPM modulations in optical communications when using APD-based receivers," *IEEE Trans. Commun.*, vol. COM-32, no. 10, pp. 1140-1143, Oct. 1984.

34. N. Sorensen and R. Gagliardi, "Performance of optical receivers with avalanche photodetection," *IEEE Trans. Commun.*, vol. COM-27, no. 9, pp. 1315-1321, Sept. 1979.

35. L. L. Jeromin and V. W. S. Chan, "Performance of a coded optical communication system using an APD direct detection receiver," *IEEE International Conference of Communications (ICC'83)*, Boston, MA, June 19-22, 1983, Conference Record, pp 235-244.

36. R. M. Gagliardi and G. Prati, "On Gaussian error probability in optical receivers," *IEEE Trans. Commun.*, vol. COM-28, no. 9, pp. 1742-1747, Sept. 1980.

37. RCA Solid State Detectors, "C30902E, C30902S, C30921E, C30921S silicon avalanche photodiodes," , (data sheet).

38. E. Hecht and A. Zajac, *Optics,* Addison-Wesley, 1974, p. 354.

39. M. C. Hutley, *Diffraction Gratings,* Academic Press, London, 1982.

40. *Optics Guide 4*, Melles Griot Inc. , Irvine, CA, 1988, p. 18-37.

41. W. R. Blood Jr., *MECL System Design Handbook,* Second ed, Motorola Semiconductor Products Inc., 1972.

42. M. I. Skolnik, *Introduction to Radar System,* McGraw-Hill, New York, 1962.

43. T. V. Muoi, "Receiver design for digital optic transmission system using Manchester (biphase) coding," *IEEE Trans. Commun.*, vol. COM-31, no. 5, pp. 608-619, May 1983.

44. F. Andreucci and U. Mengali, "Timing extraction in optical transmissions," *Optical and Quantum Electronics*, vol. 10, pp. 455-458, 1978.

45. R. L. Rosenberg and et al, "Optical fiber repeatered transmission systems utilizing SAW filters," *IEEE Trans. Sonics and Ultrasonics*, vol. 30, no. 3, pp. 119-126, May 1983.

46. U. Mengali and E. Pezzani, "Tracking properties of phase locked loops in optical communication systems," *IEEE Trans. Commun.*, vol. COM-26, no. 12, pp. 1811-1818, Dec. 1978.

47. D. Datta and R. Gangopadhyay, "Simulation studies on nonlinear bit synchronizer in APD-based optical receivers," *IEEE Trans. Commun.*, vol. COM-35, no. 9, pp. 909-917, Sept. 1987.

48. S. D. Personick, "Design of repeaters for fiber systems," in *Fundamentals of Optical Fiber Communications*, ed. M. K. Barnoski, Academic Press, Inc. , New York, 1976. ch. 6

49. S. D. Personick, *Optical Fiber Transmission Systems,* p. 78, Plenum Press, New York, 1981. ch. 3

50. L. E. Franks, "Carrier and bit synchronization in data communication — a tutorial review," *IEEE Trans. Commun.*, vol. COM-28, no. 8, pp. 1107-1121, Aug. 1980.

51. G. Ascheid and H. Meyr, "Maximum likelihood Detection and synchronization by parallel digital signal processing," *proc. IEEE Global Telecommunications Conference, (GlobeCom'84).* Atlanta GA, Nov. 26-29, 1984, pp. 1068-1072

52. F. M. Gardner, *Phaselock Techniques,* John Wiley & sons, New York, 1979.

53. W. R. Bennett, "Statistics of regenerative digital transmission," *Bell System Technical Journal,* vol. 37, pp. 1501-1542, Nov. 1958.

54. F. Davidson and X. Sun, "Gaussian approximation versus nearly exact performance analysis of optical communication systems with PPM signaling and APD receivers," *IEEE Trans. Commun.* , vol. COM-36, no.

11, pp. 1185-1192, Nov. 1988.

55. R. A. Scholtz, "Frame synchronization techniques," *IEEE Trans. Commun.*, vol. COM-28, no. 8, pp. 1204-1213, Aug. 1980.

56. C. N. Georghiades and D. L. Snyder, "Locating data frame in direct detection optical communications," *IEEE Trans. Commun.*, vol. COM-32, no. 2, pp. 118-123, Feb. 1984.

57. C. N. Georghiades, "Joint baud and frame synchronization in optical communications," *IEEE Trans. Commun.*, vol. COM-33, no. 4, pp. 357-360, April 1985.

58. C. N. Georghiades, "On PPM sequences with good autocorrelation properties," to appear in *IEEE Trans. Information Theory.*

59. G. L. Lui and H. H. Tan, "Frame synchronization for direct-detection optical communication systems," *IEEE Trans. Commun.*, vol. COM-34, no. 3, pp. 227-237, Mar. 1986.

60. G. L. Lui and H. H. Tan, "On joint symbol and frame synchronization for direct-detection optical communication systems," *IEEE Trans. Commun.*, vol. COM-35, no. 2, pp. 250-255, Feb. 1987.

VITA

Xiaoli Sun was born in [redacted], on [redacted]. He received the B.S. degree in engineering from Taiyuan Institute of Technology, Taiyuan, China, in January 1982. He began graduate study in electrical engineering at the Tsinghua University, Beijing, China, in February 1982. He entered the Electrical Engineering Department at the The Johns Hopkins University as a graduate student in September 1983 and received the M.S.E. degree in electrical engineering in May 1985. His research areas of interest are optical communication, electronics systems, and statistical theory. He is a student member of IEEE.